UNIVERSITY OF CALIFORNIA, SAN DIEGO

Transverse Wakefield of Waveguide Damped Structures and Beam Dynamics

A dissertation submitted in partial satisfaction of the
requirements for the degree Doctor of Philosophy
in Physics

by

Xintian Lin

Committee in charge:

Professor Norman M. Kroll
Professor Marshall Rosenbluth
Professor Wayne Vernon
Professor Kevin L. Quest
Professor Claudio Pellegrini

1995

The dissertation of Xintian Lin is approved, and it is acceptable in quality and form for publication on microfilm:

_____

_____

_____

_____

_____

Chair

University of California, San Diego

1995

This dissertation is dedicated to my beloved

parents Yang, Xiuqin and Lin, Shengbiao.

TABLE OF CONTENTS

LIST OF FIGURES

LIST OF TABLES

Acknowledgements

Many people have offered me help in my quest in this scientific endeavor. First and foremost, I would like to thank my Ph.D committee members: Drs. Norman M. Kroll, Marshall Rosenbluth, Wayne Vernon, Kevin L. Quest, and Claudio Pellegrini. In particular, I would like to thank my advisor, Dr. Norman M. Kroll, for introducing me to the field of accelerator physics, for providing me with perspective, insight, encouragement, and support, and for giving me the opportunity to continue the research at the Stanford Linear Accelerator Center. I am especially grateful for his patience and understanding. He was always willing to talk when I dropped in to discuss my progress. He spent many weeks carefully reading my dissertation which has been improved a lot based on his invaluable feedback. Virtually all the work reported in this thesis here has benefited from Norman's suggestions, ideas, and criticism. Dr. Marshall Rosenbluth has been of great help by generously providing his keen vision and fruitful discussions. Also thanks to Dr. Wayne Vernon for proofreading the dissertation.

As mentioned above, most of the work in the dissertation was completed at SLAC. I would like to acknowledge Prof. Ron Ruth for hosting me in the Accelerator Theory and Special Project group to whom I am indebted. Thanks to Drs. Bill Hermannsfeldt, Martin Lee, Roger Miller, Tom Knight, and Cho Ng. Special thanks to Dr. Kwok Ko for offering me much invaluable advice and help. I also appreciate the help from the fellow graduate students at SLAC as well as UCSD, specially Dennis D. Palmer, Scott Berg, Zhirong Huang, Drs. Eric Nelson, Chris Nantista, and Yiming Liang.

Substantial credit for my learning accelerator physics is goes to the US Particle Accelerator School for funding all the courses I took at USPAS in six straight years. These courses constitute an indispensable channel of accelerator physics training.

I also appreciate the efforts put in by Dr. T. D. Lee on organizing CUSPEA program through which I enrolled in UCSD.

Since 1984, I have been fortunate to be associated with an outstanding group of classmates from the Special Class for the Gifted Young at the University of Science and Technology of China. They have offered me friendship, fun, inspiration, as well as challenge. Among them, Yanbin Jia deserves special thanks.

Finally, many thanks to Ying for her encouragement and love.

VITA

July 1, 1969	Born, Chengdu, People's Republic of China
1988	B.S., University of Science and Technology of China, Hefei, P.R.China
1988–1989	Teaching Assistant, Department of Physics University of California, San Diego
1989	M.S., University of California, San Diego
1989–1995	Research Assistant, University of California, San Diego
1995	Doctor of Philosophy University of California, San Diego

PUBLICATIONS

"Minimum Wakefield Achievable by Waveguide Damped Cavity", Xintian E. Lin and Norman M. Kroll, *Proc. IEEE Part. Acce. Conf.*, Dallas, Texas, May 1-5 (1995)

"Impedance Spectrum for the PEP-II RF Cavity", Xintian E. Lin, Kwok Ko and C-K Ng, *Proc. IEEE Part. Acce. Conf.*, Dallas, Texas, May 1-5 (1995)

"Design Parameters for the Damped Detuned Accelerating Structure", N. M. Kroll, ... Xintian E. Lin, ... et al, *Proc. IEEE Part. Acce. Conf.*, Dallas, Texas, May 1-5 (1995)

"Impedance Budget of the PEP-II B-factory", S. A. Heifets, ... Xintian E. Lin, ... et al, *Proc. IEEE Part. Acce. Conf.*, Dallas, Texas, May 1-5 (1995)

"Design and Simulation of Accelerating Structures For Future Linear Colliders", K.A. Thompson, ... Xintian E. Lin, ... et al, accepted by *Particle Accelerators*, Nov 1993, (SLAC-PUB-6032)

"Persistent Wakefields Associated with Waveguide Damping of Higher Order Modes", N. Kroll and X. Lin, *Proc. 1993 Particle Accelerator Conf.*, Washington, D.C., May 1993, p.3453 (SLAC-PUB-6144)

"Effectiveness of Higher Order Mode Damping with Waveguide", X. Lin and N. Kroll, presented at *High Power Microwave Handling Workshop*, Lawrence Berkeley Lab., Feb 1993

"Computer Determination of Properties of Waveguide Loaded Cavities", N. Kroll and X. Lin, *Proc. 1990 Linac Conf.*, Albuquerque, NM, June 10-14 (1990), p. 238 (SLAC-PUB-5345)

ABSTRACT OF THE DISSERTATION

Transverse Wakefield of Waveguide Damped Structures and Beam Dynamics

by

Xintian Lin
Doctor of Philosophy in Physics
University of California, San Diego, 1995
Professor Norman M. Kroll, Chair

In the design of new high energy particle colliders with higher luminosity one is naturally led to consider multi-bunch operation. However, the passage of a leading bunch through an accelerator cavity generates a wakefield that may have a deleterious effect on the motion of the subsequent bunches. Therefore, the suppression of the wakefield is an essential requirement for beam stability. One solution to this problem, which has been studied extensively, is to drain the wakefield energy out of the cavity by means of waveguides coupled with the cavity and fed into matched terminations [2]. Waveguide dimensions are chosen to yield a cutoff frequency well above the frequency of the accelerating mode so that the latter is undamped. This paper presents a thorough investigation of the wakefield for this configuration.

The effectiveness of waveguide damping has typically been assessed by evaluating the resultant Q_{ext} of higher order cavity modes to determine their exponential damping rate. We have developed an efficient method to calculate Q_{ext} of the damped modes from popular computer simulation codes such as MAFIA. This method has been successively applied to the B-factory RF cavity.

We have also found another type of wakefield, associated with waveguide cutoff, which decays as $t^{-\frac{3}{2}}$ rather than in the well-known exponentially damped manner.

Accordingly, we called it the *persistent wakefield*. A similar phenomenon with essentially the same physical origin but occurring in the decay of unstable quantum states, has received extensive study [3].

Then we have developed various methods of calculating this persistent wakefield, including mode matching and computer simulation. Based on a circuit model we estimate the limit that waveguide damping can reach to reduce the wakefield.

Finally, based on an analytic treatment of the Beam Break-Up(BBU) instability, we show that bunch to bunch accumulation effects are limited for any wakefield that falls off at least as fast as t^{-1}. As a consequence, there is no significant qualitative difference in the effect on BBU of a $t^{-\frac{3}{2}}$ decaying wakefield and an exponentially damped one, and even the quantitative difference is small when the characteristic decay lengths are the same. The persistent wakefield, in particular, turns out to have a small effect based on the current Next Linear Collider parameters.

Chapter 1

Introduction

1.1 Wakefield

Colliders, the colliding beam devices, are first introduced by D. Kerst [1] in 1956 to achieve the highest center of mass energy as compared to the fixed target experiments. Their main parameters are energy and luminosity. As the name suggests, energy is the energy carried by each charged particle. The higher the energy, the deeper the fundamental structure it reveals. The proposed Next Linear Collider (NLC) has a 0.5 TeV center of mass energy, upgradable to 1 TeV. While colliders for high energy particle physics research typically aim for the highest achievable energy, some machines are designed at specific energy to explore the physics there or to produce a large amount of certain particles at resonance. For example, the ongoing B-factory project at Stanford Linear Accelerator Center, targeted at 10.58 GeV center of mass energy [8], produces hundreds of millions of B mesons on the $\Upsilon(4S)$ resonance. Luminosity, on the other hand, is a measure of the number of particle collisions per unit time. It is always favorable to have a machine with higher luminosity so that small cross section events can be studied in a reasonable amount of experiment time. Besides, due to the kinematics of high energy collision, cross section scales with energy as $\frac{1}{E^2}$; so the future TeV colliders necessarily require a very high luminosity. The proposed NLC is aiming for a luminosity of $10^{33} - 10^{34} cm^{-2} sec^{-1}$.

Luminosity can be increased by accelerating more particles per bunch, by increasing collision frequency, and by reducing the beam area[1]. Since a charged bunch interacts electromagnetically with the surroundings, usually a metallic vacuum chamber, it generates an electromagnetic field, called *the wakefield*. The wakefield acts back on the motion of the bunches, including the source bunch and the trailing bunches. It causes instability and subsequent beam loss. The number of particles per bunch is limited by single bunch instabilities. For example, the space charge effect will limit the bunch charge at the gun and the low energy transport line; energy spread and single bunch beam break up [4] from the short range wakefield also limit the charge of a single bunch. The long range wakefield, on the other hand, restricts the bunch collision frequency. The second bunch cannot be injected until the wakefield generated by the first one dies out, or becomes negligible, unless other measures are taken[2].

1.2 Wakefield Suppression

The wakefield can be reduced by coupling out of the cavity with waveguides and feeding into matched loads [2]. The cutoff frequency of the waveguide is chosen such that all but the accelerating mode are damped. The rate of the energy propagating out of the cavity is proportional to the field square at the port, that is

$$\frac{dE}{dt} = -\alpha F^2 = -\alpha' E, \tag{1.1}$$

where E is the total energy in the cavity, F is the field (either electric or magnetic field) at the port, and α and α' are two constants. From the above differential equation, we get an exponential decay law,

$$\left.\begin{aligned} E(t) &= E(0)e^{-\alpha' t} = E(0)e^{-\frac{\omega t}{Q_{ext}}} \\ F(t) &= F(0)e^{-\frac{\alpha'}{2}t} = F(0)e^{-\frac{\omega t}{2Q_{ext}}} \end{aligned}\right\}, \tag{1.2}$$

[1] NLC is designed to focus the beam to a tiny spot 60 nanometers high and 1 micron wide at the collision region.

[2] Such as feed back.

where Q_{ext} is the external Q of the damped mode.

The natural ohmic loss on the wall, for the same reason, also gives rise to exponentially decaying fields. It typically yields a much higher Q value. A rough estimate of Q for a cavity mode can be obtained [7] by

$$Q \approx \frac{V}{S\delta_{skin}} = \frac{V}{S}\sqrt{\frac{\mu\sigma\omega}{2}}, \tag{1.3}$$

where V and S are the volume and the total surface area of the cavity, respectively, δ_{skin} is the skin depth evaluated at the mode frequency, and σ is the metal conductivity. For example, B-factory cavity modes have a natural Q of 40000 (principle mode, 476 MHz). The Q of the Higher Order Mode (HOM) is about the same. On the other hand, with the help of waveguide damping, the HOM Q_{ext} of the B-factory RF cavity is reduced to around 20[3], making it possible to achieve a bunch separation of 1.26 meter, a total of 1658 bunches[4] in the ring [8]. See Fig. 1.1. It is designed to achieve a luminosity of $3 \times 10^{33} cm^{-2} sec^{-1}$.

The effectiveness of waveguide damping has typically been assessed by evaluating the resultant Q_{ext}. It will be the most reliable and straightforward to calculate the resonant frequency of the cavity subject to *outgoing wave boundary condition* at the waveguide port. The resonant frequency is typically complex, the real part is the oscillating frequency, while the imaginary part is the amplitude decay rate. A real resonant frequency means that the mode is trapped, it does not decay at all.

Except for some simple geometries, analytical solutions of this sort are hard to find. A number of powerful computer programs have been developed to compute the resonant frequencies of *closed* cavities. These programs apply finite difference or finite element methods to a lattice representation of the cavity (We refer to them as Lattice Based Closed Cavity, LBCC, programs.). In addition, the field distributions, Q due to the metal wall losses, dielectric losses and time domain evolution are

[3] Even lower Q can be achieved, but one has to weight the loss of the fundamental mode shunt impedance.

[4] Compare with just 1 or a few in first generation colliding rings. The B-factory uses feed back to control transverse instabilities too. In fact, the Q value is not low enough to completely damp the wakefield, but enough so that a small amount of feed back power can handle the instability.

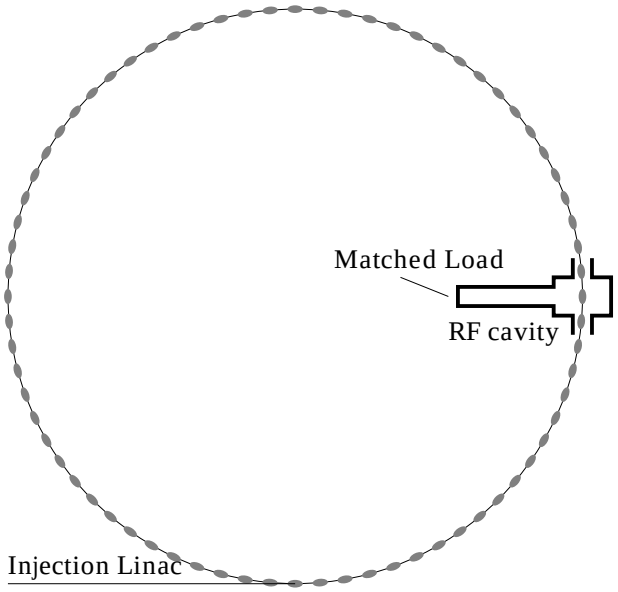

Figure 1.1: Schematic layout of a storage ring. Only one waveguide and one RF cavity are shown. Typically, there are 3 or more waveguides attached to each RF cavity to damp dipole modes of all polarizations and minimizing distortion of the field of the accelerating mode.

readily available. Examples are MAFIA [9], SUPERFISH [10]. These programs have proven to be valuable tools for accelerator cavity design. However, they do not include procedures for external Q calculation on coupling a waveguide with a matched load configuration. Currently, there is a strong interest in cavities which are heavily damped by external coupling to facilitate multi-bunch operation. Examples are SRS cavity [11] at Daresbury and ALS cavity [12] at LBL.

It is clear from the work of Slater [13] that the desired information can be obtained by inserting a terminating short at the end of the waveguide and studying the behavior of the combined cavity, shorted waveguide system. Gluckstern and Li [14] have described a computer implementation of applying the Slater method. Kroll and Yu [16] have developed a related but distinct method, which we have modified to reduce the number of computer runs needed and to extend the domain of applicability. It will be covered in chapter 2. Arcioni and Conciauro [19] have also developed a program to calculate the whole excitation spectrum, in which Q_{ext} follows from the width of each peak. Their method combines information obtained from

LBCC programs with a mode matching approach applied to the damped waveguides.

While the waveguide damping research reported here has been in progress, other methods, including cavity detuning, damped detuning, and patching lossy material on the cavity wall, have been suggested and are being actively pursued. These alternatives will not be discussed here; interested readers are referred to [20], [21], [22], [6] and [5].

1.3 Beam Break-Up Instability

In the linac of the proposed SLAC NLC design, 90 one nanocoulomb bunches are accelerated in a train. In fact, it is the de facto approach of most NLC designs to increase luminosity. In this multi-bunch design, one important issue that needs to be coped with is the transverse Beam Break-Up (BBU) instability [23]. There is single bunch BBU and a multi-bunch version of it. Their underlying physics is the same, but different aspects of the wakefield are involved. Single bunch BBU is dependent upon the very short range wakefield, while multi-bunch BBU is affected by the long range wakefield. Here when referring to BBU, we always mean multi-bunch BBU.

When an intense beam passes through an accelerating cavity slightly off axis, it will generate a strong wakefield that kicks the trailing beam off axis. A simple calculation points to linear growth of the second bunch, quadratic growth of the third bunch, ..., t^{n-1} growth for the nth bunch. This more and more rapid growth for the later bunches poses a serious danger to emittance control. We will address the problem of what type of wakefield leads to a stable bunch train for a given linac length in Chapter 7.

We begin by examining two bunches in a train, it is straightforward to generalize to n bunches. Assume no acceleration and smooth focusing for the sake of simplicity. The equations of motion are

$$\left.\begin{aligned} x_1'' + k^2 x_1 &= 0; \\ x_2'' + k^2 x_2 &= \frac{Ne^2 W_\perp(l)}{E} x_1 \end{aligned}\right\}. \tag{1.4}$$

Here x_1, x_2 are the transverse displacement of the first and second bunch, respectively, k is the betatron wave number, l is the distance between bunches. Also E denotes the energy of the electrons in the beam, $W_\perp(l)$ is the transverse wake function at the location of the second bunch due to the first, and N is the number of electrons per bunch. The prime stands for derivative with respect to longitudinal distance s.

Taking the solution of the first equation in the form $x_1(s) \propto e^{iks}$, we obtain

$$\left.\begin{array}{rcl} x_1(s) & = & a e^{iks} \\ x_2(s) & = & a(1 + \frac{Ne^2 W_\perp(l)}{2ikE} s) e^{iks} \end{array}\right\}. \tag{1.5}$$

Note that while the oscillation amplitude of x_1 is constant, that of x_2 grows linearly with s. The secular growth is the direct consequence of the fact that the two bunches oscillate in resonance.

There are many situations in which the wakefield is strongly damped so that a bunch will only feel the wakefield generated by the immediately preceding bunch. In this case, we can use a simple "daisy chain" model to estimate the transverse blowup of each bunch. The equations of motion become

$$\begin{array}{rcl} x_1'' + k^2 x_1 & = & 0 \quad ; \\ x_n'' + k^2 x_n & = & \frac{Ne^2 W_\perp(l)}{E} x_{n-1} (n > 1). \end{array} \tag{1.6}$$

We assume the solutions are of the form $x_n(s) = a_n(s) e^{iks}$, which yields

$$a_n'' + 2ika_n' = \frac{Ne^2 W_\perp(l)}{E} a_{n-1}, \tag{1.7}$$

and since $a_n(s)$ is a slow varying function, we neglect the a_n'' term. Thus we have

$$a_n' = -i\sigma a_{n-1}, \tag{1.8}$$

where $\sigma = \frac{Ne^2 W_\perp(l)}{2kE}$. It is straightforward to show that the solution is (with initial condition $a_n(0) = 1$ for all n)

$$a_n(s) = \sum_{j=0}^{n-1} \frac{(-i\sigma s)^j}{j!}. \tag{1.9}$$

We see that a_3 grows quadratically with sufficient large σs, a_4 grows with third power, and so on. Also note, $\lim_{n\to\infty} a_n(s) = e^{-i\sigma s}$. In fact, so long as $n \gg \sigma s$, the

asymptotic expression is valid. The apparent stability for later bunches is the result of the fact that the wakefield is short-ranged, and also due to the fact that the resonant response of a bunch to the transverse displacement of the preceding bunch is 90^o out of phase with it. Thus there is no long term accumulation of bunch displacement with the bunch number. We shall address this issue again in Chapter 7.

Chapter 2

Wakefield Damping

Strong wakefield damping can be achieved by a waveguide feeding to a matched load. A considerable effort has been spent on how to characterize the cavity-waveguide system.

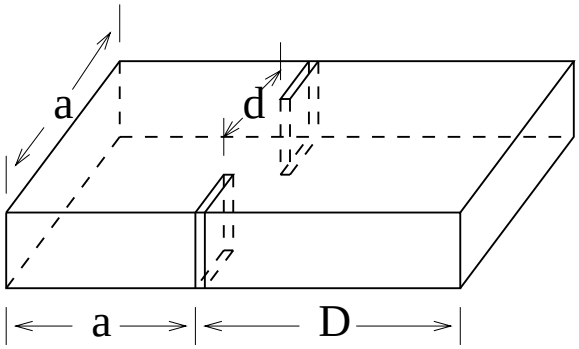

Figure 2.1: Shorted waveguide-cavity system. The cavity is an $a \times a$ square. It is coupled to a waveguide of the same width through an iris of size d. A shorted plane is placed at distance D away from the iris.

Consider a cavity attached to a single waveguide through a small iris. The smallness of the iris is not required, but many properties of this system can be easily quantified with small coupling. Following Slater [13], we place a short at a distance D away from the waveguide-cavity junction. See Fig. 2.1. The shorted waveguide can be viewed as a cavity with a certain resonant frequency depending on the length D. Let us denote by ω_1 the resonant frequency of the cavity without iris opening,

and by ω_2 that of the shorted waveguide. In the presence of a small iris, the two modes are coupled with each other, with eigenfrequencies ω_+, and ω_-. Without loss of generality, we assume $\omega_1 > \omega_2$. When the fractional frequency difference of ω_1 and ω_2 is much greater than the coupling constant η[1], each eigenmode looks like either that of ω_1 or ω_2, i.e. the coupling between the modes is small. Field patterns and frequencies are similar to the uncoupled case, i.e. $\omega_+ - \omega_- \approx \omega_1 - \omega_2$. By sliding the waveguide shorting plane inward, we could increase ω_2. When ω_2 is very close to ω_1, where the closeness is measured by the coupling constant, both cavity and waveguide are excited at each eigenmode. If $\omega_1 = \omega_2$, cavity and waveguide store equal amount of energy at each eigenmode , and $\omega_+ - \omega_-$ is minimized. For small couplings, the minimum separation is related to coupling constant:

$$\eta = 2\left(\frac{\omega_+ - \omega_-}{\omega_+ + \omega_-}\right)_{minimum} \tag{2.1}$$

When we further increase ω_2, the difference of the eigenmode frequencies increases. This phenomena is called *avoided crossing* (AC). Numerical simulations using MAFIA on the geometry shown in Fig. 2.1 are performed to illustrate this behavior. (See Fig. 2.2.)

The same structure with zero iris thickness can be solved analytically based on an equivalent circuit model [16]. Typical examples are illustrated in Fig. 2.3. Fig. 2.3a exhibits the behavior when the external coupling is quite small. The dashed lines correspond to the waveguide modes present with no coupling between waveguide and cavity. The solid lines, which represents the frequency of the coupled system when a small iris is opened between the cavity and the waveguide, exhibit AC behavior near each point where the uncoupled waveguide and cavity mode curve would cross. They exchange mode characteristics after crossing. Fig. 2.3b shows the evolution of this behavior when coupling increases. An inspection of Fig. 2.3 convinces one that no matter what waveguide shorting length is chosen, there is at least one cavity-waveguide eigenfrequency that is close to resonance.

[1] η is defined in the circuit model as $\eta = \frac{M_{12}}{\sqrt{L_1 L_2}}$, where M_{12} is the mutual inductance which couples the LC resonant circuits, and L_1 and L_2 are the inductances of each circuit.

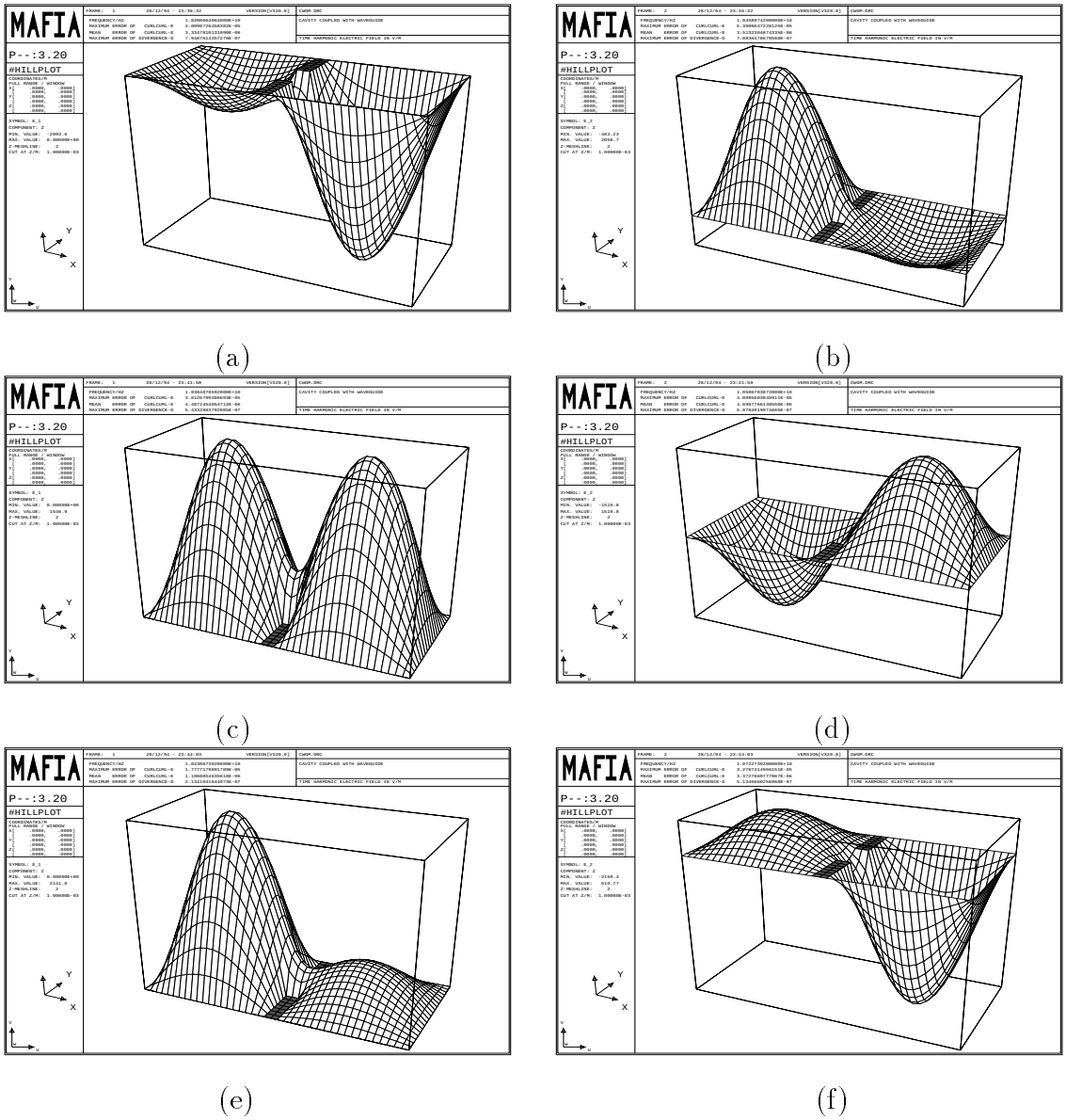

Figure 2.2: Electric field plots from the MAFIA simulations of the cavity-waveguide system shown in Fig. 2.1, with $a = 2cm$, $d = 0.6cm$, and iris thickness $0.2cm$. The shorting distance D is chosen to be 2.1cm in plot (a) and (b), 2.0cm in plot (c) and (d) and 1.9cm in plot (e) and (f) respectively. We have $\omega_a = 10201MHz$ (primarily the waveguide mode) and $\omega_b = 10459MHz$ (primarily the cavity mode) with $\Delta\omega_{ab} = 258MHz$, $\omega_c = 10385MHz$ and $\omega_d = 10507MHz$ with $\Delta\omega_{cd} = 122MHz$, and $\omega_e = 10431MHz$ (primarily the cavity mode) and $\omega_f = 10723MHz$ (primarily the waveguide excitation) with $\Delta\omega_{ef} = 292MHz$.

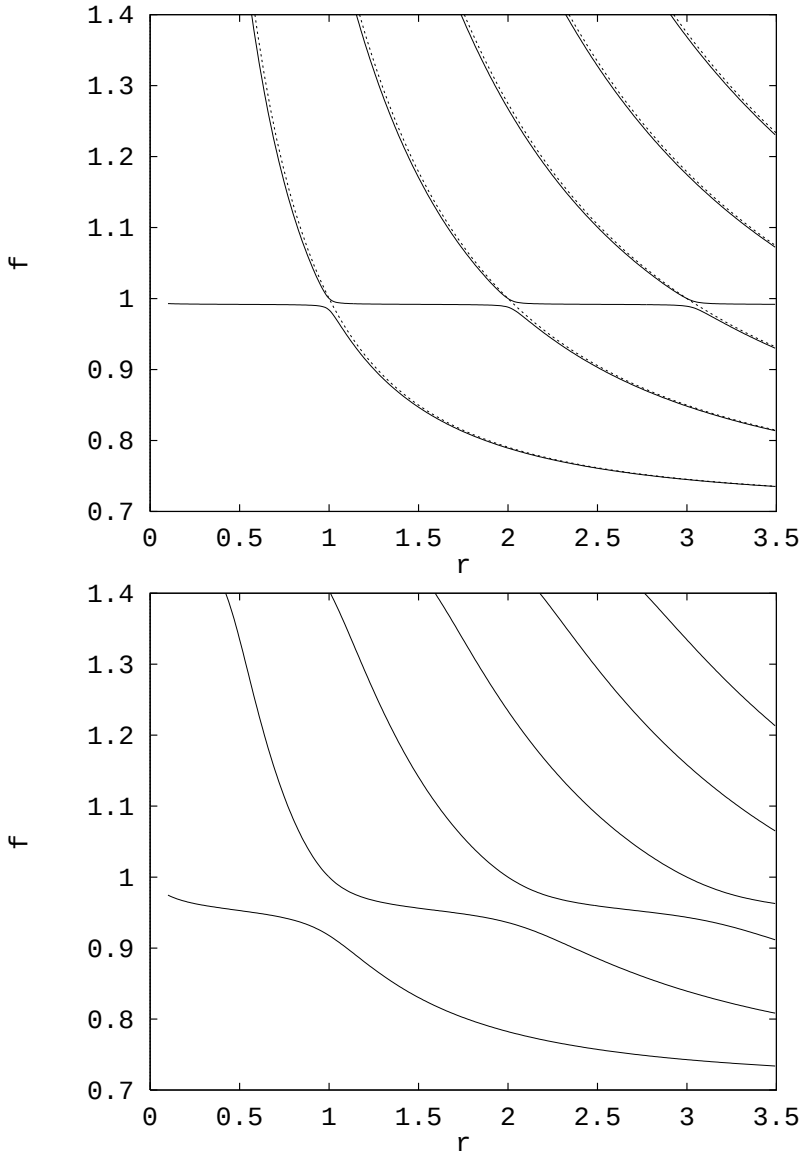

Figure 2.3: Typical examples of relative frequency f plotted as a function of relative length r of the waveguide. The frequency f is normalized to the frequency of the uncoupled cavity mode, and the waveguide length r is normalized to one half the cutoff wavelength. The cavity mode is sufficiently isolated, so that other cavity modes do not have a significant effect over the frequency range shown. The top figure represents a weakly coupled case, where the dashed lines are the uncoupled waveguide resonance. The bottom one shows a case of moderate coupling.

Qualitatively speaking, at the AC, the mean frequency of the two eigenmodes gives the resonance frequency of the cavity, and the minimum separation yields the coupling constant. However, relating η to the Q_{ext} requires a theory and an equivalent circuit, and the relation is different for each AC.

The Kroll-Yu (KY) method (See Appendix B) and the method discussed below are, on the other hand, based upon study of the frequency dependence of the reflection coefficient $R(\omega)$ near the cavity resonance frequency.

2.1 Kroll-Lin (KL) Method

The KY method, in writing the reflection coefficient near the resonance as (see Eqs. B.1, B.2, and B.4)

$$-e^{2jkD} \equiv R(\omega) = -\frac{\omega - u + jv}{\omega - u - jv} e^{-2j(\chi(u)+\chi'(u)(\omega-u))}, \tag{2.2}$$

provides a four-parameter representation of the reflection coefficient. Four MAFIA runs at four different waveguide shorting distance D provide enough information to find the parameters u, v, $\chi(u)$, and $\chi'(u)$.

A highly accurate MAFIA calculation usually consumes a large amount of computer time[2]. Therefore the reduction of the number of MAFIA runs is quite desirable. Our extension on top of the KY method reduces MAFIA runs by a factor of two and make it possible to obtain Q_{ext} from a single MAFIA run. It essentially utilizes the extra information provided by numerical code on such quantities as field strength, energy, etc. [18]

Taking tangent of Eq. B.3 and using the approximation in Eq. B.4, we obtain

$$\tan(k(\omega)D + \chi(u) + \chi'(u)(\omega - u)) = \frac{u}{2Q(\omega - u)}. \tag{2.3}$$

Differentiating Eq. 2.3 with respect to ω, we find

$$\frac{d\omega}{dD} = -k(\omega)\left(\frac{\omega D}{k(\omega)c^2} + \chi'(u) + \frac{2Qu}{4Q^2(\omega - u)^2 + u^2}\right)^{-1} \tag{2.4}$$

[2]Because MAFIA 3.20 is a finite difference program, in order to model the curved boundary, it has to have a very small mesh size. And the time needed in a sparse matrix eigenmode calculation is proportional to the number of mesh points, i.e. mesh size to the - 3rd power in 3D.

where c is the speed of light. Eq. 2.4 is a new condition that u, v, $\chi'(u)$ have to satisfy. It is useful only if we can calculate $\frac{d\omega}{dD}$ independently. This can be done via the formula

$$\frac{d\omega}{dD} = -\frac{\omega \int (\mu_0 H^2 - \epsilon_0 E^2) dS}{2 \int \mu_0 H^2 dV}, \tag{2.5}$$

which is a result of the cavity perturbation theory [13]. The denominator on the right side of the above equation is the stored energy of the whole cavity system, which is a standard output of MAFIA. The numerator includes the surface integral at the shorting plane. Since MAFIA also provides the field strength at any locations, the surface integral can also be evaluated.

Now we are able to calculate u, v, $\chi(u)$, and $\chi'(u)$ with two frequency-length pairs plus two derivatives. With the inspection of the field plot, if one branch is recognized near the resonance, another run at a different length is needed to provide a second point; if two branches near the cavity resonance can be identified, which is usually the case, one MAFIA run suffices.

2.1.1 Implementation Formula

The parameter determination procedure described in Sec. B.1 is readily adapted to our new method by taking limits as the frequencies approach one another in pairs. We need to use $\frac{d\phi}{d\omega}$ instead of $\frac{d\omega}{dD}$. They are related by

$$\frac{d\phi}{d\omega} = \frac{k(\omega)}{\frac{d\omega}{dD}(\omega)} + \frac{\omega D}{k(\omega) c^2}. \tag{2.6}$$

From the input data points and an assumed value of $\chi'(u)$, we define

$$B_1 \equiv (\tfrac{d\phi}{d\omega}(\omega_1) + \chi'(u))^{-1}, \tag{2.7}$$

$$B_{12} \equiv (\omega_1 - \omega_2) \cot(\phi_1 - \phi_2 + \chi'(u)(\omega_1 - \omega_2)), \tag{2.8}$$

and

$$A \equiv \tfrac{B_1 - B_{12}}{\omega_1 - \omega_2}. \tag{2.9}$$

From these, we obtain

$$v = \tfrac{-B_1}{1 + A^2}, \tag{2.10}$$

and

$$u = \omega_1 - Av. \tag{2.11}$$

We then determine $\chi'(u)$ numerically as the root of

$$\frac{d\phi}{d\omega}(\omega_2) + \chi'(u) + \frac{v}{(\omega_2 - u)^2 + v^2} = 0. \tag{2.12}$$

We have implemented a FORTRAN program to search the root automatically. In this method, $\chi(u)$ is not involved in determining the other parameters. It may be determined upon substituting u, v and $\chi'(u)$ in Eq. B.9.

2.2 Numerical Investigations of the Sensitivity of the KL Method on the Choice of the Waveguide Length

In order to test the validity and sensitivity of the KL method, we have tested several simple configurations, one with known analytical result, and the other with input from a computational simulation code. The test results are compared to themselves to show the self consistency. Both have shown excellent agreement.

2.2.1 Analytic Waveguide Model

We first tested the KL method on the analytic waveguide model introduced in Sec. 3 of Kroll and Yu's paper [16]. (See Fig. 2.1 also.) This is a standard TE^{10} waveguide. With an adjustable symmetric iris parallel to the electric field, it forms a waveguide loaded resonator. When taking a zero thickness iris, this configuration can be modeled accurately by the equivalent circuit shown in Fig. 2.4, provided the frequency of concern is lower than the cutoff of the higher waveguide mode. The open waveguide is represented by the equivalent circuit shown in Fig. 2.4(a), and the waveguide with variable short is shown in Fig. 2.4(b). The parallel lines represent transmission lines with propagation constant k satisfying

$$k^2 = (\frac{\omega}{c})^2 - (\frac{\pi}{a})^2$$

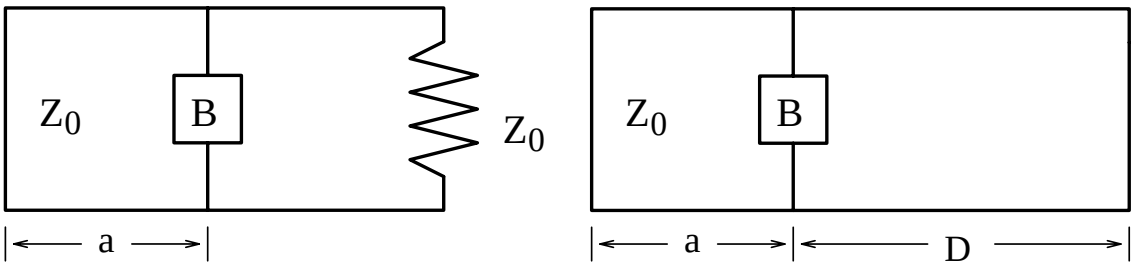

(a) (b)

Figure 2.4: (a) Equivalent circuit for the waveguide model with outgoing wave boundary condition. (b) Equivalent circuit for the waveguide model with terminating short at distance D from the output window

Even though the exact formula of shunt susceptance B is not known, highly accurate expression may be found in the *Waveguide handbook* by Marcuvitz. Since we are interested in testing the KL method, only a reasonably accurate expression for B is needed. We used

$$B = -(\frac{2\pi}{ka})\cot^2(\frac{\pi d}{2a}) \tag{2.13}$$

where B has been normalized to the characteristic admittance of the waveguide TE^{10} mode.

The resonant condition of the circuits in Fig. 2.4 requires that the sum of all admittance of the elements vanishes. We choose the reference point at the window, where the short at the left side transformed into $-j\cot(ka)$. Because it is a matched line on the right hand (see Fig. 2.4(a)), the admittance is 1. Thus the resonance condition of the open waveguide is

$$-j\cot(ka) + jB + 1 = 0. \tag{2.14}$$

It becomes

$$\cot(\pi x) + \frac{2}{x}\cot^2(\frac{\pi d}{2a}) + j = 0 \tag{2.15}$$

where $x = \frac{ka}{\pi} = \sqrt{2(\frac{\omega}{u_0})^2 - 1}$. Similarly the circuit equation of the shorted waveguide is

$$\cot(\pi x) + \frac{2}{x}\cot^2(\frac{\pi d}{2a}) + \cot(\pi x\frac{D}{a}) = 0. \tag{2.16}$$

Our object here is to solve the circuit model Eq. 2.15 to find the complex resonant frequency ω, i.e. the u and v (as the real and imaginary part of ω, respectively.) in the KL method. And the circuit equation 2.16 simulates what simulation codes will give you with a shorting distance D, i.e. length, frequency pairs. Since Eq. 2.16 is an analytic expression, it also yields $\frac{d\omega}{dD}$[3]. All these information is then fed into the KL implementation to solve for u and v. By a comparison of the values of u and v with the known result, the accuracy of the KL method can be tested. Our exercise also shows the sensitivity of the KL method to the shorting distance chosen.

The results obtained for a set of seven iris openings are shown in Fig. 2.5 and 2.6 for Q and u, respectively. Calculations were performed at a large number of lengths between $R = 0.8$ to 3, so that the dependence of the computed Q and frequency U on the length could be displayed as continuous curves. In carrying out the procedure, it is also necessary to choose the right pair of branches. See Fig. 2.3, at $r \sim 1$, branches 1 and 2 are near the avoided crossing, when r is increased. branch 1 moves downward quickly, so does branch 3. So around $r \sim 2$, branches 2 and 3 are near the avoid crossing, clearly the better choice than branch 1 and 2. We use a simple criteria to determine the switch: Use the pair with the smallest frequency difference, provided they are significantly below the frequency of the next higher cavity resonance. The discontinuity of the curves in Fig. 2.5 and 2.6 reflects the successive jumps to the higher branches.

Ideally, we would hope that the solid curves coincide with the dashed lines, which are the exact value from the circuit models. The discrepancy is then a measure of how reliable the KL method is. We have the following observations:

- The relative accuracy increases with higher Q
- The agreement and consistency arising from the combination of branches 1 and 2 is noticeably poorer than that from the higher branch combinations. This is explained by noting that the frequencies involved in the lower branch combinations are further from the complex pole. Thus the linear approximation

[3] while simulation obtains the same quantity through Eq. 2.5

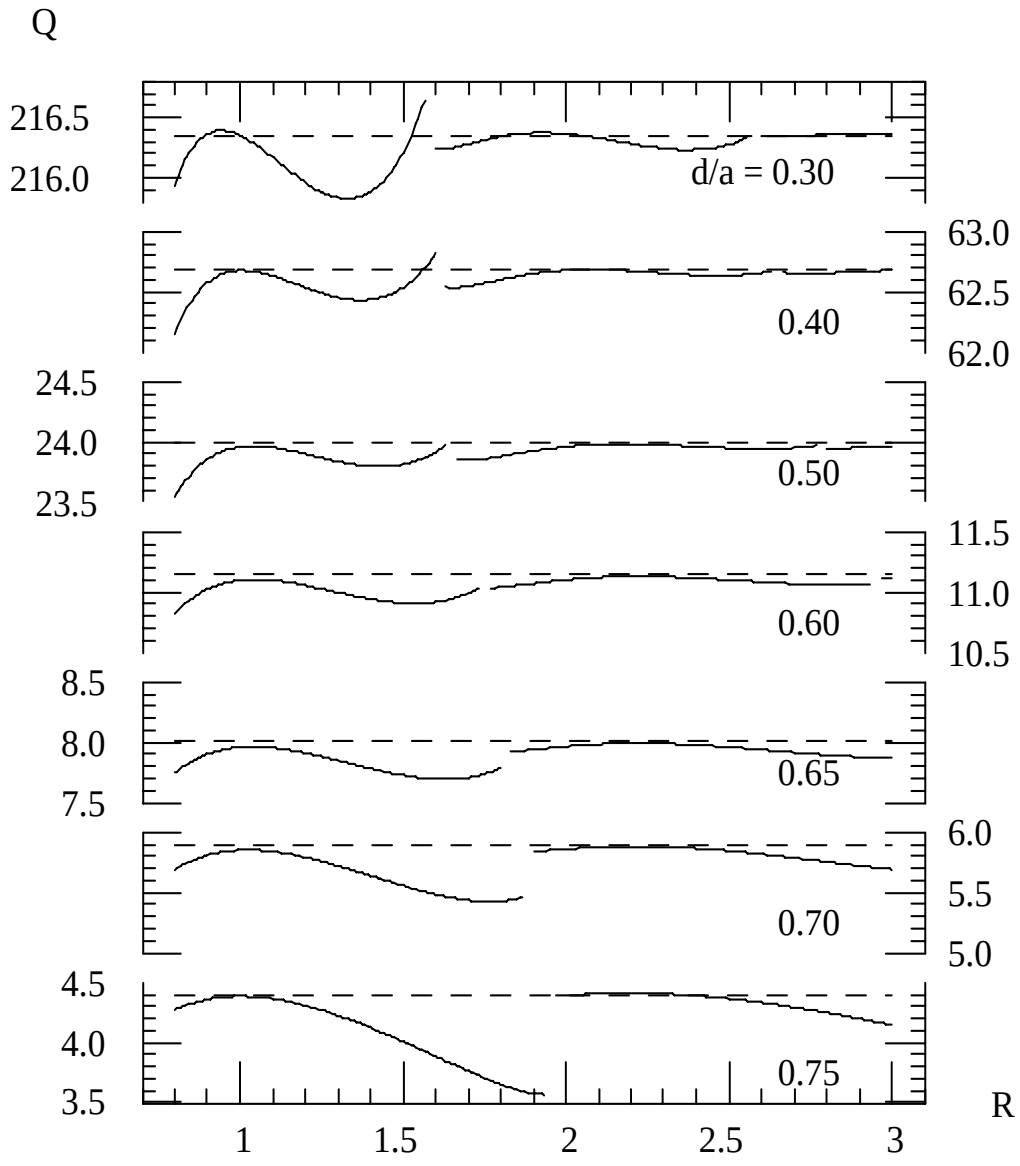

Figure 2.5: The Q_{ext} of the waveguide model. The R is the ratio of D and a. The symbol d is the iris opening, and the dashed line represents the exact solution from Eq. 2.15.

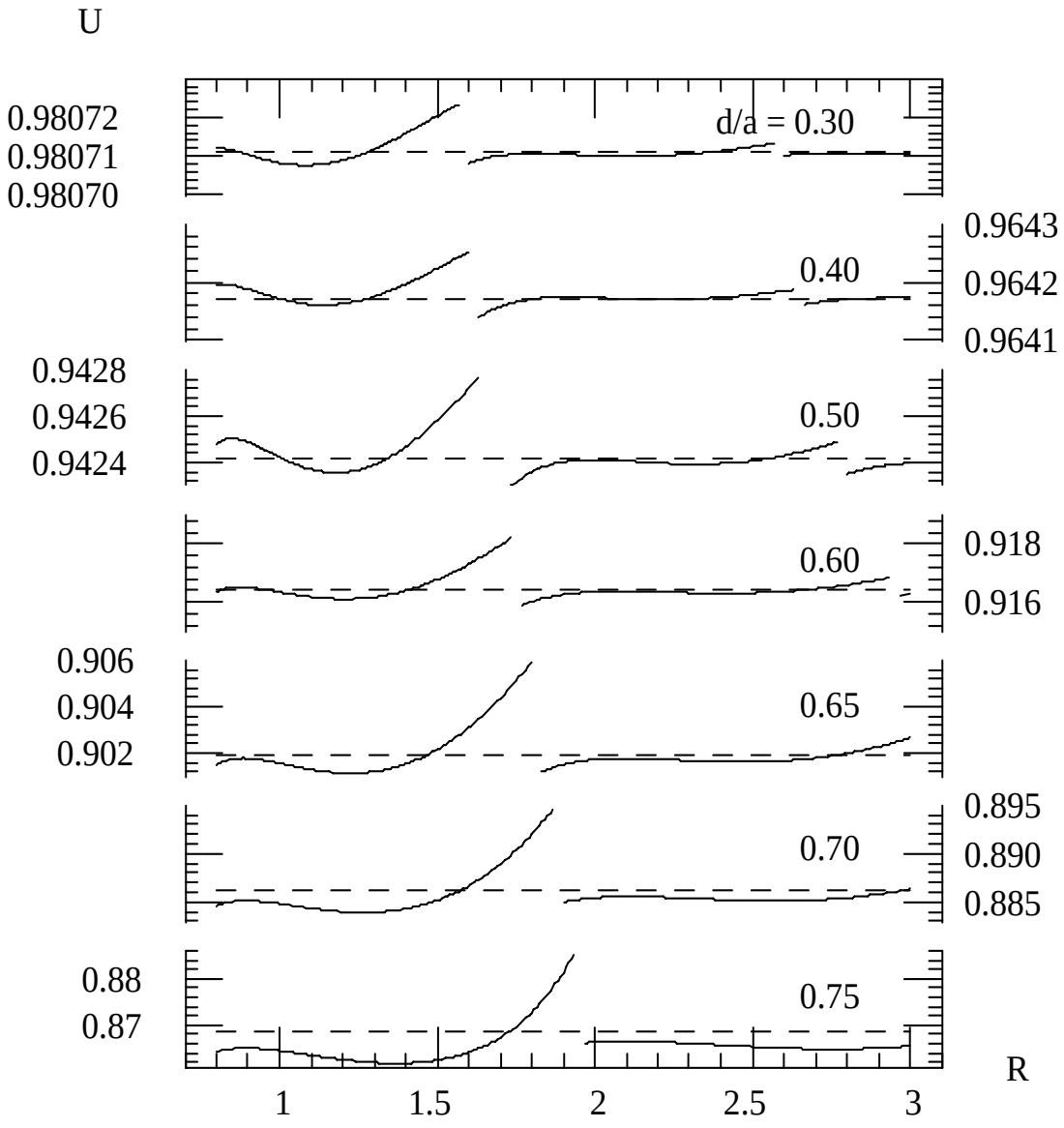

Figure 2.6: The resonant frequencies of the waveguide model. The R is the ratio of D and a. The symbol d is the iris opening and the dashed line represents the exact solution from Eq. 2.15.

in Eq. B.3 is less accurate, resulting in a poorer result. Since one usually has a rough idea of where the resonant frequency is, the lower branch combination can be avoided by choosing a longer waveguide length.

- Agreement is the best at the avoided crossing region. Because, near the avoided crossing, the frequency difference is the smallest. It is our view, that the agreement is good enough for most practical purpose at any waveguide length.

2.2.2 Computer Simulations

The real application of the KL method is in the computational context. As a test to the method, we chose the geometry illustrated in Fig. 2.1, with $a = 0.9$ inch, iris thickness $\frac{1}{32}$ inch, and iris opening $\frac{d}{a}$ left for variation. The cavity mode of interest is similar to the TM^{110} mode in a 0.9 inch by 0.9 inch box, independent of height. This mode has an electric field perpendicular to the top and bottom plane. This is essentially a 2 dimensional problem, MAFIA 3D code is used because of its many advantages. The height-dependent modes are avoided by choosing a very small height (0.01 inch) to push them far above the spectrum of interest.

We begin the analysis of the computer output by examining the field plot of the cavity-waveguide system. In Fig. 2.7, we plot the field of the lowest four modes in the case of $\frac{d}{a} = 0.5$ inch, $D = 2$ inch. Because the configuration has a mid plane reflection symmetry, only one half of the cavity-waveguide system need be considered. Since the lowest cavity modes is symmetric, we apply a symmetric boundary condition at the mid plane (instead of an antisymmetric boundary condition). The field pattern clearly indicates that mode 3 is the closest to the cavity resonance: The field pattern in the cavity is close to that of TM^{11}, plus the fact that most of the energy is inside the cavity. Modes 2 and 4 are on the lower and the higher branches, respectively. Because the frequency difference between modes 2 and 3 (533 MHz) is smaller than that between modes 3 and 4 (1710 MHz). We choose modes 2 and 3 for application of the KL method, the result is $Q = 34.542$ and resonant frequency = 8769.07 MHz.

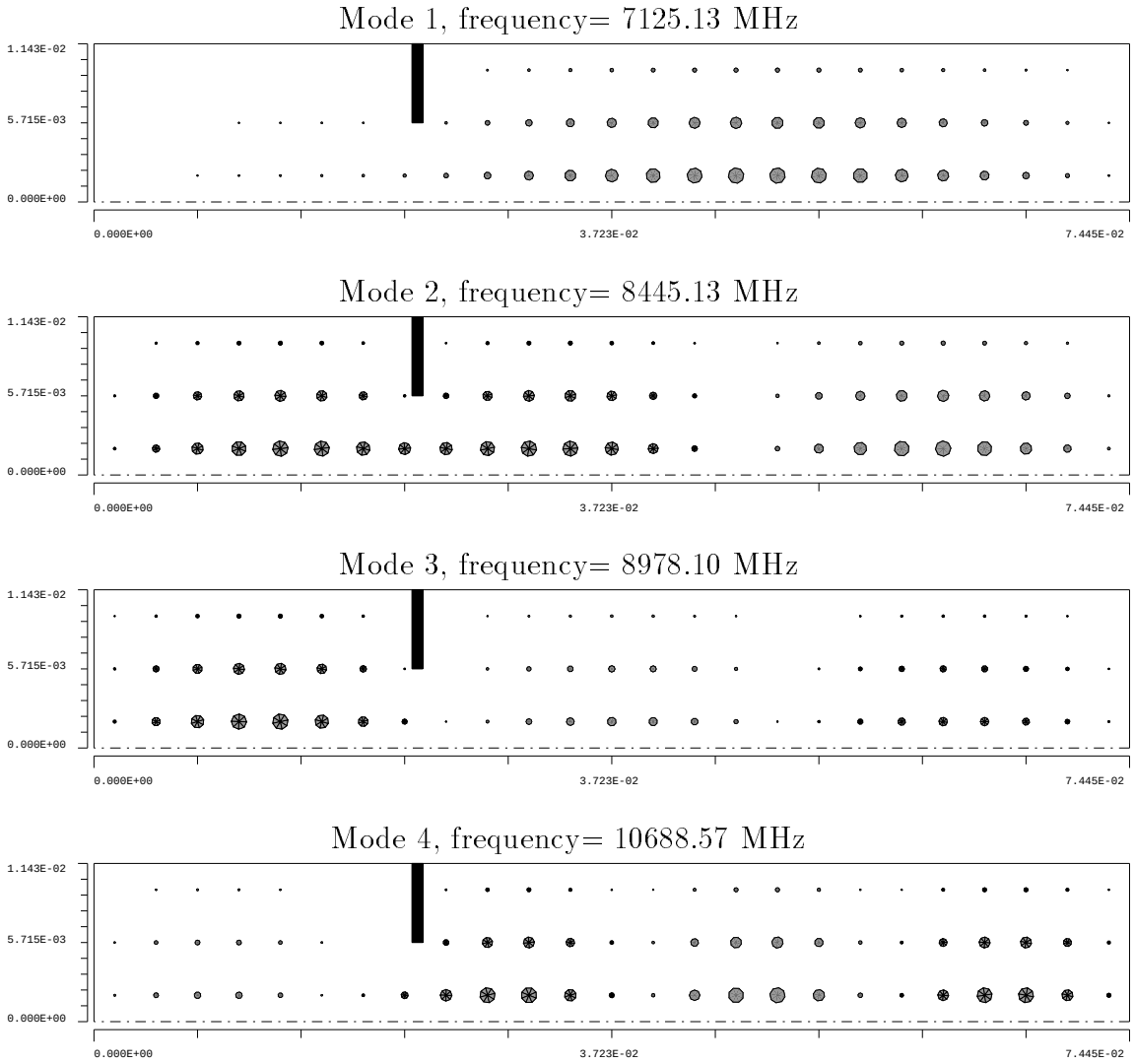

Figure 2.7: Field plots of a cavity-waveguide system. The E_z field (z is coming out of the paper) of the first four eigenmodes are plotted.

In order to carry out the test on the sensitivity of the KL method on the waveguide length chosen, we ran MAFIA with a number of different lengths. We also investigate the Q dependence of the agreement by varying the iris opening. The results are summarized in Fig. 2.8. Note that the points from different branch combinations are displayed in different symbols: $\diamond$ symbol for the branches 1 and 2 combination, the other symbol for the combination of branches 2 and 3. As outlined earlier, the decision on choosing the right branch combinations is based on the actual cavity excitation, as well as the frequency separation. In all these cases, the exact values are of course unknown, but a dashed line, showing the arithmetic mean of all the data points, is added, nevertheless, as an aid to the visualization of the fluctuation. This line does not have any more significance. We see roughly the same fluctuation of the result as that shown in Fig. 2.6 and 2.5. So we know it is coming out of the approximation we made in the 4-parameter representation, not from the numerical noise of the code.

The data used to determine the points in Fig. 2.8 allowed us to compare the results shown in Fig. 2.8 with two lengths single branch application of the KL method and also with two lengths two branches and four lengths single branch applications of the KY method. These results are given in Table 2.1. Comparison of the entries with one another and with the points in Fig. 2.8 shows excellent consistency.

Even though the single length two-branch calculation proves to be very successful, there are situations in which two-length calculation is preferred: for example, when no two branches of the same cavity mode can be identified from the field plot or when the frequency separation between the two branches is too large. These situations can usually be avoided by choosing a longer waveguide. But some computational limitation may prohibit this from being done, especially when there are too many extra mesh points introduced as a result of longer waveguide.

The number of mesh points in the plane of the figure in MAFIA simulation was 7896. Increasing density was used in the vicinity of the iris to better model the important field variation. Because of the two dimensional nature of the problem, only

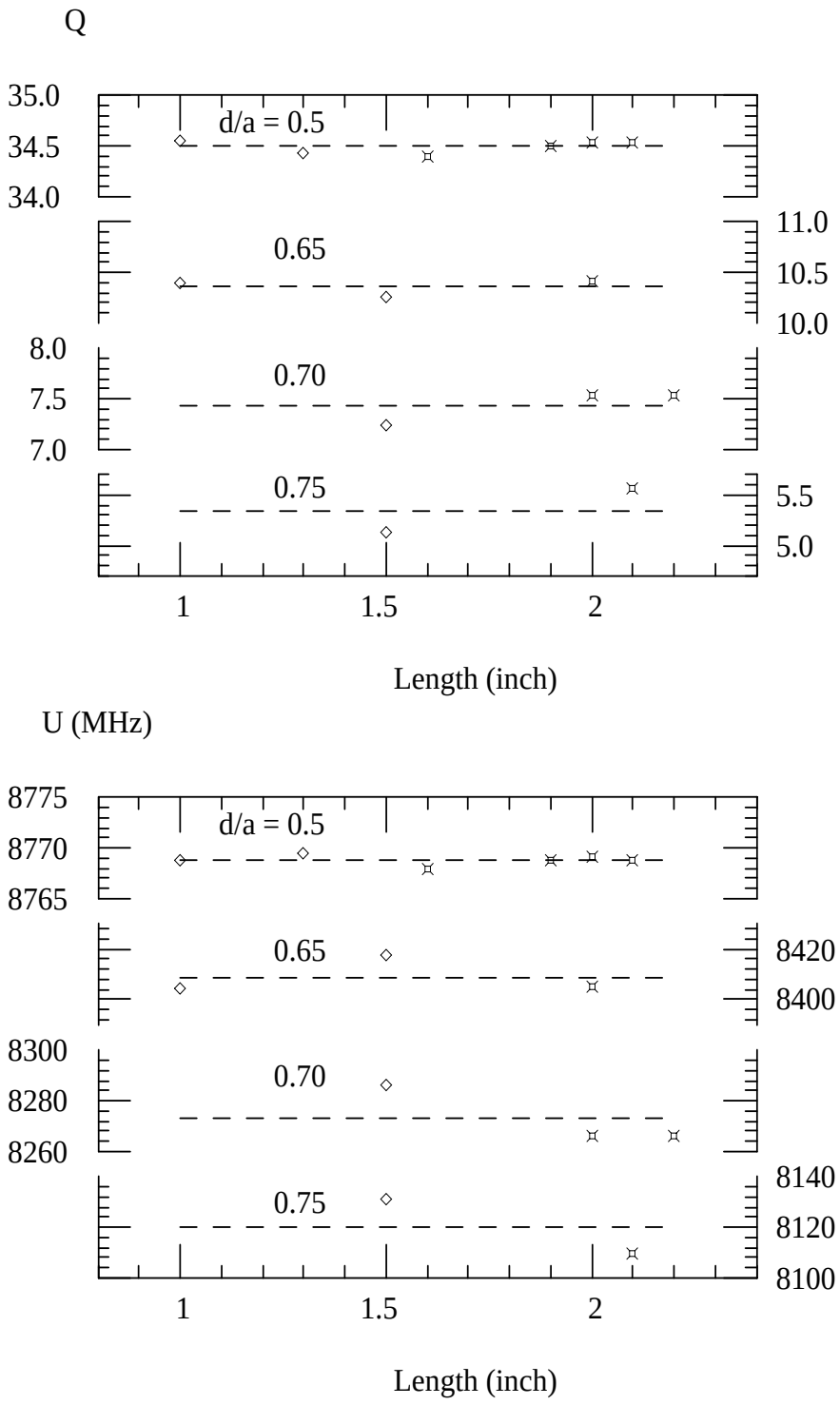

Figure 2.8: The Q_{ext}s and the resonant frequencies of the waveguide model with finite iris thickness. The R is the ratio of D and a. The symbol d is the iris opening and the dashed line represents the arithmetic mean of all the points.

$\frac{d}{a}$	frequency (MHz)	Q	Branches	Lengths(inches)	Method
0.5	8769.07	34.54	2, 3	2.0	KL
	8769.09	34.52	2	1.3, 1.9	KL
	8768.93	34.63	2, 3	2.0, 2.1	KY
	8768.84	34.59	2	1.3, 1.6, 1.9, 2.0	KY
0.65	8405.01	10.41	2, 3	2.0	KL
	8407.99	10.39	2	1.5, 2.0	KL
	8403.95	10.34	2, 3	1.5, 2.0	KY
0.70	8266.35	7.54	2, 3	2.0	KL
	8270.48	7.48	2	1.5, 2.0	KL
	8263.87	7.48	2, 3	1.5, 2.0	KY
0.75	8109.44	5.57	2, 3	2.1	KL
	8114.20	5.47	2	1.5, 2.1	KL
	8109.52	5.55	2, 3	1.5 2.1	KY

Table 2.1: Numerical comparison of the KL and the KY methods at various iris opening and waveguide shorting lengths.

two points were used in the direction perpendicular to the plane.

The consistency of the KL and the KY method is remarkably good down to $Q \sim 5$. Even lower Q has been tested; it still shows reasonable results. The KL method has also been successfully applied to very high Q (In the 10^5 range.) cases. We note that the single run KL method is particularly advantageous for high Q application. This is because high Q cases require accurate determination of small frequency difference. This can be done more reliably when one is dealing with two modes of a single lattice than when one is dealing with modes on the same branch from different lattices. The lattices must differ to some extent because the waveguide lengths are different. One of course tries to minimize the difference, but in so doing the resonant frequency differences are notably smaller than the cross branch differences, which further reduces the reliability of method requiring two or more runs.

Chapter 3

The Persistent Wakefield in Waveguide Damped Structures

3.1 Origin

The problem of describing a decaying system is of great interest to the physics community. In particle physics, almost all known elementary particles are unstable. Even in nuclear physics a considerable number of unstable (radioactive) nuclei, both naturally and artificially produced, are known. In fact, it was the desire to understand the process of radioactivity that first led physicists to the elaboration of a quantitative theory for the decay process. It goes without saying that such a theory fits nicely under quantum theory, where typical effects, like the tunneling effect, are particularly suitable to account for the dynamics of unstable systems.

The wakefield is just another form of decaying system. However, the wakefield energy in the cavity is usually very large compared with that of a quantum $\hbar\omega$, where ω is the resonant frequency of the cavity. This implies that a large number of quanta exist in the cavity, classical field theory should account for the system very well.

As described by classical theory, decay is a memoryless process. In other words, the decay probability does not depend on the history. The governing dif-

ferential equation is similar to Eq. 1.2. This is a phenomenological description of the process, since no effort is made to understand the mechanism that is responsible for the decay. However, we have to remark that Eq. 1.2 accounts very well for the experimentally observed facts.

A more detailed analysis reveals that the decay can not be exponential at long time. The argument goes as follows: If one decomposes the field in the cavity in terms of the eigenmodes of the system, it has a number of discrete modes plus a continuum of propagating modes above the cutoff of the waveguide. When the fields are added up, the result is a few sines and cosines associated with the discrete modes, plus an integral of the type:

$$A(t) = \int_{\omega_{min}}^{\infty} d\omega f(\omega) e^{-i\omega t}.$$

It is understood that the physical quantity is the real part of the above expression. An integral of the above type can not be an exponential in t. At large enough t, $A(t)$ is asymptotically proportional to $t^{-\alpha}$. This assertion can be demonstrated by integration by parts.

$$\begin{aligned} & \int_{\omega_{min}}^{\infty} d\omega f(\omega) e^{-i\omega t} \\ = & -\frac{1}{it} e^{-i\omega t} f(\omega) \mid_{\omega_{min}}^{\infty} + \frac{1}{it} \int_{\omega_{min}}^{\infty} e^{-i\omega t} f'(\omega) d\omega \\ = & \frac{1}{it} e^{-i\omega_{min} t} f(\omega_{min}) + \frac{1}{it} \int_{\omega_{min}}^{\infty} e^{-i\omega t} f'(\omega) d\omega. \end{aligned} \tag{3.1}$$

Here we have used the fact that $f(\omega \to \infty) = 0$. The leading term decays as t^{-1} if the coefficient is non-zero. If $f(\omega_{min})$ is zero, we have to repeat the process of partial integration. Not all $f^{(n)}(\omega_{min})$ can vanish for finite ω_{min}, otherwise $f(\omega)$ is identically zero everywhere[1]. It could happen that $f^{(n)}(\omega_{min}) = 0, n = 0, 1, \ldots, m-1$, but $f^{(m)}(\omega_{min}) \to \infty$. This is an indication that the integral decays as $t^{-\alpha}$, for some α with $m < \alpha < m + 1$. In fact, we shall see this situation later.

Similar phenomena have been much discussed in connection with radioactive nuclei. This power law tail has, however, never been observed for radioactive decay

[1] The fact that f is analytic and bounded in the upper half plane is enough to prove this assertion.

because its coefficient is so small that it dominates the exponential decay only after many half lives, at which time the residual decay is too weak to detect.

In this chapter, we present analytic discussions of two simple but physically realistic models which illustrate the presence of the $t^{-(n+\frac{1}{2})}$ decaying tail in addition to the usual exponentially damped mode in the transverse wakefield.

3.2 Transverse Wakefield in a Straight Waveguide

For our first example we consider a uniform rectangular waveguide excited by a beam passing through it in the z direction (see figure below). It may be thought of as an extreme limit of the waveguide model cavities studied in the previous chapter, the limit in which the irises are opened up completely.

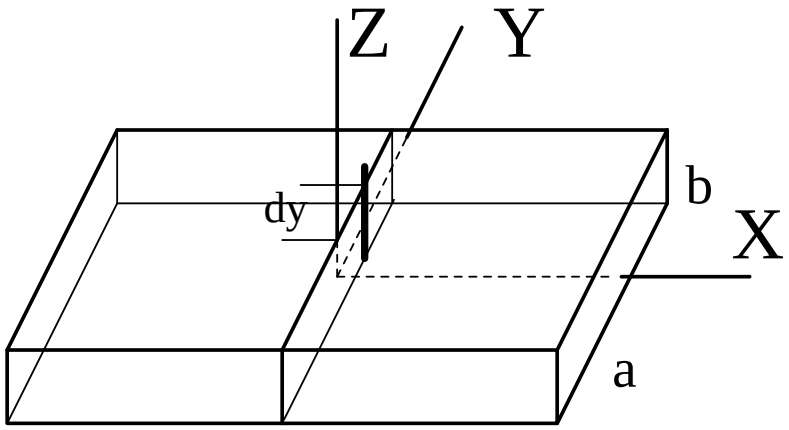

Figure 3.1: A straight waveguide going in the x direction. Beam path is off center in y direction by an amount of dy, represented by the thick line.

If a particle bunch passes through the cavity off-center in the y direction, it will excite the TE^{20} waveguide mode. A residuum of the mode remains well after the particle has left the waveguide and its H_x field at and near the origin generates a force on trailing bunches in the same direction as that of the initial transverse displacement. Hence the result of the force is to drive trailing bunches farther off axis, thereby exhibiting in its simplest form the fundamental mechanism of the transverse multi-bunch Beam Break-Up(BBU) instability.

The derivation of the wakefield uses no more than Maxwell's equations:

$$\left.\begin{aligned} \nabla \times \vec{E} &= -\tfrac{1}{c}\tfrac{\partial \vec{B}}{\partial t} \\ \nabla \cdot \vec{D} &= 4\pi\rho \\ \nabla \times \vec{H} &= \tfrac{4\pi}{c}\vec{J} + \tfrac{1}{c}\tfrac{\partial \vec{D}}{\partial t} \\ \nabla \cdot \vec{B} &= 0 \end{aligned}\right\} \tag{3.2}$$

with the linear isotropic homogeneous relations

$$\vec{D} = \epsilon\vec{E} \quad , \quad \vec{B} = \mu\vec{H}. \tag{3.3}$$

Combining the curl and divergence equations, we obtain a single equation in terms of the field $\vec{H}$,

$$\begin{aligned} \nabla \times (\nabla \times \vec{H}) &= \frac{4\pi}{c}\nabla \times \vec{J} + \frac{\epsilon}{c}\frac{\partial}{\partial t}(-\frac{\mu}{c}\frac{\partial \vec{H}}{\partial t}) \\ \frac{\epsilon\mu}{c^2}\frac{\partial^2}{\partial t^2}\vec{H} - \nabla^2\vec{H} &= \frac{4\pi}{c}\nabla \times \vec{J}. \end{aligned} \tag{3.4}$$

With a charged particle moving at velocity v, the current $\vec{J} = qv\delta(x)\delta(y - dy)\delta(z - vt)\hat{z}$, with dy the y direction offset. The field equation for H_x is

$$\frac{\epsilon\mu}{c^2}\frac{\partial^2}{\partial t^2}H_x - \nabla^2 H_x = \frac{4\pi qv}{c}\delta(x)\delta'(y - dy)\delta(z - vt). \tag{3.5}$$

With the uniform $y - z$ cross section outlined here, the field can be calculated by an expansion in terms of the eigenmodes in the regions $x < 0$ and $x > 0$. The matching condition at $x = 0$ provides the necessary equations to solve for the unknown amplitudes:

$$\left.\begin{aligned} H_x^1 &= \textstyle\sum_{mn}\int a^1_{mn}(\omega)e^{-i\omega t + il_x x}d\omega f_{mn}(y,z) \\ H_x^2 &= \textstyle\sum_{mn}\int a^2_{mn}(\omega)e^{-i\omega t - il_x x}d\omega f_{mn}(y,z) \end{aligned}\right\} \tag{3.6}$$

where the superscripts 1 and 2 denote the regions $x > 0$ and $x < 0$, respectively.

$$l_x = \sqrt{(\frac{\omega}{c})^2 - (\frac{m\pi}{a})^2 - (\frac{n\pi}{b})^2}$$

the sign of the above square root is chosen such that the field satisfies the outgoing wave boundary condition in both regions. The $f_{mn}(y,z)$ are the eigenmodes of the

waveguide cross-section.

$$f_{mn}(y,z) = \frac{1}{\sqrt{(2-\delta_{m0})a}}\cos(\frac{m\pi}{a}(y-\frac{a}{2}))\frac{1}{\sqrt{(2-\delta_{n0})b}}\cos(\frac{n\pi}{b}(z-\frac{b}{2})). \qquad (3.7)$$

These modes satisfy

$$\begin{aligned}(\frac{\partial^2}{\partial y^2}+\frac{\partial^2}{\partial z^2})f(y,z) &= \lambda f(y,z) \quad in \quad \Omega \\ \frac{\partial}{\partial n}f(y,z) &= 0 \quad on \quad ,\end{aligned}$$

where Ω is the interior of the cross section and , is the boundary. The symbol n points to the normal direction of the boundary surface, not to be confused with the index n. For later convenience, the numerical factors are chosen to normalize the eigenmodes so that $\int f_{mn}f_{m'n'}dydz = \delta_{mm'}\delta_{nn'}$.

By inspecting Eq. 3.6, the field continuity at $x=0$ immediately gives[2]

$$a^1_{mn}(\omega) = a^2_{mn}(\omega) \qquad (3.8)$$

The other condition a_{mn}'s have to satisfy comes from the (dis)continuity of the first derivative of the field. Using Eq. 3.8, we integrate Eq. 3.5 from $\int_{0^-}^{0^+} dx$ to obtain

$$\begin{aligned}-(\frac{d}{dx}H^1_x - \frac{d}{dx}H^2_x)\mid_{x=0} &= \frac{4\pi qv}{c}\delta'(y-dy)\delta(z-vt); \\ -\sum_{mn}\int 2il_x a^1_{mn}(\omega)e^{-i\omega t}d\omega f_{mn}(y,z) &= \frac{4\pi qv}{c}\delta'(y-dy)\delta(z-vt). \qquad (3.9)\end{aligned}$$

To solve for a_{mn}s, we multiply Eq. 3.9 with $f_{mn}(y,z)$ and then integrate $\int dydz$ to yield

$$\begin{aligned}&-\int 2il_x a^1_{mn}(\omega)e^{-i\omega t}d\omega \\ =\ &\frac{4\pi qv}{c}\int_{-\frac{b}{2}}^{\frac{b}{2}}\int_{-\frac{a}{2}}^{\frac{a}{2}}\delta'(y-dy)\delta(z-vt)dydz \\ =\ &\frac{4\pi qv}{c}\frac{1}{\sqrt{Z_mZ_nab}}\frac{m\pi}{a}\sin(\frac{m\pi}{a}(\frac{a}{2}+dy))\cos(\frac{n\pi}{b}(vt+\frac{b}{2})), \qquad (3.10)\end{aligned}$$

[2]Since for this problem $\nabla\cdot\vec{H}$ as well as $\nabla\cdot\vec{B}$ vanish.

where Z_m is a short notation for $2-\delta_{m0}$. We use the inverse Fourier transform to express $a^1_{mn}(\omega)$ explicitly as

$$\begin{aligned} & a^1_{mn}(\omega) \\ = & \frac{i}{2l_x}\frac{1}{2\pi}\frac{4\pi qv}{c}\frac{1}{\sqrt{Z_m Z_n ab}}\frac{m\pi}{a}\sin(\frac{m\pi}{a}(\frac{a}{2}+dy))\int_{-\frac{b}{2v}}^{\frac{b}{2v}}\cos(\frac{n\pi}{b}(vt+\frac{b}{2}))e^{i\omega t}dt \\ = & \frac{qv}{cl_x}\frac{1}{\sqrt{Z_m Z_n ab}}\frac{m\pi}{a}\sin(\frac{m\pi}{a}(\frac{a}{2}+dy))\frac{\omega}{\omega^2-\frac{n^2\pi^2}{b^2}v^2}((-)^n e^{i\frac{b}{2v}\omega}-e^{-i\frac{b}{2v}\omega}). \quad (3.11) \end{aligned}$$

We are interested in the field around the center, at the location of the beam. Setting $y=0$ yields

$$\begin{aligned} H_x(t,x,z) &= \sum_{mn}\int a^1_{mn}(\omega)e^{-i\omega t+il_x x}d\omega f_{mn}(0,z) \\ &= \sum_{mn}\int a^1_{mn}(\omega)e^{-i\omega t+il_x x}d\omega\frac{\cos(\frac{m\pi}{2})}{\sqrt{Z_m Z_n ab}}\cos(\frac{n\pi}{b}(z-\frac{b}{2})). \quad (3.12) \end{aligned}$$

Without any confusion, we will use $H_x(t,x,z)$ to denote the field at the center of the waveguide. From Eq. 3.11 and 3.12, it is easy to see that only even m contribute to $H_x(t,x,z)$. And because b is chosen to be very small, $n\neq 0$ terms will only come from high frequency components of the spectrum. Our point charge, of course, excites an infinitely wide spectrum, but it does not prevent us from taking only the low frequency part to mimic a finite length bunch for the sake of simplicity. Therefore, we will limit our attention to $n=0$ and $m=2,4,6,\ldots..$

Taking $n=0$ and $m=2$ for example, the field pattern

$$H^{20}_x(t,x)=\frac{qv}{2abc}\frac{2\pi}{a}\sin(\frac{2\pi}{a}dy)\int\frac{1}{\omega l_x}(e^{i\frac{b}{2v}\omega}-e^{-i\frac{b}{2v}\omega})e^{-i\omega t}e^{il_x x}d\omega \quad (3.13)$$

is that of the traveling TE^{20} waveguide mode. Since the $n=0$ term is independent of z, we also dropped the argument z in H^{20}_x. In writing $\omega=\frac{2\pi}{a}cx'=\omega_c x'$, where x' is a scaled dummy variable, not to be confused with coordinate x, we obtain

$$\begin{aligned} H^{20}_x(t,x) &= \frac{qv}{2abc}\sin(\frac{2\pi}{a}dy)\int\frac{dx'}{x'}(e^{i\frac{b}{2v}\omega_c x'}-e^{-i\frac{b}{2v}\omega_c x'})\frac{e^{-ix'\omega_c t}}{\sqrt{x'^2-1}}e^{i\sqrt{x'^2-1}\frac{2\pi}{a}x} \\ &= \frac{qv}{2abc}\sin(\frac{2\pi}{a}dy)\int\frac{dx'}{x'}(e^{i\frac{b}{2v}\omega_c x'}-e^{-i\frac{b}{2v}\omega_c x'})\frac{e^{-ix'\omega_c t}}{\sqrt{x'^2-1}} \\ & \qquad (i\sin(\sqrt{x'^2-1}\frac{2\pi}{a}x)+\cos(\sqrt{x'^2-1}\frac{2\pi}{a}x)). \quad (3.14) \end{aligned}$$

Before taking $x = 0$, we want to point out that the integral of the first term (involving $\sin(\sqrt{x'^2-1}\frac{2\pi}{a}x)$) above vanishes when $t > \frac{b}{2v} + \frac{x}{c}$, since the integrand is an analytic expression on the whole complex plane. Notice that $\frac{\sin(\sqrt{x'^2-1}\frac{2\pi}{a}x)}{\sqrt{x'^2-1}}$ is analytic, so is $\frac{e^{i\frac{b}{2v}\omega_c x'} - e^{-i\frac{b}{2v}\omega_c x'}}{x'}$. The path can be closed from below when $t > \frac{b}{2v} + \frac{x}{c}$. With no singularities in the contour, the integration vanishes. When $t < -\frac{b}{2v} - \frac{x}{c}$, the contour can be closed from above, the integration vanishes too[3]. In other words, this term basically represents the passage of the charge. From now on, without any confusion, we will drop this term from H_x^{20}. Remember that we are only interested in long time behavior of the wakefield near the center.

The other term in Eq. 3.14 involving $\cos(\sqrt{x'^2-1}\frac{2\pi}{a}x)$ is different. For simplicity, let us take $x = 0$; then

$$H_x^{20}(t) = \frac{qv}{2abc}\sin(\frac{2\pi}{a}dy)\int_{\omega_c(t-\frac{b}{2v})}^{\omega_c(t+\frac{b}{2v})} dx' \int dx'' \frac{ie^{-ix''x'}}{\sqrt{x''^2-1}}. \tag{3.15}$$

We have used the identity $\frac{1}{ix'}e^{ix'x''} = \int e^{ix'x''}dx''$ in deriving the above equation. The inner integral has two branch points on the complex x'' plane: ± 1. The outgoing boundary condition already defines the branch cuts, from 1 to $+\infty$ and from -1 to $-\infty$. As a result, the integration path can be detoured according to the sign of x'. When $t < -\frac{b}{2v}$, all $x' < 0$, the integration along the semi-circle in the upper half plane vanishes, and the line integral from $-\infty$ to $+\infty$ is the same as the whole contour integral. The contour integral vanishes because there is no singularities within the contour. This is the result of causality, before $t = -\frac{b}{2v}$, charge has not shown up in the waveguide yet.

When $t > \frac{b}{2v}$, all $x' > 0$, integration along the semi-circle in the lower half plane vanishes. Because the line integral can be deformed into the path in Fig. 3.2(b), subtracting zero contribution from the semi-circle yields the two branch cuts integral. Since the square root on the lower half plane path is the negative of the square root

[3]It is a little counter intuitive in noticing $t < -\frac{b}{2v} - \frac{x}{c}$ instead of $t < -\frac{b}{2v}$ as causality suggested. This is due to the fact that we split $e^{il_x x}$. The expression is still causal when we include the cos term in Eq. 3.14. This effect is not important to us because we are only interested in the field value with *very* small x.
When discussing field propagation in x direction, it is better not to split the term $e^{il_x x}$.

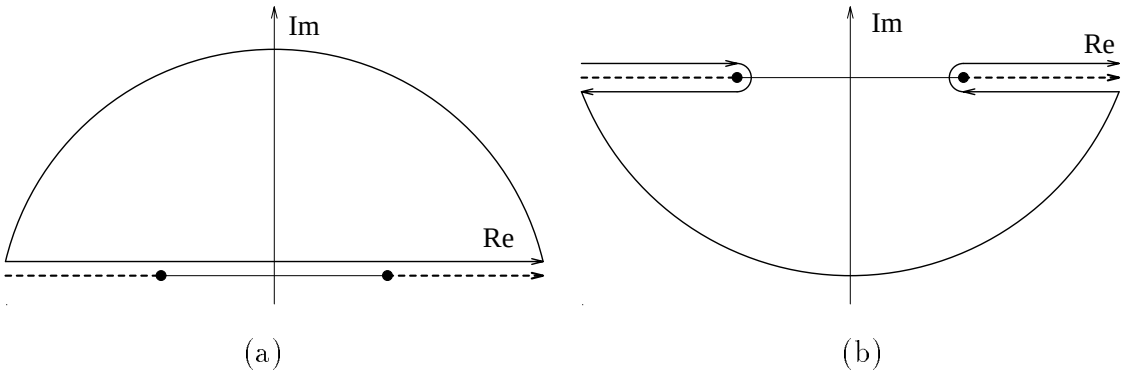

Figure 3.2: The dashed lines signify the branch cuts. (a) when $x' < 0$, the path can be closed from above. (b) when $x' > 0$, the path can be closed from below

on the upper half plane path and since the integration direction is opposite, the branch cut integral doubles the value of that from integrating a single side path. Also observing that the two branches are complex conjugate of each other, this integral is not hard to write down as

$$\begin{aligned} & \int dx'' \frac{ie^{-ix''x'}}{\sqrt{x''^2-1}} \\ = \; & 4\Re \int_1^\infty \frac{ie^{-ix''x'}}{\sqrt{x''^2-1}} dx'' \\ = \; & 4\int_1^\infty \frac{\sin(x''x')}{\sqrt{x''^2-1}} dx'' \\ = \; & 2\pi J_0(x'), \end{aligned} \tag{3.16}$$

where $J_0(x')$ is the 0th order Bessel function. As a result, $H_x^{20}(t)$ is given by

$$H_x^{20}(t) = \frac{-2qv}{Ac} \sin(\frac{2\pi}{a} d_y) \int_{\omega_c(t-\frac{b}{2v})}^{\omega_c(t+\frac{b}{2v})} \frac{\pi}{2} J_0(x')dx', \tag{3.17}$$

where $A = ab$ is the area of the waveguide cross section.

It is obvious that for large t, the field H_x decays as $t^{-1/2}$. We call it the *persistent wakefield*, in distinction with the usual exponentially decaying ones. In this particular model, we do not have a cavity mode because we do not have a cavity yet. But in general, there will be contributions from damped modes as well as the persistent wake. At large enough time, $t^{-1/2}$ exceeds $e^{-\alpha t}$ and becomes the dominant term. Also note that persistent wake oscillates at the waveguide cutoff frequency. This

supports the notion that zero group velocity component contributes to the persistent wakefield.

This model does not generate any transverse wakefield in the x direction, because it is translationally invariant in x.

3.3 Wakefield in a Dielectric Waveguide Cavity

A better model that illustrates the effect of the cavity but is still reasonably easy to solve is a straight waveguide filled with dielectric material in the middle. See Fig. 3.3.

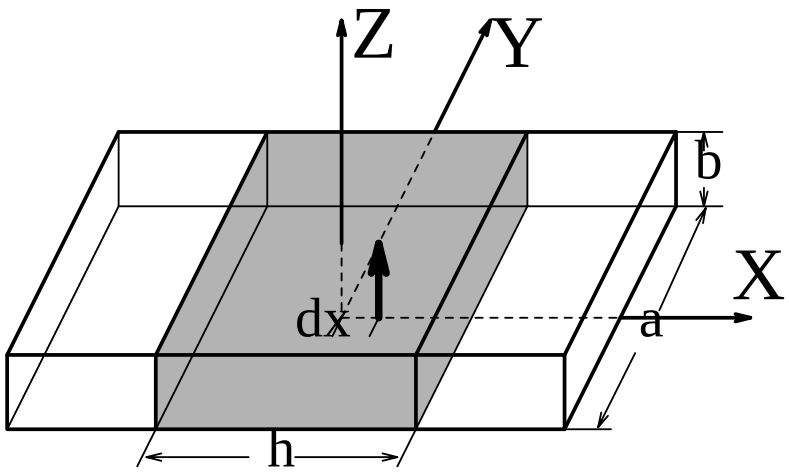

Figure 3.3: Waveguide partially filled with dielectric material, represented by shaded region. The beam passes with an offset dx in the x direction to excite the dipole of that polarization.

The dielectric constant $\epsilon > 1$ effectively enlarges the portion with the material, making it a cavity. This configuration has at least one trapped mode, much like the situation in one-dimensional potential well problem in quantum mechanics. This lowest energy trapped mode has a symmetric field distribution with respect to y-z plane, and has an electric field distribution suitable for accelerating particles in the z direction. More trapped modes are possible depending on the parameters chosen. There are also damped modes associated with multiple reflections between the two dielectric-free space interfaces that have frequencies above the cutoff of the free

space portion of the waveguide. Hence it provides us with a reasonable model of a waveguide damped accelerator cavity.

With a charged particle moving at velocity v in the z direction as indicated by the arrow in Fig. 3.3, the current $\vec{J} = qv\delta(x-dx)\delta(y)\delta(z-vt)\hat{z}$, where dx is the x direction offset. The field equation for H_x is

$$\frac{\epsilon\mu}{c^2}\frac{\partial^2}{\partial t^2}H_x - \nabla^2 H_x = \frac{4\pi q v}{c}\delta(x-dx)\delta'(y)\delta(z-vt). \tag{3.18}$$

With the uniform $y-z$ geometry outlined here, the field can be calculated by an expansion in terms of the eigenmodes in regions $x < -\frac{h}{2}$, $-\frac{h}{2} < x < dx$, $dx < x < \frac{h}{2}$, and $\frac{h}{2} < x$, denoted by superscript 4, 2, 1, and 3, respectively. The matching conditions at $x = -\frac{h}{2}$, $x = dx$, and $x = \frac{h}{2}$ provide the necessary equations to solve for the unknown amplitudes.

$$\left.\begin{array}{rcl} H_x^1 &=& \sum_{mn}\int (a^1_{mn}(\omega)e^{ik_x(x-dx)} + b^1_{mn}(\omega)e^{-ik_x(x-dx)})e^{-i\omega t}d\omega f_{mn}(y,z) \\ H_x^2 &=& \sum_{mn}\int (a^2_{mn}(\omega)e^{ik_x(x-dx)} + b^2_{mn}(\omega)e^{-ik_x(x-dx)})e^{-i\omega t}d\omega f_{mn}(y,z) \\ H_x^3 &=& \sum_{mn}\int c^1_{mn}(\omega)e^{il_x(x-\frac{h}{2})}e^{-i\omega t}d\omega f_{mn}(y,z) \\ H_x^4 &=& \sum_{mn}\int c^2_{mn}(\omega)e^{-il_x(x+\frac{h}{2})}e^{-i\omega t}d\omega f_{mn}(y,z) \end{array}\right\} \tag{3.19}$$

where $k_x = \sqrt{\mu\epsilon(\frac{\omega}{c})^2 - (\frac{m\pi}{a})^2 - (\frac{n\pi}{b})^2}$, $l_x = \sqrt{(\frac{\omega}{c})^2 - (\frac{m\pi}{a})^2 - (\frac{n\pi}{b})^2}$. Because of the material interface at $x = \pm\frac{h}{2}$, regions 1 and 2 have waves going in both directions, while regions 3 and 4 only have outgoing waves.

First, the B_x field has to be continuous across the interface $x = -\frac{h}{2}$, $x = dx$, and $x = \frac{h}{2}$ (See the footnote on page 28). It immediately gives

$$\left.\begin{array}{rcl} a^1_{mn} + b^1_{mn} &=& a^2_{mn} + b^2_{mn} \\ a^1_{mn}e^{ik_x(\frac{h}{2}-dx)} + b^1_{mn}e^{-ik_x(\frac{h}{2}-dx)} &=& \frac{1}{\mu}c^1_{mn} \\ a^2_{mn}e^{ik_x(-\frac{h}{2}-dx)} + b^2_{mn}e^{-ik_x(-\frac{h}{2}-dx)} &=& \frac{1}{\mu}c^2_{mn} \end{array}\right\} \tag{3.20}$$

Next, by integrating Eq. 3.18 from x^- to x^+ at $x = -\frac{h}{2}$ and at $x = \frac{h}{2}$, continuity of $\frac{dH_x}{dx}$

$$\left.\begin{array}{rcl} a^1_{mn}e^{ik_x(\frac{h}{2}-dx)} - b^1_{mn}e^{-ik_x(\frac{h}{2}-dx)} &=& \frac{l_x}{k_x}c^1_{mn} \\ a^2_{mn}e^{ik_x(-\frac{h}{2}-dx)} - b^2_{mn}e^{-ik_x(-\frac{h}{2}-dx)} &=& -\frac{l_x}{k_x}c^2_{mn} \end{array}\right\} \tag{3.21}$$

follows because no source is present.

The last condition the unknown amplitudes have to satisfy comes from the (dis)continuity of the first derivative of H_x at $x = dx$ due to the delta function source term. Integrating Eq. 3.18 from dx^- to dx^+, we obtain

$$\begin{aligned} & \frac{4\pi qv}{c}\delta'(y)\delta(z-vt) \\ = & -(\frac{d}{dx}H_x^1 - \frac{d}{dx}H_x^2) \mid_{x=dx} \\ = & -\sum_{mn}\int ik_x(a_{mn}^1(\omega) - b_{mn}^1(\omega) - a_{mn}^2(\omega) + b_{mn}^2(\omega))e^{-i\omega t}d\omega f_{mn}(y,z). \quad (3.22) \end{aligned}$$

To simplify Eq. 3.22, we multiply it by $f_{mn}(y,z)$, integrate over the $y-z$ cross-section and apply the inverse Fourier transform in t. We then have

$$\begin{aligned} & a_{mn}^1(\omega) - b_{mn}^1(\omega) - a_{mn}^2(\omega) + b_{mn}^2(\omega) \\ = & \frac{2qv}{ck_x}\frac{1}{\sqrt{Z_mZ_nab}}\frac{m\pi}{a}\sin(\frac{m\pi}{2})\frac{\omega}{\omega^2 - \frac{n^2\pi^2}{b^2}v^2}((-)^n e^{i\frac{b}{2v}\omega} - e^{-i\frac{b}{2v}\omega}) \equiv \frac{\alpha_{mn}}{k_x}. \quad (3.23) \end{aligned}$$

Note that α_{mn} is analytic everywhere.

Solving Eqs. 3.20, 3.21 and 3.23 simultaneously gives us all the amplitudes:

$$a_{mn}^1 = \frac{1}{2}\frac{\alpha_{mn}(k_x+l_x\mu)[e^{-ik_xh}(k_x+l_x\mu) + e^{2ik_xdx}(k_x-l_x\mu)]}{4k_x[-ik_x\sin(k_x\frac{h}{2}) + l_x\mu\cos(k_x\frac{h}{2})][k_x\cos(k_x\frac{h}{2}) - il_x\mu\sin(k_x\frac{h}{2})]}; \quad (3.24)$$

$$b_{mn}^1 = \frac{1}{2}\frac{\alpha_{mn}(k_x-l_x\mu)[e^{-2ik_xdx}(k_x+l_x\mu) + e^{ik_xh}(k_x-l_x\mu)]}{4k_x[-ik_x\sin(k_x\frac{h}{2}) + l_x\mu\cos(k_x\frac{h}{2})][k_x\cos(k_x\frac{h}{2}) - il_x\mu\sin(k_x\frac{h}{2})]}; \quad (3.25)$$

$$a_{mn}^2 = \frac{1}{2}\frac{\alpha_{mn}(k_x-l_x\mu)[e^{2ik_xdx}(k_x+l_x\mu) + e^{ik_xh}(k_x-l_x\mu)]}{4k_x[-ik_x\sin(k_x\frac{h}{2}) + l_x\mu\cos(k_x\frac{h}{2})][k_x\cos(k_x\frac{h}{2}) - il_x\mu\sin(k_x\frac{h}{2})]}; \quad (3.26)$$

$$b_{mn}^2 = \frac{1}{2}\frac{\alpha_{mn}(k_x+l_x\mu)[e^{-ik_xh}(k_x+l_x\mu) + e^{-2ik_xdx}(k_x-l_x\mu)]}{4k_x[-ik_x\sin(k_x\frac{h}{2}) + l_x\mu\cos(k_x\frac{h}{2})][k_x\cos(k_x\frac{h}{2}) - il_x\mu\sin(k_x\frac{h}{2})]}; \quad (3.27)$$

$$c_{mn}^1 = \frac{\mu\alpha_{mn}[e^{-ik_x(\frac{h}{2}+dx)}(k_x+l_x\mu) + e^{ik_x(\frac{h}{2}+dx)}(k_x-l_x\mu)]}{4[-ik_x\sin(k_x\frac{h}{2}) + l_x\mu\cos(k_x\frac{h}{2})][k_x\cos(k_x\frac{h}{2}) - il_x\mu\sin(k_x\frac{h}{2})]}; \quad (3.28)$$

$$c_{mn}^2 = \frac{\mu\alpha_{mn}[e^{-ik_x(\frac{h}{2}-dx)}(k_x+l_x\mu) + e^{ik_x(\frac{h}{2}-dx)}(k_x-l_x\mu)]}{4[-ik_x\sin(k_x\frac{h}{2}) + l_x\mu\cos(k_x\frac{h}{2})][k_x\cos(k_x\frac{h}{2}) - il_x\mu\sin(k_x\frac{h}{2})]}. \quad (3.29)$$

By substituting the solutions back into Eq. 3.19, the field H_x^2 can be written explicitly in the following equation,

$$H_x^2 = \sum_{mn} \int \frac{1}{2} \frac{\alpha_{mn}\{\cos(k_x x)D_2 - k_x \sin(k_x x)D_1\}\{\cos(k_x dx)D_2 + k_x \sin(k_x dx)D_1\}}{k_x^2 \quad D_1 \quad D_2} e^{-i\omega t} d\omega f_{mn}(y,z) \tag{3.30}$$

where

$$D_1 = [k_x \sin(k_x \frac{h}{2}) + i l_x \mu \cos(k_x \frac{h}{2})]; \tag{3.31}$$

$$D_2 = [k_x^2 \cos(k_x \frac{h}{2}) - i l_x k_x \mu \sin(k_x \frac{h}{2})]. \tag{3.32}$$

3.3.1 Analytic Properties

In order to evaluate the integral in Eq. 3.30, it is important to understand the analytic structure of the integrand on the complex ω plane. We start with the expression

$$l_x = \sqrt{(\frac{\omega}{c})^2 - (\frac{m\pi}{a})^2 - (\frac{n\pi}{b})^2}.$$

To simplify the notation, we shall write $l_x = \frac{1}{c}\sqrt{\omega^2 - \omega_c^2}$. The meaning of ω_c is apparent. From the definition of l_x, there are two branch points at $\pm\omega_c$ associated with the square root. A careful inspection on the expression D_1 and D_2 confirms that the integrand in Eq. 3.30 indeed has branch points at these two locations. On the other hand, square root in k_x does not give rise to singularities because the integrand is even in k_x, i.e. the integrand does not change when $k_x \mapsto -k_x$. Also there is no singularity at $k_x = 0$. The singularities on the real axis, however, prevent simple-minded contour closure in evaluating the integral because branch cuts have to be drawn. Drawing the contour is related to choosing the right sign for the square root. It is normally referred to as choosing the outgoing wave boundary condition in this context. What it really means is that by writing the field in the region 3 (see Eq. 3.19) in terms of $e^{il_x x - i\omega t}$, we choose l_x positive real when ω is positive (of course, when ω is bigger than ω_c.) and choose l_x negative real when ω is negative (of course, when

ω is smaller than $-\omega$.). This is done by lifting the integration path $(-\infty, \infty)$ a little bit above real axis. Thus,

$$l_x = \sqrt{(\omega + i\epsilon)^2 - \omega_c^2} = \sqrt{\omega^2 - \omega_c^2 + 2i\epsilon\omega}$$

where ϵ is an infinitesimally small positive number [4].

Now let us return back to the Eq. 3.30. The singularities of the integrand depend on D_1 and D_2. The rest of the expression is analytic. To simplify the discussion, we assume x and dx very small so that we do not have to think about them in the next statement. When $t < -\frac{b}{2v}$, the source has not appeared yet, causality requires the integral to be zero. The integrand vanishes on the big semi-circle in the upper half plane because of the factor $e^{-i\omega t}$ [5]. Adding the two paths, the whole contour integral vanishes. The vanishing contour integral gives the well known result that the upper plane is free of any singularities. It is usually referred to as the requirement of causality.

Before we cite time reversal property, let us paint the physical picture of the whole process: Before time $-\frac{b}{2v}$, there is no field in the cavity; after time $-\frac{b}{2v}$, there are fields in the cavity and waves *going out of* the waveguide.

Because the governing differential equations involve second order derivative in time only, the process is invariant under operation $t \mapsto -t$. The time reversal produces a process like this: before time $\frac{b}{2v}$, there are fields in the cavity and waves *coming into* the waveguide; after time $\frac{b}{2v}$, there is nothing left. It is graphically illustrated in Fig. 3.4

To be more precise, we proceed with the underlying differential equation:

$$\frac{\epsilon\mu}{c^2}\frac{\partial^2}{\partial t^2}H_x - \nabla^2 H_x = \begin{cases} \frac{4\pi q v}{c}\delta(x - dx)\delta'(y)\delta(z - vt) & -\frac{b}{2v} < t < \frac{b}{2v} \\ 0 & \text{otherwise} \end{cases} . \qquad (3.33)$$

The exact form of the current term is irrelevant. However, we write it out explicitly to

[4] "sign" of l_x is automatically defined in the region $-\omega_c < \omega < \omega_c$ once we have done that.

[5] That is why we avoid the divergence of $\sin k_x x$ and $\cos k_x dx$ etc. on the complex ω plane by assuming x and dx very small. Causality still works out, but more tediously.

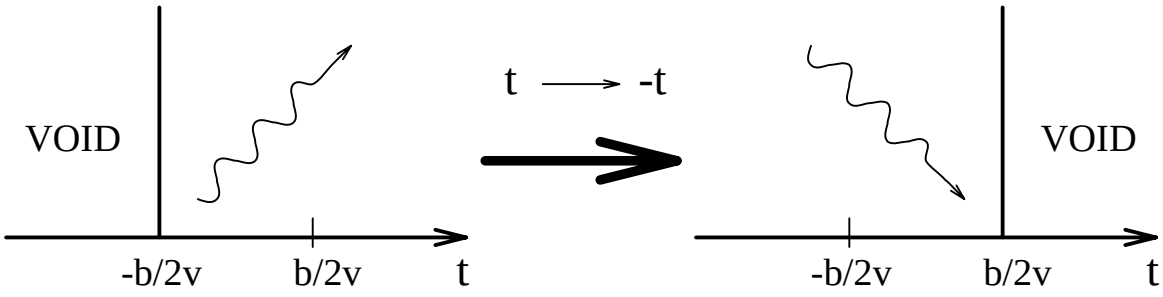

Figure 3.4: Time reversal.

facilitate further discussion. The solution of Eq. 3.33 is subject to the initial condition

$$H_x(t_0,x,y,z)=\chi_0(x,y,z)\quad,\quad \frac{\partial}{\partial t}H_x(t_0,x,y,z)=\chi_1(x,y,z),$$

and *outgoing wave boundary condition*. As a special case, the problem we solved in the previous section has $\chi_0(x,y,z)=\chi_1(x,y,z)=0$. The solution can be expressed in terms of an integral

$$H_x(t,x,y,z)=\int \beta(\omega)e^{-i\omega t}d\omega. \tag{3.34}$$

The arguments x, y, and z in β are suppressed for convenience.

Now we take the same differential equation, and solve another problem,

$$\frac{\epsilon\mu}{c^2}\frac{\partial^2}{\partial t'^2}H'_x-\nabla^2 H'_x=\begin{cases}-\frac{4\pi q v}{c}\delta(x-dx)\delta'(y)\delta(z+vt') & -\frac{b}{2v}<t'<\frac{b}{2v}\\ 0 & \text{otherwise}\end{cases}, \tag{3.35}$$

where we use "$\prime$" to denote a different field and a different time. Comparing Eqs. 3.33 and 3.35 we see an overall change of the sign of v. If we take the initial condition at time $t'_1=-t_1$, with $t_1>\frac{b}{2v}$, as

$$H'_x(t'_1,x,y,z)=-H_x(t_1,x,y,z)\quad,\quad \frac{\partial}{\partial t'}H'_x(t'_1,x,y,z)=\frac{\partial}{\partial t}H_x(t_1,x,y,z),$$

and subject the solution H'_x to *incoming wave boundary condition*, we will show below, that $H'_x(t',x,y,z)=-H_x(-t,x,y,z)$ is the solution. First it obviously satisfies initial conditions. Second, we have

$$\begin{aligned}&\frac{\epsilon\mu}{c^2}\frac{\partial^2}{\partial t^2}H'_x(t,x,y,z)-\nabla^2 H'_x(t,x,y,z)\\ =\;&-(\frac{\epsilon\mu}{c^2}\frac{\partial^2}{\partial t^2}H_x(-t,x,y,z)-\nabla^2 H_x(-t,x,y,z))\\ =\;&-\frac{4\pi q v}{c}\delta(x-dx)\delta'(y)\delta(z+vt).\end{aligned} \tag{3.36}$$

The third line follows from Eq. 3.33. Incoming wave boundary condition is also satisfied by noting the sign change of t.

Following the same procedure of getting Eq. 3.34 (we will take care of incoming wave boundary condition later), we can also write

$$H'_x(t', x, y, z) = \int \beta'(\omega) e^{-i\omega t'} d\omega. \tag{3.37}$$

The difference in Eq. 3.37 and Eq. 3.34 is from the initial condition and current source term, it does not affect the analytical property of the integrand due to the structure, i.e. the poles of the differential operator.

Instead of outgoing wave boundary condition, Eq. 3.37 has incoming wave boundary condition. It amounts to mapping $l_x \mapsto -l_x$. We could accomplishing this by drawing the branch cut from $-\infty$ to $-\omega_c$ and ω_c to ∞. Here, we observe that by taking the integration path a little bit below the real axis, l_x changes sign[6].

$$l_x = \frac{1}{c}\sqrt{(\omega - i\epsilon)^2 - \omega_c^2}$$

See Fig. 3.5. At time $t > \frac{b}{2v}$, The line integral from $-\infty - i\epsilon$ to $\infty - i\epsilon$ is zero as

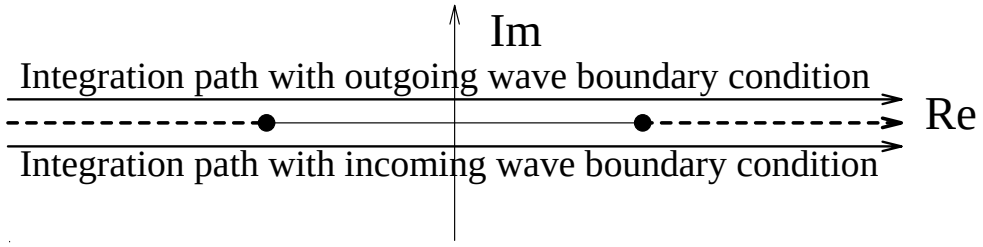

Figure 3.5: The integration path with incoming wave boundary condition.

we know already from $H'_x(t) = -H_x(-t)$. The integral along the big semi-circle in the lower half plane vanishes because of the factor $e^{-i\omega t}$. By adding the two integrals together, the vanishing contour integral shows that $\beta'(\omega)$ has no singularity in the lower half plane.

Since $\beta(\omega)$ and $\beta'(\omega)$ have the same poles on the sheet defined by Fig. 3.5, $\beta(\omega)$ also has no poles in the lower half plane. Poles can only reside on the real axis or on the second sheet defined by the branch cuts.

[6]It changes sign when crossing branch cut once.

The plane defined by the above branch cut is usually called the physical sheet. The other plane approached by crossing the branch cut once is called unphysical sheet. In order to see the unphysical sheet, we will rotates the branch cut associated with $-\omega_c$ counter clockwise by 180^o. so it looks like Fig. 3.6. Where the shaded region

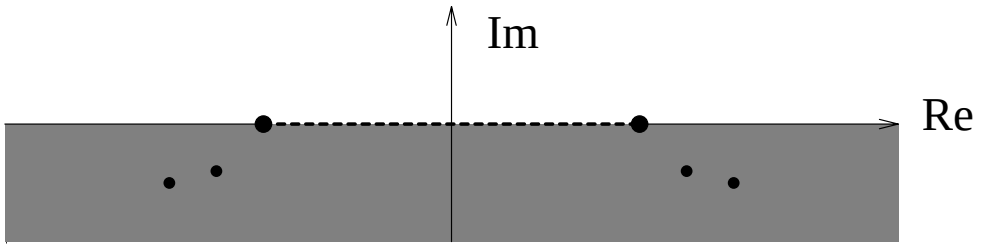

Figure 3.6: Branch cut to reveal the unphysical sheet poles.

represents the lower half plane of the unphysical sheet. The branch cut is reduced to the segment from $-\omega_c$ to ω_c. One can think of it as that crossing the line (ω_c, ∞) is equivalent to crossing two branch cuts; it does not change anything. Therefore, no branch cut discontinuity is present in (ω_c, ∞). At $t > \frac{b}{2v}$, the integration path in Eq. 3.34, or more precisely, Eq. 3.30 can be closed in the lower half plane. In shrinking the contour to the one around the branch cut, the resulting integration includes two types of contribution: one from the branch cut integral, the other from passing through *all* the poles in the lower half plane, as illustrated in Fig. 3.7.

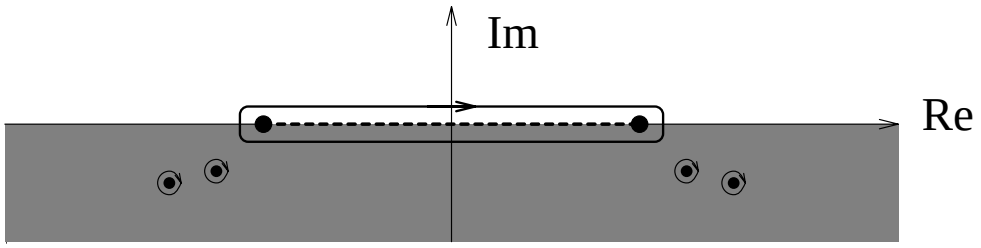

Figure 3.7: Contour integral to include the unphysical sheet poles.

Eq. 3.34 becomes

$$H_x(t) = \oint \beta(\omega) e^{-i\omega t} d\omega + \sum_i \gamma_i e^{-i\omega_i t}. \tag{3.38}$$

The meaning of each term is self-explanatory. Since H_x is real, the poles necessarily appear in group of two with $\omega_i = -\omega_j^*$ to ensure reality, where $*$ is the complex conjugate. It appears as natural that the resonant frequency ω_i is complex, with negative imaginary part, so that each term under the summation decays exponentially. They are then interpreted as the decaying modes.

On the other hand, we could do a similar maneuver to the expression in Eq. 3.37. This time, we rotate the branch cut associated with $-\omega_c$ clockwise 180^o, so that the upper half plane of the unphysical sheet is revealed. See Fig. 3.8. At

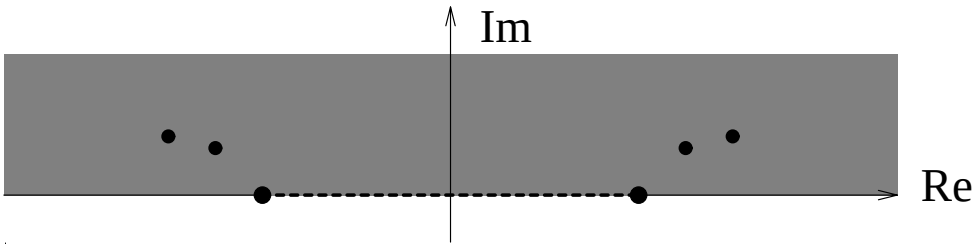

Figure 3.8: Branch cut to reveal the unphysical sheet poles.

$t < -\frac{b}{2v}$, the integration path (-$\infty - i\epsilon, \infty - i\epsilon$) can be closed from above. Similarly, the contour integration is reduced to a branch cut integral plus pole integrals, as shown in Fig. 3.9.

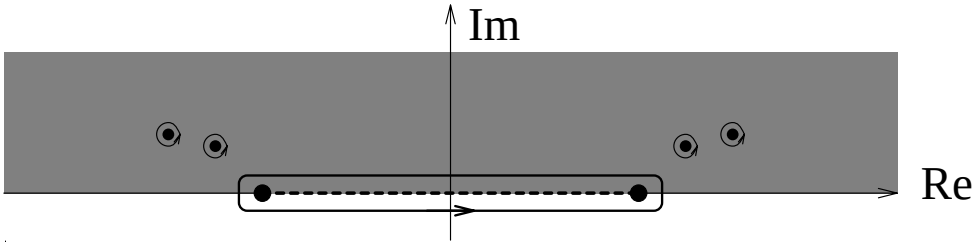

Figure 3.9: Contour integral to include the unphysical sheet poles.

Eq. 3.37 then becomes

$$H_x'(t) = \oint \beta'(\omega) e^{-i\omega t} d\omega + \sum_i \gamma_i' e^{-i\omega_i' t}. \tag{3.39}$$

The imaginary part of the resonant frequency ω_i' is positive, giving rise to a growing mode, which is expected from the incoming wave boundary condition. From

the time reversal aspect, not only the real part of the ω_i' has to equal the real part of the ω_i, but the imaginary part of the ω_i' has to equal the negative of the imaginary part of the ω_i. i.e.

$$\omega_i^* = \omega_i'.$$

Hence we conclude that the poles on the second sheet are symmetric with respect to both real and imaginary axes.

With the explicit expression of D_1 and D_2, in Eq. 3.30, it is straightforward to verify these assertions. In order to explain the point, we will take a digression on the calculation of the square root.

Most programs (numerical or theoretical) implement the square root calculation as

$$\sqrt{re^{i\theta}} = \sqrt{r}e^{i\frac{\theta}{2}} \tag{3.40}$$

where $-\pi < \theta < \pi$ and $r > 0$. This is equivalent to taking the branch cut from $-\infty$ to 0. This particular choice has the property

$$\sqrt{x^*} = (\sqrt{x})^*, \tag{3.41}$$

while cuts anywhere else do not preserve this identity. For example, with cut from 0 to ∞, we could define

$$\sqrt{re^{i\theta}} = \sqrt{r}e^{i\frac{\theta}{2}}$$

where $0 < \theta < 2\pi$. Then $\sqrt{x^*} = -(\sqrt{x})^*$, since

$$\sqrt{(e^{i\theta})^*} = \sqrt{e^{i(2\pi-\theta)}} = e^{i(\pi-\frac{\theta}{2})} = -e^{\frac{-i\theta}{2}}$$

The above observation leads us to a more precise definition of $l_x(\omega)$. With the branch cut we outline in the previous section

$$l_x(\omega) = \sqrt{\omega - \omega_c}\sqrt{\omega + \omega_c} = i\sqrt{\omega_c - \omega}\sqrt{\omega + \omega_c} \tag{3.42}$$

where the $\sqrt{}$ is defined in accordance with Eq. 3.40. On the unphysical sheet, the definition of l_x is changed by an overall minus sign. The first square root results in

the branch cut from ω_c to ∞, and the second square root leaves the branch cut from $-\infty$ to $-\omega_c$. It is then obvious that

$$l_x(\omega^*) = -l_x^*(\omega). \tag{3.43}$$

The minus comes from the i in Eq. 3.42. We also have $l_x(-\omega) = l_x(\omega)$.

These relations hold on both sheets, it being understood that the left and right sides always refer to the same sheet.

It is then easy to see by inspection that

$$\begin{aligned} D_1(\omega^*) = D_1^*(\omega) \quad &, \quad D_1(-\omega) = D_1(\omega), \\ D_2(\omega^*) = D_2^*(\omega) \quad &, \quad D_2(-\omega) = D_2(\omega). \end{aligned}$$

Hence if ω_i is a root of D_i on one of the sheets, then, on the same sheet, $-\omega_i$, ω_i^*, and $-\omega_i^*$ are also roots. Thus the location of the roots of D_i and hence poles of $\beta(\omega)$ is symmetric with respect to both the real and imaginary axes. Also the absence of of roots on the upper half plane of the physical sheet implies the absence of roots on the lower half plane.

Before we look into the poles on the real axis, it is instructive to see what all these terms in Eq. 3.30 mean, and have some insight into why there are poles on the real axis.

The Eq. 3.30 can be written in the form

$$\sum_{mn} \int \frac{\alpha_{mn} i}{2} \{ \frac{\sin(k_x(dx - x))}{k_x} + \frac{\cos(k_x x)\cos(k_x dx)}{k_x^2} \frac{D_2}{D_1} - \sin(k_x x)\sin(k_x dx) \frac{D_1}{D_2} \}$$
$$e^{-i\omega t} d\omega f_{mn}(y, z)$$

The term with no denominator on the right hand side of Eq. 3.30 is

$$\sum_{mn} \int \frac{\alpha_{mn} i}{2} \frac{\sin(k_x(dx - x))}{k_x} e^{-i\omega t} d\omega f_{mn}(y, z). \tag{3.44}$$

The integrand of this expression is an analytical function on the whole complex ω plane, with no singularities. Based on the same argument as on page 30, this term

represents beam passage, it does not give any contribution shortly after the beam leaves the cavity. We shall ignore this term from now on.

Now H_x^2 is reduced to

$$H_x^2 = \sum_{mn} \int \frac{\alpha_{mn} i}{2} \{ \frac{\cos(k_x x)\cos(k_x dx)}{k_x^2} \frac{D_2}{D_1} - \sin(k_x x)\sin(k_x dx) \frac{D_1}{D_2} \} e^{-i\omega t} d\omega f_{mn}(y,z). \tag{3.45}$$

It is interesting to note that the first term in Eq. 3.45 represents a field which is symmetric with respect to the plane $x = 0$ (notice the $\cos k_x x$ term.), and the excitation of the field is proportional to $\cos k_x dx$. By the same token, the second term represents an antisymmetric field.

As suggested earlier, the poles of D_1 on the real axis of the physical sheet give rise to a trapped symmetric field, while poles on the complex plane of the unphysical sheet result in an exponentially damped symmetric field. Similarly, poles of D_2 contribute to the antisymmetric field.

Taking the expression of D_1 in Eq. 3.31, for example, we only need to look at the positive real axis as a result of the left-right symmetry on the complex plane. Further more, D_1 can not have any roots in the intervals $(0,\ \frac{\omega_c}{\sqrt{\mu\epsilon}})$ and $(\omega_c,\ \infty)$: In the interval $(0,\ \frac{\omega_c}{\sqrt{\mu\epsilon}})$, $k_x \sin k_x \frac{h}{2} < 0$, and $i l_x \mu \cos k_x \frac{h}{2} < 0$; in the interval $(\omega_c,\ \infty)$, $k_x \sin k_x \frac{h}{2}$ is real while $i l_x \mu \cos k_x \frac{h}{2}$ is imaginary. As a result, the expression D_1 can never be zero. Therefore, we confine our attention to the interval $(\frac{\omega_c}{\sqrt{\mu\epsilon}},\ \omega_c)$.

With $\omega \in (\frac{\omega_c}{\sqrt{\mu\epsilon}}, \omega_c)$, we have $l_x = i\sqrt{\omega_c^2 - \omega^2}$. The roots of D_1 satisfy

$$k_x \sin(k_x \frac{h}{2}) = \frac{\mu}{c} \sqrt{\omega_c^2 - \omega^2} \cos(k_x \frac{h}{2}). \tag{3.46}$$

It is easier to write everything in terms of $k_x = \frac{1}{c}\sqrt{\mu\epsilon\omega^2 - \omega_c^2}$. Notice that k_x is in the range $(0,\ \frac{\omega_c}{c}\sqrt{\mu\epsilon - 1})$. Eq. 3.46 then reduces to

$$k_x \tan(k_x \frac{h}{2}) = \sqrt{\frac{\mu}{\epsilon}} \sqrt{\frac{{\omega_c}^2}{c}(\mu\epsilon - 1) - k_x^2}. \tag{3.47}$$

In order to work with dimensionless quantities, we scale k_x by $\frac{\omega_c}{c}$, i.e. $k_x \mapsto \frac{k_x c}{\omega_c}$, and $h \mapsto \frac{h\omega_c}{c}$. It is equivalent to choosing our own length unit as $\frac{c}{\omega_c}$. We finally arrive at

this transcendental equation

$$k_x \tan(k_x \frac{h}{2}) = \sqrt{\frac{\mu}{\epsilon}}\sqrt{(\mu\epsilon - 1) - k_x^2}. \tag{3.48}$$

Since the root can not be expressed in terms of elementary functions, the solution is displayed graphically in Fig. 3.10. The thick gray solid lines represent the left hand side of the Eq. 3.48. The vertical line is an artifact of the plotting program trying to connect different branches of the tan curve. It is worth noting that the curve starts from 0 at $k_x = 0$ and monotonically increases to $+\infty$ at $k_x \frac{h}{2} = \frac{\pi}{2}$[7]. The thin solid lines represent the right hand side of the Eq. 3.48. It starts from $\sqrt{\frac{\mu}{\epsilon}}\sqrt{\mu\epsilon - 1}$ at $k_x = 0$ and monotonically decreases to 0 at the other end of the range of k_x, $\sqrt{\mu\epsilon - 1}$. These two curves have at least *one* intersection by noting their respective monotonicity, no matter how small h is, or for that matter, how small μ and ϵ are, as long as $\mu\epsilon > 1$. The exact same equation is involved in the one dimensional potential well problem in quantum mechanics. No matter how small and shallow the well is, there is always a ground state energy below 0. The wave function is also symmetric.

Whether there are more trapped modes depends on the parameters chosen. We have chosen $\mu = 10$, $\epsilon = 1$, $h = 1$ in Fig. 3.10(a), and only one trapped mode is present. We also plotted the case with $h = 3$ in Fig. 3.10(b), where a second trapped mode does appear. To add to our understanding of how the trapped modes appear, it is beneficial to add a third curve to the plot, the dashed lines representing the negative of the solid thin lines. In the previous discussion we have emphasized that to cross a branch cut once will reach the unphysical sheet from the physical sheet and vice versa. Numerically, it is the same as changing $l_x(\omega)$ into $-l_x(\omega)$. Thus, the intersections of the thick gray curves with the dashed lines are the real roots of D_1 on the unphysical sheet. The Fig. 3.10(b) shows that there is a real pole on the unphysical sheet associated with the second trapped mode, by "associated" we mean they are from the same branch of the tan curve. By decreasing h, the whole thick gray curves scale horizontally to the far right, while the solid and dashed thin lines

[7] k_x may not be able to take that value if h is too small, but for the following discussion, the monotonicity is enough.

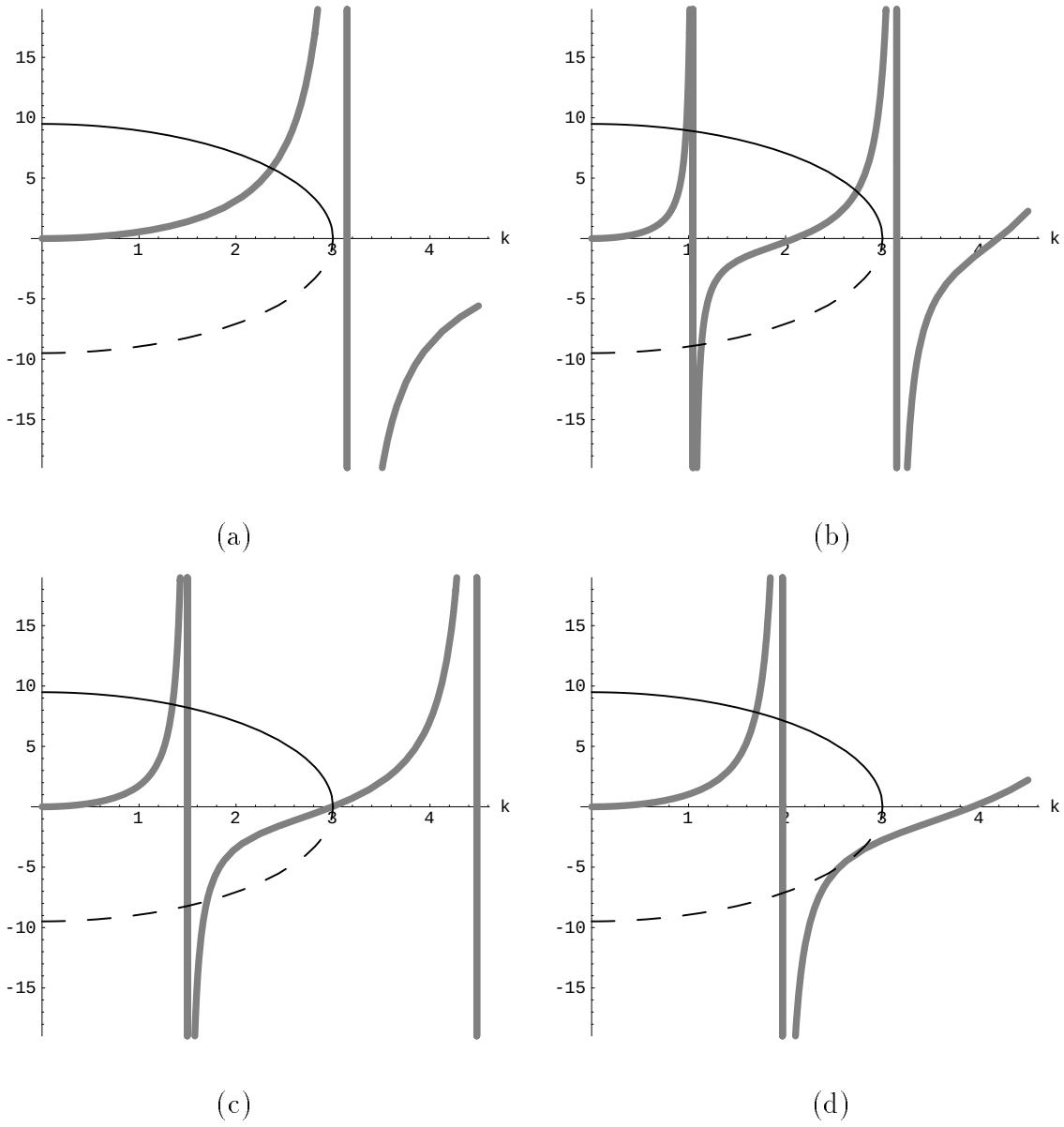

Figure 3.10: A graphical display of solutions to Eq. 3.48. The thick gray solid lines represent the left hand side of the Eq. 3.48, the solid thin lines represent the right hand side of the Eq. 3.48. The dashed line is the negative of the solid thin curve.

stay the same. As a result, the intersections move to the right, i.e. the frequency of the root moves up.

At around $h = 2.1$, to be precise, $h = \frac{2\pi}{\sqrt{\frac{\mu}{\epsilon}}\sqrt{\mu\epsilon-1}}$, (see Fig. 3.10(c).) the two curves intersect at k_x^{max}, which is ω_c if we write the root in terms of frequency. Thus, the pole coincides with the branch point. When we further decrease h, the real pole on the physical sheet moves on to the unphysical sheet and moves towards lower frequency, while the other pole moves towards higher frequency until the two poles associated with the same branch collide as illustrated on Fig. 3.10(d). It is about $h = 1.6$. Further decrease of h moves the poles into the complex plane, one above the real axis, one below, as required by the symmetry.

The number of trapped modes N is then related to $k_x^{max}\frac{h}{2}$, the phase advance in the dielectric material at ω_c, by

$$N = ceiling(\frac{h\sqrt{\mu\epsilon-1}}{2\pi}) \tag{3.49}$$

where $ceiling(x) = \min\{n | n \geq x,\ integer\ n\}$.

The poles of D_2 which satisfy

$$k_x \cot(k_x\frac{h}{2}) = \mp\sqrt{\frac{\mu}{\epsilon}}\sqrt{(\mu\epsilon-1)-k_x^2} \tag{3.50}$$

have a similar movement on the complex plane. The minus and plus sign correspond to the real roots on the physical and unphysical sheet, respectively. We have chosen several sets of parameters to solve for the roots. They are shown in Fig. 3.11. The curves have similar meanings as those in Fig. 3.10.

The intersection of the thick gray line and the dashed line in Fig. 3.11(a), representing a real pole on the unphysical sheet, moves toward the branch point as we increase h. At $h = \frac{\pi}{\sqrt{\mu\epsilon-1}}$, the real pole is at ω_c (see Fig. 3.11(b)) and any further increasing of h brings the pole on to the physical sheet to become a trapped mode. Further increase of h brings the two damped modes associated with another branch of the cotangent closer to the real axis. In Fig. 3.11(c), the two poles hit the real axis on the unphysical sheet. As h increases, one pole moves to the higher frequency

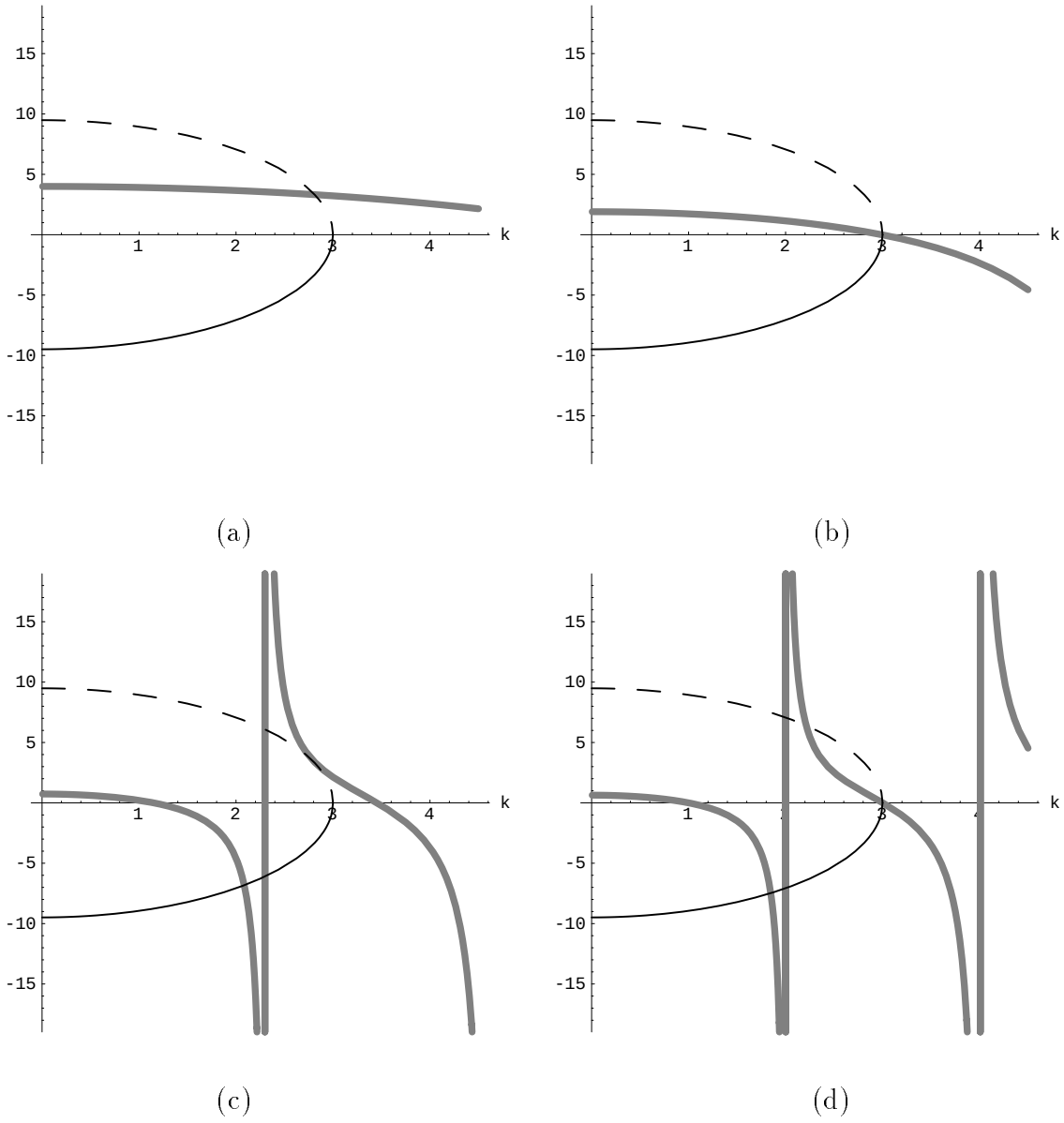

Figure 3.11: A graphical display of solutions to Eq. 3.50. The thick gray solid lines represent the left hand side of the Eq. 3.50, the solid thin lines represent the right hand side of the Eq. 3.50. The dashed line is the negative of the solid thin curve.

while other moves to the lower. At $h = \frac{3\pi}{\sqrt{\mu\epsilon-1}}$, the higher frequency pole moves to the physical sheet (Fig. 3.11(d)).

3.3.2 Wakefield

Since we are most interested in the so-called dipole wakefield, namely the deflecting force in the same direction as the source particle offset, and proportional to the offset, we can simplify the expression in Eq. 3.45 further. Because the offset is in x direction, we need to calculate H_y field at the center. From the *Gauss's Law* on magnetic induction

$$\nabla \cdot \vec{B} = \mu(\frac{\partial H_x}{\partial x} + \frac{\partial H_y}{\partial y} + \frac{\partial H_z}{\partial z}) = 0,$$

we obtain

$$\frac{\partial^2}{\partial x \partial y} H_x + \frac{\partial^2}{\partial y^2} H_y = 0 \tag{3.51}$$

because we choose the dimension b in the z direction very small, the field is independent of z. in another word, we only consider the $n = 0$ terms in the Eq. 3.45.

Substituting Eq. 3.45 in, we obtain

$$\begin{aligned} H_y &= \sum_m \int \frac{i\alpha_{m0}}{2} \{-\frac{\sin(k_x x)}{k_x} \cos(k_x dx) \frac{D_2}{D_1} - \cos(k_x x) k_x \sin(k_x dx) \frac{D_1}{D_2}\} \\ &\quad e^{-i\omega t} d\omega \frac{\frac{\partial}{\partial y} f_{m0}(y,z)}{-(\frac{m\pi}{a})^2}. \end{aligned} \tag{3.52}$$

We have used the fact $\frac{\partial^2}{\partial y^2}(\frac{\partial}{\partial y} f_{m0}(y,z)) = -(\frac{m\pi}{a})^2 (\frac{\partial}{\partial y} f_{m0}(y,z))$. Taking $x = y = 0$ and dx infinitesimally small, the wake force F_x is

$$\frac{F_x}{qdx} = \frac{v}{c}\frac{B_y}{dx} = \frac{v\mu}{c} \sum_m \int \frac{i\alpha_{m0}}{2} k_x^2 \frac{D_1}{D_2} e^{-i\omega t} \frac{\partial}{\partial y} \frac{f_{m0}(y=0,z)}{(\frac{m\pi}{a})^2} \tag{3.53}$$

The wake function $W_\perp$, defined as the force produced by unit charge offsets unit distance on unit test charge, becomes

$$\begin{aligned} W_\perp &= \frac{\mu}{ab} \sum_m (\sin\frac{m\pi}{2})^2 \int \frac{ik_x^2}{\omega} (e^{i\frac{b}{2v}\omega} - e^{-i\frac{b}{2v}\omega}) e^{-i\omega t} \frac{D_1}{D_2} d\omega \\ &= \frac{-\mu}{ab} \sum_{n=0}^{m=2n+1} \int \frac{2k_x^2 \sin\frac{b}{2v}\omega}{\omega} e^{-i\omega t} \frac{D_1}{D_2} d\omega \end{aligned} \tag{3.54}$$

In the relativistic limit.

As we have discussed before, the integral in Eq. 3.54 is taken along the entire real axis of the physical sheet on the positive imaginary side of the branch cut with infinitesimal detour above them.

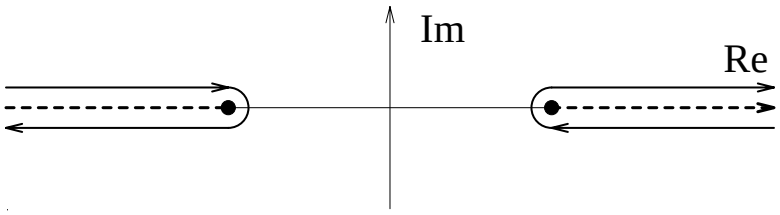

Figure 3.12: Contour path to calculate $W_\perp$.

After the particle leaves the cavity ($t > \frac{b}{2v}$), the line integral from $+\infty$ to $-\infty$ slightly below real axis vanishes because it can be closed in the lower half plane. We add it to the integration path of Eq. 3.54 and shrink it to the form shown in Fig. 3.12. This is nothing more than decomposing the field in terms of the continuum eigenmodes, and accordingly we refer to it as the continuum representation. Usually, there are poles of D_2 on the real axis, and they will contribute to the line integral because the path sweeps through them as we shrink the contour. The non-decaying nature of the trapped modes make them undesirable in the design of accelerator cavities. We could, in our model, make sure no trapped modes exist by making $h < \frac{\pi}{\sqrt{\mu\epsilon-1}}$. In reality, the cavity geometry has to be carefully designed to avoid any trapped dipole (antisymmetric) modes. It is commonly done with the help of an electromagnetic simulation code. Assuming it has been done, therefore, we did not include poles on the real axis in Fig. 3.12.

A representation which is more convenient for analyzing the wakefield is obtained by moving the branch cut integral downwards to $\pm\omega_c - i\infty$, as shown in Fig. 3.13.

Here the upper half plane together with the lower half plane region between the two indicated branch cuts is a part of the physical sheet, while the remainder of the lower half plane is on the unphysical sheet. In shrinking the contour integral to

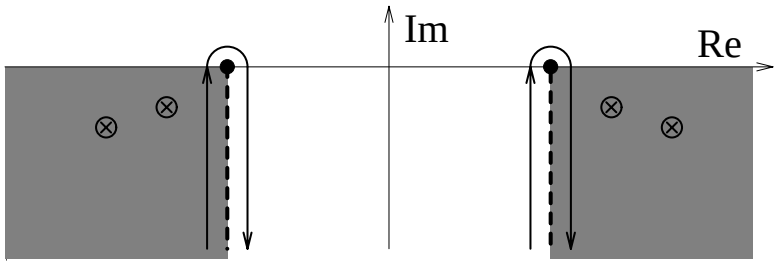

Figure 3.13: Contour path to exhibit the damped and persistent components of $W_\perp$.

the two discontinuity integrals along the branch cuts, we must pass through the poles which have been exposed on the unphysical sheet, and we must retain a residue from each of them. Thus we have expressed $W_\perp$ as an expansion in terms of the discrete exponentially damped cavity modes with $\Re(\omega_j) > \omega_c$ plus a contribution from the branch cut integrals. It is this latter contribution which provides the persistent wake (see, Sec. 3.3.3). We refer Eq. 3.55

$$W_\perp \sim (\int_\cap + \int_\cap)\beta(\omega)e^{-i\omega t} + \sum_j \gamma_j e^{-i\omega_j t} \tag{3.55}$$

as the damped modes representation. Here the $\cap$ denotes the two branch cut integrals, and ω_js are the poles on the unphysical sheet with real part greater than ω_c.

The pole contributions are normally interpreted as damped modes, but they do have one difficulty when one considers the time-distance propagation. The time t and coordinate x dependence of an exponentially damped mode with, for example, $\omega_r > 0$

$$H \sim e^{-i(\omega_r + i\omega_i)t} e^{i(k_r + ik_i)x} \qquad (t > 0, x > 0, \text{ and } \frac{x}{t} < 1)$$

has $k_r + ik_i = \sqrt{(\omega_r + i\omega_i)^2 - 1}$, (for simplification, frequency is normalized to cutoff, and speed of light is 1) with

$$k_r = \sqrt{\frac{{\omega_r}^2 - {\omega_i}^2 - 1 + \sqrt{({\omega_r}^2 - {\omega_i}^2 - 1)^2 + 4{\omega_r}^2{\omega_i}^2}}{2}}, \tag{3.56}$$

$$k_i = -\sqrt{\frac{-({\omega_r}^2 - {\omega_i}^2 - 1) + \sqrt{({\omega_r}^2 - {\omega_i}^2 - 1)^2 + 4{\omega_r}^2{\omega_i}^2}}{2}}. \tag{3.57}$$

The sign of k_r follows from analytic continuation of k_x from $\omega_i = 0$ into the unphysical sheet with $\omega_i < 0$. The negative sign of k_i is seen most simply from the relation $k_i = \frac{\omega_r}{k_r}\omega_i$. Interpreting $\frac{k_r}{\omega_r}$ (always less than one) as the group velocity of the decaying mode as it propagates down the waveguide, we see that the exponential growth in x at fixed t just reflects the fact that the field was emitted at an earlier time. Indeed if we take $x = v_g t = \frac{k_r}{\omega_r}t$, then $\omega_i t - k_i x$ vanishes, corresponding to the fact that the mode propagates at v_g without decay after it is emitted into the waveguide. The anomaly occurs for $1 > \frac{x}{t} > v_g$. Here the exponential factor increases without limit as t and x simultaneously increase. This unphysical exponential growth can only be cancelled by the infinite pole summation and/or the branch cut integral. We conclude that it is better to use the continuum representation for this region.

However, we are interested in the field at the origin, where this difficulty does not occur. So we will use Eq. 3.55 to study the wakefield.

3.3.3 Persistent Wake

We define the persistent wake function W_p as the contribution from the branch cut discontinuity integrals, and to simplify the discussion we redefine t as $\omega_c t$ and ω as ω/ω_c. The cut discontinuity can then be written as $\sqrt{\omega^2-1}F(\omega)$ where F is analytic in the neighborhood of the branch point. Making use of partial integration, we obtain the large t asymptotic behavior as follows:

$$\begin{aligned} W_p(t) &= \int_1^{1-i\infty} \sqrt{\omega^2-1}F(\omega)e^{-i\omega t}d\omega + c.c. \\ &= \frac{1}{it}\int_1^{1-i\infty} e^{-i\omega t}d\omega\frac{d}{d\omega}\sqrt{\omega^2-1}F(\omega)d\omega + c.c. \\ &= \frac{1}{it}\int_1^{1-i\infty} e^{-i\omega t}\frac{F(1)}{\sqrt{\omega^2-1}}d\omega + \\ &\quad \frac{1}{it}\int_1^{1-i\infty} e^{-i\omega t}\sqrt{\omega^2-1}G(\omega)d\omega + c.c.. \end{aligned} \tag{3.58}$$

Here G, which has the same analyticity properties as F, is given by

$$G(\omega) = \frac{F(\omega)\omega - F(1)}{\omega^2-1} + \frac{dF}{d\omega}. \tag{3.59}$$

The dominant asymptotic behavior comes from the first term. Carrying out the integral we find

$$W_p(t) = -\frac{\pi}{2t} H_0^{(2)}(t) F(1) + O(t^{-5/2}) + c.c.. \tag{3.60}$$

which decays as $t^{-3/2}$. Here $H_0^{(2)}$ is the zeroth order Hankel function of the second kind. Because the second term in Eq. 3.58 is subject to the same manipulations as the first, it falls off as $t^{-5/2}$, and by repeating the process one obtains a sequence terms falling off with increasing powers of $\frac{1}{t}$.

There is another class of integrand, which can be written as $\frac{F(\omega)}{\sqrt{\omega^2-1}}$[8] near the branch point. Our straight waveguide model in Sec. 3.2 has an integrand in this class. See Eq. 3.14. The leading term of the persistent wakefield falls off as $t^{-\frac{1}{2}}$ because the integration by part in Eq. 3.58 is not necessary, which saves one power of t.

In general, if the integrand can be written as $F(\omega)(\omega^2-1)^{n-\frac{1}{2}}$ near the branch point, the persistent wakefield falls off as $t^{-(n+\frac{1}{2})}$ because integration by parts has to be performed n times to bring down nth power of t.

3.3.4 Numerical Test

For a particular choice of parameters, $h = 0.8$, $\mu = 1.25$ and $\epsilon = 10$, the full expression for $W_\perp$ in Eq. 3.54, $m = 1$ term, has been evaluated numerically. We calculate the integration by the contour in Fig. 3.7. A numerical root searcher finds all the complex poles and their respective residues in the lower half complex plane (up to $\pm 330\omega_c$ in the real part) . A few of them has been listed in Table 3.1. Of course, there are their mirror images on the left side of lower half plane, which we did not show.

It is interesting to note that the imaginary part of the poles approaches a constant value. For a physical interpretation, note that at higher and higher frequency, the group velocity approaches the speed of light. The rate of energy leaking out of the dielectric cavity, which is proportional to the group velocity, is thus constant. As a result, the imaginary part of ω_i, signifying the decay rate, approaches a

[8] $e^{i\omega t}$ is taken out.

Mode number	Pole Location (In unit of ω_c)	Asymptotic value
1	(1.09888934698, -0.122566829057)	1.110720735 - 0.2612752287 I
2	(3.34227453238, -0.24855915074)	3.332162204 - 0.2612752287 I
3	(5.56038962312, -0.256685988028)	5.553603673 - 0.2612752287 I
4	(7.78003711983, -0.258931266412)	7.775045142 - 0.2612752287 I
5	(10.000416003, -0.259856580572)	9.996486611 - 0.2612752287 I
6	(12.2211624663, -0.260325308928)	12.21792808 - 0.2612752287 I
7	(14.4421158112, -0.260595004928)	14.43936955 - 0.2612752287 I
8	(16.6631962693, -0.260764255552)	16.66081102 - 0.2612752287 I
9	(18.8843601641, -0.260877386255)	18.88225249 - 0.2612752287 I

Table 3.1: Location of the poles on the unphysical sheet.

constant.

Mathematically, we take the expression of D_2 in Eq. 3.32, and write the pole as $k_x \cos(k_x \frac{h}{2}) = i l_x \mu \sin(k_x \frac{h}{2})$, i.e.

$$\frac{e^{ik_x\frac{h}{2}} + e^{-ik_x\frac{h}{2}}}{e^{ik_x\frac{h}{2}} - e^{-ik_x\frac{h}{2}}} = \frac{\mu\sqrt{\omega^2 - 1}}{\sqrt{\mu\epsilon\omega^2 - 1}} \tag{3.61}$$

where we have taken $\frac{\omega_c}{c}$ as unity. Taking the limit as ω approaches ∞, we obtain

$$\frac{e^{i\sqrt{\mu\epsilon}\omega h} + 1}{e^{i\sqrt{\mu\epsilon}\omega h} - 1} = \sqrt{\frac{\mu}{\epsilon}}. \tag{3.62}$$

Solving for ω, we have

$$\omega = \frac{1}{\sqrt{\mu\epsilon}h}(2n\pi - i\log(\frac{\sqrt{\frac{\mu}{\epsilon}} + 1}{\sqrt{\frac{\mu}{\epsilon}} - 1})). \tag{3.63}$$

In our case, with $\mu = 1.25$, $\epsilon = 10$, and $h = 0.8$, we find

$$\omega = 1.110720735 + 2.221441469n - 0.2612752287i \tag{3.64}$$

It can be seen from Table 3.1 that the asymptotic value is highly accurate even down to the second pole.

We select the parameters so that no trapped modes exist. It is shown graphically in Fig. 3.14

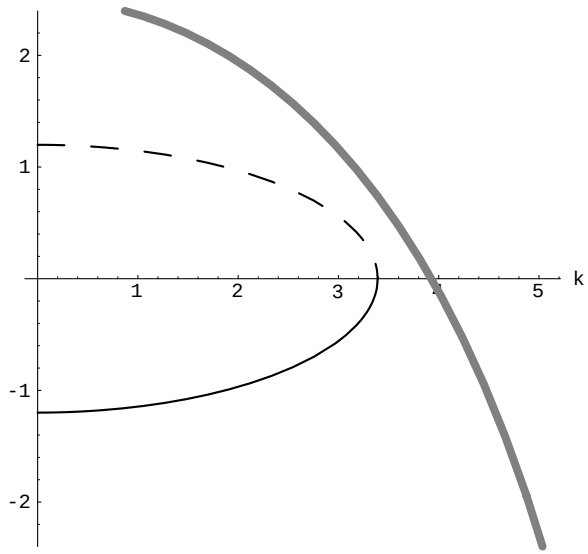

Figure 3.14: A graphical display of the trapped dipole mode solution.

Since there is no intersection between the thick gray curve with the dashed line, no real poles exist on the unphysical sheet either. Our branch cut integral then does not encounter any singularities; no particular care was needed to perform the integration.

The resulting wakefield is shown in Fig. 3.15. Highly damped successive reflections from the interfaces appear at early time. Careful scrutiny reveals that the field oscillates at about $1.12\omega_c$ in early time, which is in between the least damped first mode and the rest almost uniformly damped modes. At long time, however, it is not an exponentially decaying tail.

We also evaluate the asymptotic limit from Eq. 3.60, where, we essentially expand the integrand in Eq. 3.54 in terms of l_x. The linear coefficient of the l_x term is the $F(\omega)$ in Eq. 3.58, which gives the coefficient of $t^{-\frac{3}{2}}e^{-i\omega_c t}$.

The long time tail oscillates at ω_c as shown in Fig. 3.16. The asymptotic limit takes over quite rapidly.

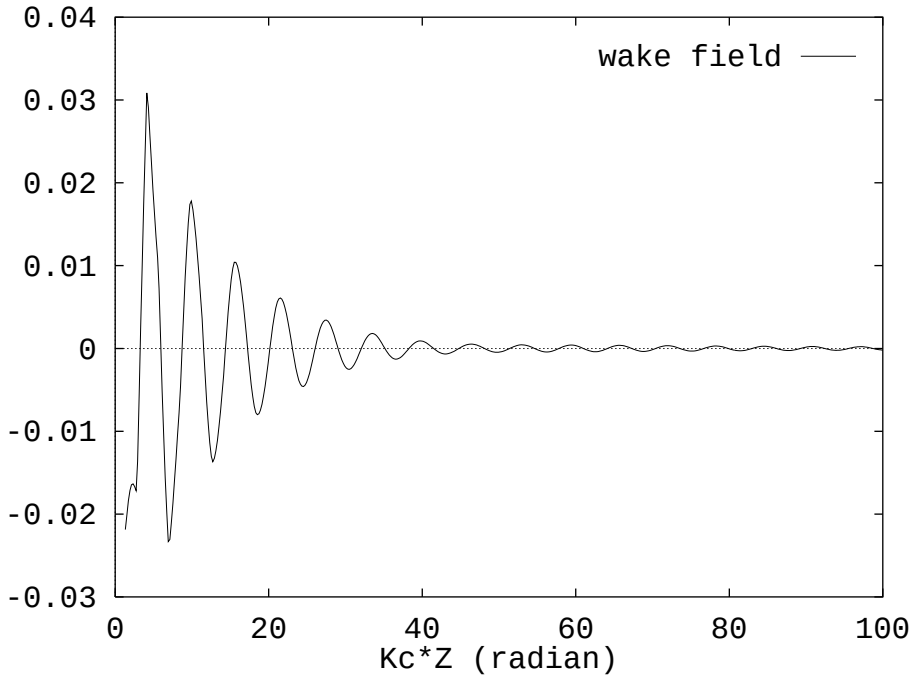

Figure 3.15: Transverse wakefield of the dielectric waveguide model.

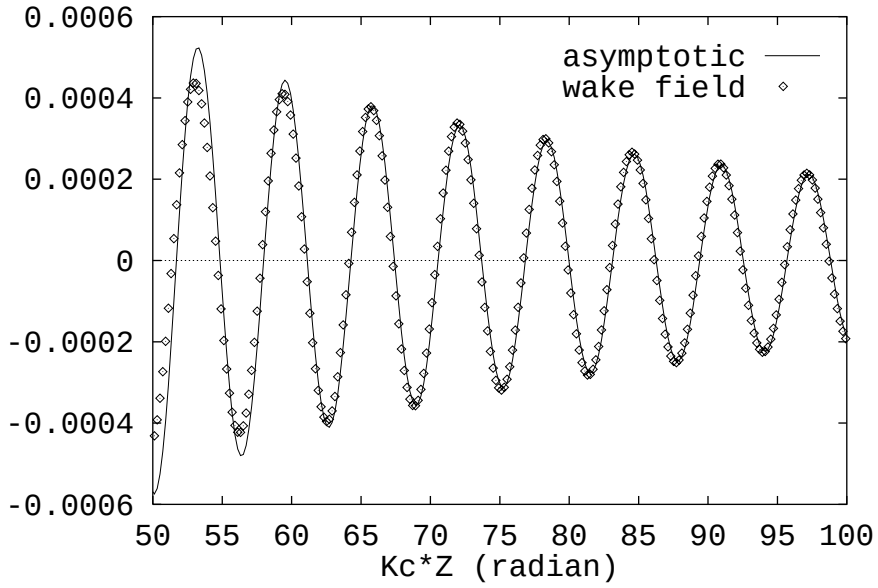

Figure 3.16: Asymptotic behavior of the transverse wakefield.

3.4 Conclusion

We have shown how the persistent wakefield arises from the waveguide cut-off effect, and its connection to the analytical structure of the complex plane. We have also demonstrated that it decays like $t^{-(n+\frac{1}{2})}$, in particular, $t^{-\frac{1}{2}}$ for the straight waveguide model, $t^{-\frac{3}{2}}$ for our dielectric model. Another familiar example of the persistent wakefield is the resistive wall wakefield, which also decays as $t^{-(n+\frac{1}{2})}$. The resistive wall wakefield does not oscillate since the dispersion(the relationship of the wave vector with frequency) in the metal is $k \propto \sqrt{\omega}$.

Because the persistent wakefield does not involve resonance, its magnitude is believed to be small compared to a damped resonant mode. Because of its persistent nature, however we considered it to be necessary to quantify its strength for more realistic structures. We develop various ways of accomplishing this in the next three chapters.

Chapter 4

Persistent Wakefield Amplitude and MAFIA Simulations

Since most of the geometries we are interested in as accelerator cavities can only be simulated on computers, it would be useful to have a procedure in the code to calculate the persistent wakefield. Most simulation codes, in particular MAFIA, do have a wakefield calculation capability. In particular, there is provision to carry out time domain simulation of the fields excited by a beam. It would be most straightforward to calculate the beam excited wakefield under outgoing wave boundary conditions on the waveguide ports. Unfortunately, the accuracy provided with the available broad band outgoing wave boundary condition is not sufficient to see the persistent tail of the wakefield, namely, the outgoing wave conditions at the boundary matched poorly near the waveguide cutoff frequency which is the source of persistent wake. We have performed a few cases where the persistent tail at long time is completely washed out by the errors.[1]

We have chosen to limit this part of the study to heavily damped cavities. We use a very long waveguide, long enough so that, in the time range of interest, the reflected field has not yet returned to the cavity. We can then proceed with

[1] While this work is in progress, some improvement in MAFIA has made it possible to approach the matched load condition by placing lossy dielectric load at the waveguide end. But we have not tested it.

time domain studies without concern for the terminating boundary conditions on the waveguides. (The "electric" boundary condition was actually used.) The waveguide lengths used varied from 26 cm to 60 cm, which allows us to study time intervals somewhat larger than that proposed for successive NLC bunches. The excitation is provided by a $\sigma_z = 2.7mm$ Gaussian beam slightly displaced from the cavity center in the horizontal direction. The time domain simulation requires a finite beam length (σ_z). The length chosen suppresses the contribution of high frequency cavity modes and waveguide cutoffs, which improves numerical accuracy. There is some discussion of results with smaller length in the next chapter.

In all of the structures studied below we specify a very small cavity height (the dimension in the beam direction, which we always refer to as z). The effect of the very high frequency cavity and waveguide modes which are z dependent is completely suppressed by the specified beam length, so that the fields excited may be thought of as two dimensional.

4.1 Simulation

We first studied the cavity formed by two identical waveguides crossing at right angles as shown in Fig. 4.1.

In order to damp the dipole wakefield of both polarizations, at least three waveguides must be used. To simplify modeling, we choose four. By taking symmetry into account, only a quarter of it with proper boundary conditions needs to be studied. See Fig. 4.1(b). Note that with the boundary conditions selected only one of the two dipole mode polarizations can appear. Furthermore, only odd indexed TE modes can appear in the x-directed waveguide and even indexed TE modes in the y-directed waveguide.

The dimension of the configuration, i.e. the width of the waveguide, is chosen such that its fundamental mode has a frequency of 11.424 GHz, as proposed for the X-band NLC, so that we could compare our wakefield with that from other

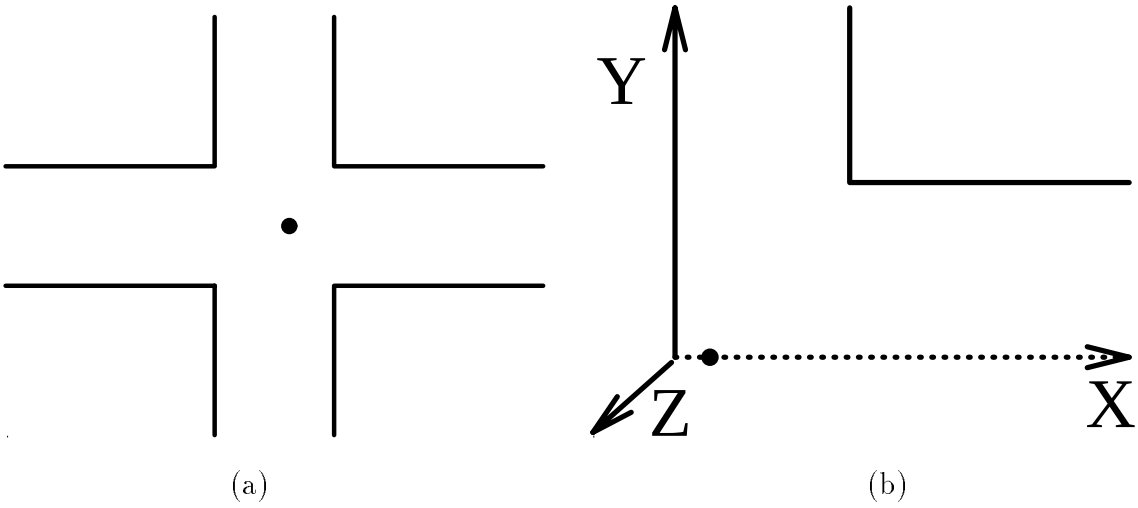

Figure 4.1: Crossed waveguides. The slightly off center dot is the position of beam passage. The (b) figure is the upper right quarter of (a) with electric boundary on the Y axis and magnetic boundary on the X axis.

means of wakefield suppression. The required dimension is calculated in the post processing step by scaling. To scale to the right frequency, all lengths are multiplied by $\alpha = \frac{f_0}{11.424GHz}$, where f_0 is the fundamental frequency of the simulated structure. All the field and force quantities are multiplied by α^{-2}. We found that a waveguide half width of 5.39 mm is needed to obtain $f_0 = 11.424$ GHz.

The MAFIA time domain simulated transverse wakefield is displayed in Fig. 4.2(a). It is clearly not exponential. The oscillating period of the wakefield as determined by the spacing of the wakefield zeros is strikingly uniform. It corresponds precisely to the cutoff wavelength of the waveguide. Because the cutoff frequencies of the z independent modes are all in harmonic relation to one another, this uniform spacing of zeros is expected for the persistent wake. In order to determine the decaying trend, the amplitude is calculated by averaging the square of the field over one period of the waveguide cutoff wavelength. A log-log plot of this amplitude as a function of time is displayed in Fig. 4.2(b). Note that time is shown as z (ct) in all the plots. A $t^{-\frac{3}{2}}$ line (shown dashed) is fitted to the curve by visual inspection. As seen from the plot, the persistent wake dominates the wakefield from as early as one wavelength away from the source particle. Due to the extremely heavy damping, we are not able

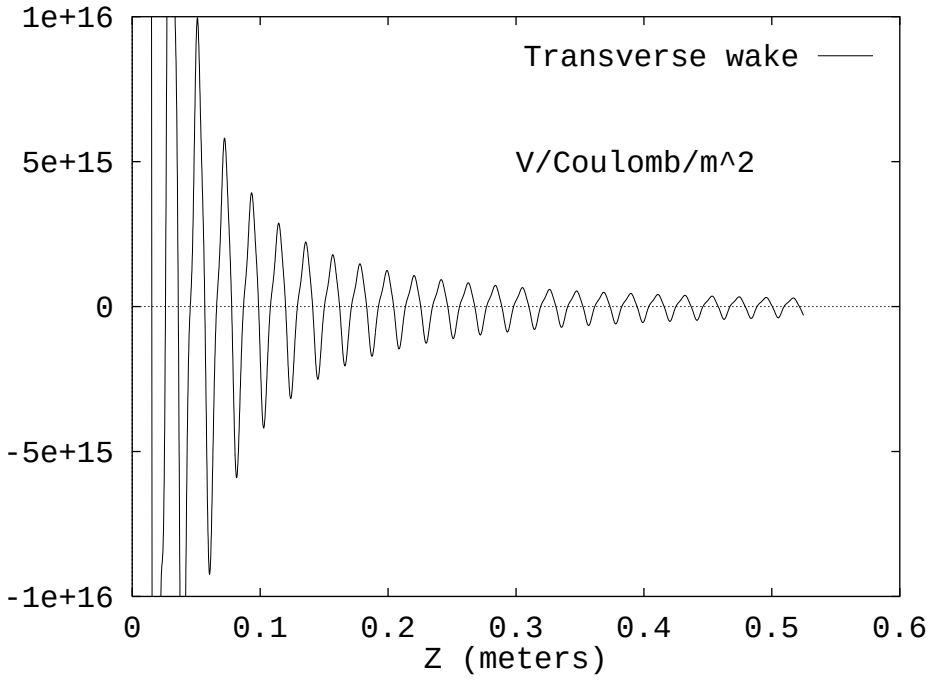

(a)

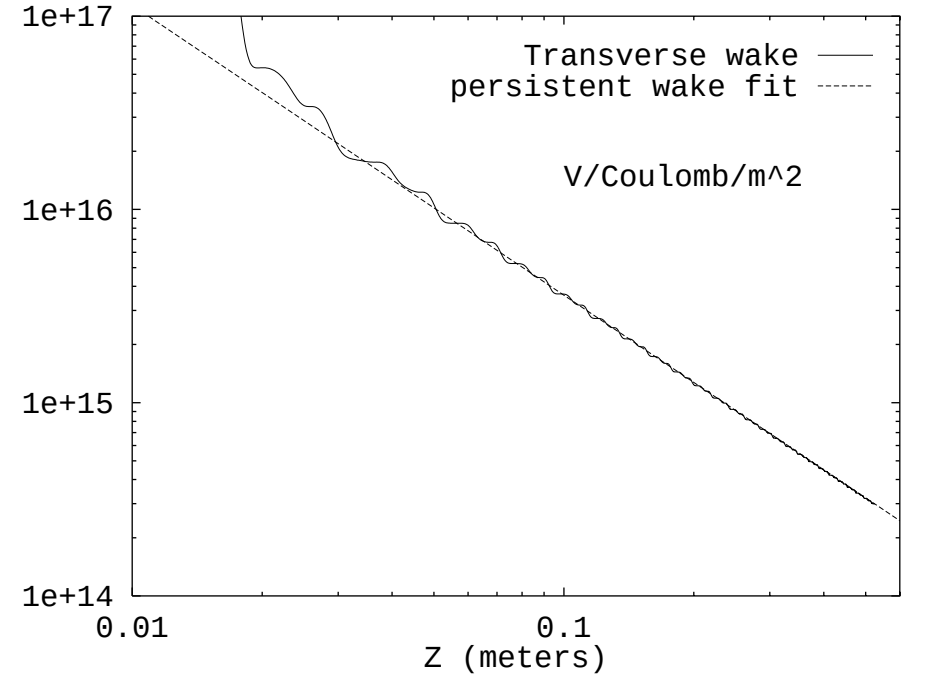

(b)

Figure 4.2: Wakefield of the crossed waveguides.

to resolve any higher order damped modes from the wakefield, nor have we been able to identify any by application of the Kroll-Yu method.

We next studied a set of more realistic models, namely a cylindrical pill-box cavity coupled to the waveguides via inductive irises. The configuration is displayed in Fig. 4.3. Only a quarter of the structure is shown because of the symmetry. The

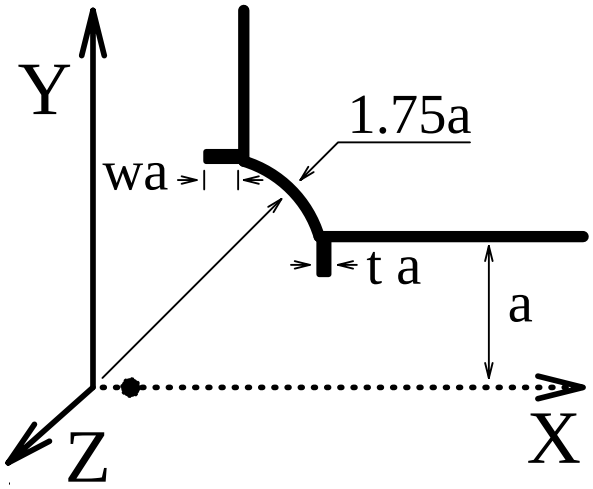

Figure 4.3: Waveguide damped cavity.

waveguide has a half width of a (the total width is $2a$). The radius of the arc is fixed at $1.75a$. We then varied the iris width $w \cdot a$ and thickness $t \cdot a$ to adjust the coupling.

The first case we tested has an iris width of $0.25a$, and thickness of $0.05a$. Through the same scaling procedure, we make the fundamental mode 11.424GHz, which gives the waveguide half width $a = 5.25mm$. The cutoff of the lowest waveguide mode is then $\frac{c}{4a} = 14.27$ GHz. Two damped dipole modes are identified by MAFIA frequency domain calculations. We applied the Kroll-Yu and the Kroll-Lin method as described in Chapter 2 for the first mode and produced consistent results: Resonant frequency = 17.365 GHz and $Q = 3.74$. Because the second dipole mode frequency was found to be above the cutoff of the TE_{20} mode in the y-directed waveguide too, which is $2\frac{c}{4a} = 28.54$ GHz, the cavity is coupled to two propagating channels and the Kroll-Kim-Yu [17][2] (KKY) method was required. It yields a resonant frequency of

[2]KKY show that with more than one channel propagating, the determinant of the S-matrix takes the role of the reflection coefficient in the Kroll-Yu method. The same pole searching procedure

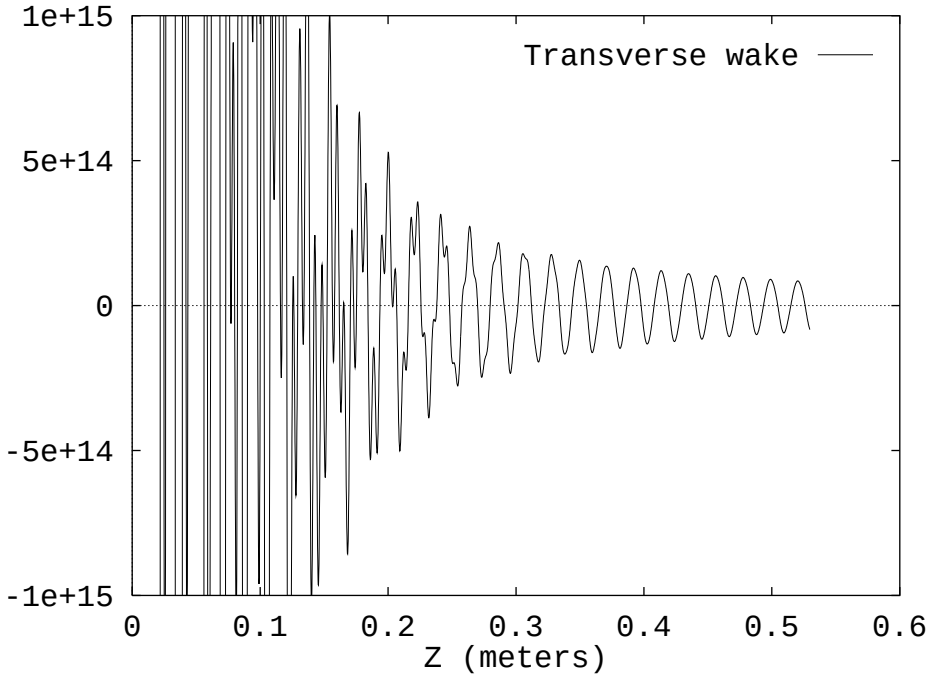

(a)

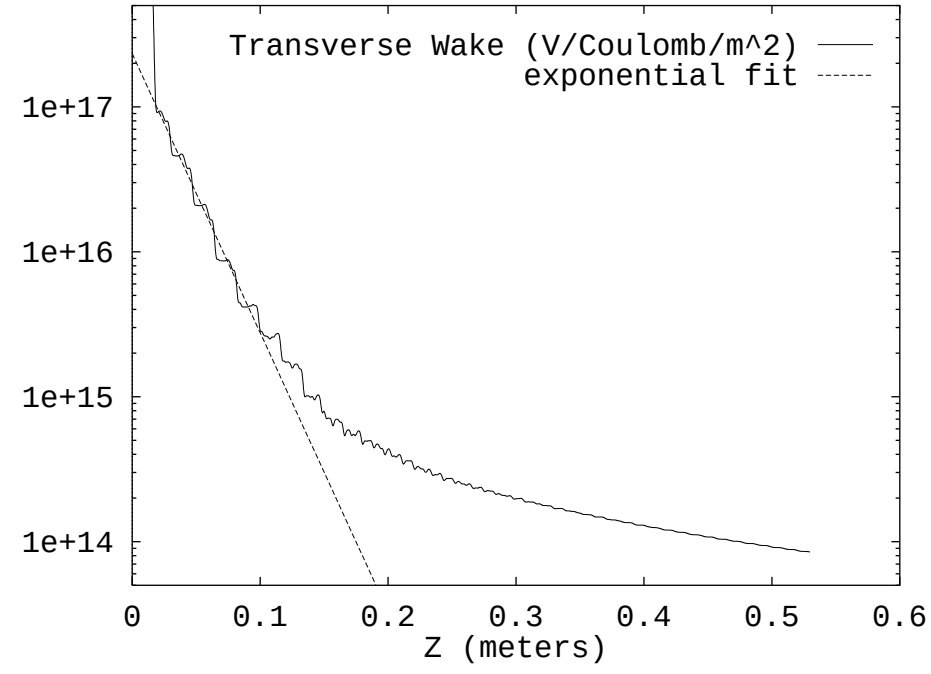

(b)

Figure 4.4: The wakefield of a waveguide damped cavity. The iris has a width $0.25a$ and thickness $0.05a$.

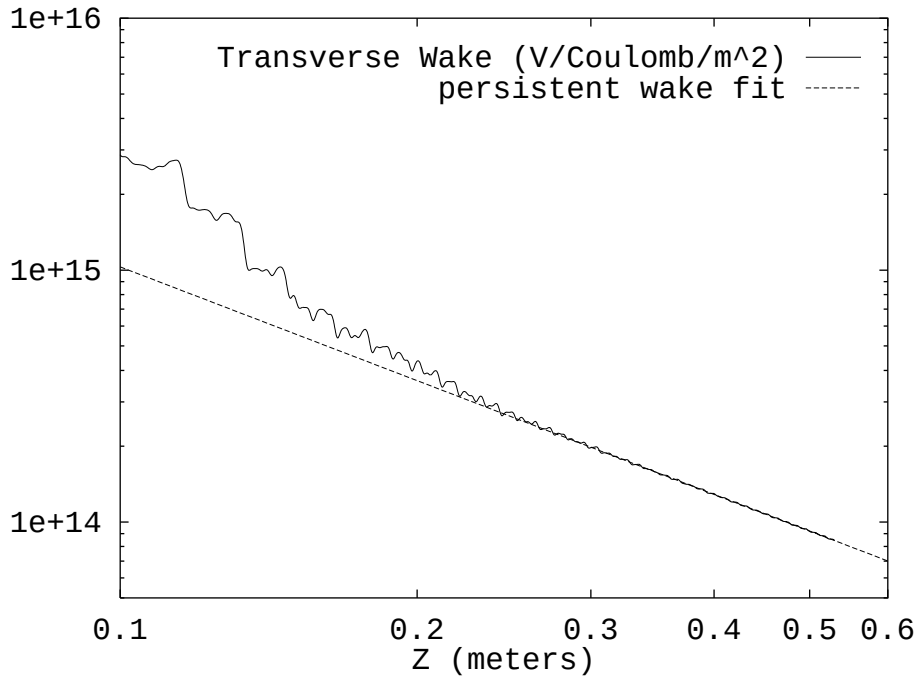

Figure 4.5: The wakefield of a waveguide damped cavity. The iris has a width $0.25a$ and thickness $0.05a$.

34.297 GHz and $Q = 9.0$.

The MAFIA time domain simulation of the transverse wakefield for this case is shown in Fig. 4.4. An early exponentially decaying field is visible (it is not shown in Fig. 4.4(a) because of the scale.) in the wakefield plot. The log plot of the averaged amplitude in Fig. 4.4(b) exhibits perhaps three exponential damping rates. The straight line fit shown by the dashed line determines a damping rate of $44.33m^{-1}$, which is to be compared to the unresolved pair of decay rates of $48.64m^{-1}$ and $39.92m^{-1}$ from the first and second dipole modes determined in the frequency domain calculation earlier. The second slope of $27.6m^{-1}$ in the z interval $0.1 - 0.15$ meters (the straight line fit is not shown.) is associated with a higher frequency mode beyond the range of our frequency domain simulation. Figure 4.5 shows the log-log plot of the same wakefield. The persistent wake is again quite apparent, and the straight line fit shows that, as in the waveguide cross case, it dominates at an early

applies.

stage.

It is very interesting to compare the wakefield of Fig. 4.2(b) and Fig. 4.5 at a typical distance, 42 cm, the inter-bunch distance chosen by the X-band NLC design. The second configuration, despite having less damping, results in a wakefield which is 3.5 times smaller. It can be understood by noticing the role played here by the coupling strength.

With the contour integral in Fig. 3.13, and the results of Eqs. 3.58 and 3.60, Eq. 3.55 can be written as sums of the damped modes and persistent wake modes as in the following:

$$W_\perp(t) = \sum_i \alpha_i e^{-\frac{\omega_i t}{2Q_i}} \sin(\omega_i t) + \sum_j \gamma_j t^{-\frac{3}{2}} \sin(\omega_j^c t + \phi_j), \tag{4.1}$$

where index i sums over all damped modes, which are shown as complex poles on the unphysical sheet. The index j runs over all waveguide modes. The damped mode amplitudes α's are primarily determined by the cavity geometry, particularly, the size[3], while the Q's and γ's are directly related to the cavity-waveguide coupling. The weaker the coupling, the higher the Q's, but the γ's vary in the opposite way. The persistent wake is associated with an excitation in the waveguide. Its excitation by a beam passing through the cavity is reduced by weakening the cavity-waveguide coupling. The competition between the Q's and γ's will lead to an optimum coupling strength, which gives a minimum wakefield. Of course, the minimum value depends on the distance we are interested in. Nevertheless, it is clear from the above comparison, that *extreme* damping can do more harm than good.

To further investigate this issue, we proceed to increase the iris thickness in order to further reduce the coupling. The transverse wakefield shown in Fig. 4.6 is obtained by increasing the iris width to $0.25a$, other parameters of the cavity-waveguide system being kept unchanged. (It is understood that we always rescale a to keep the frequency of the accelerating mode at 11.424 GHz.) We see a factor of 2.2 reduction of the persistent amplitude in Fig. 4.6(b) compared with that of Fig. 4.4(b).

[3]Especially for the higher Q resonances. In very low Q cases, the amplitudes depend moderately on the coupling.

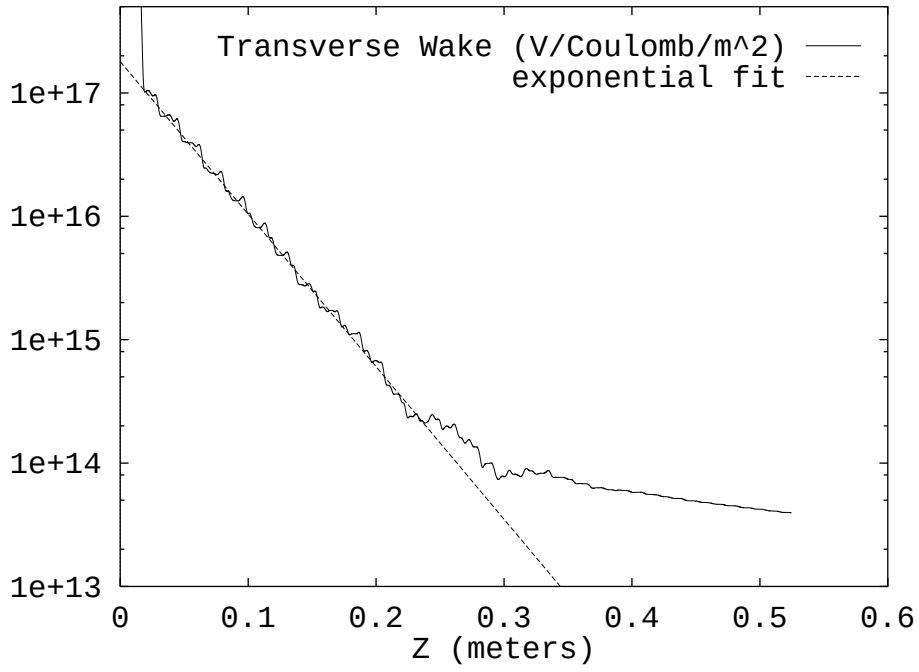

(a)

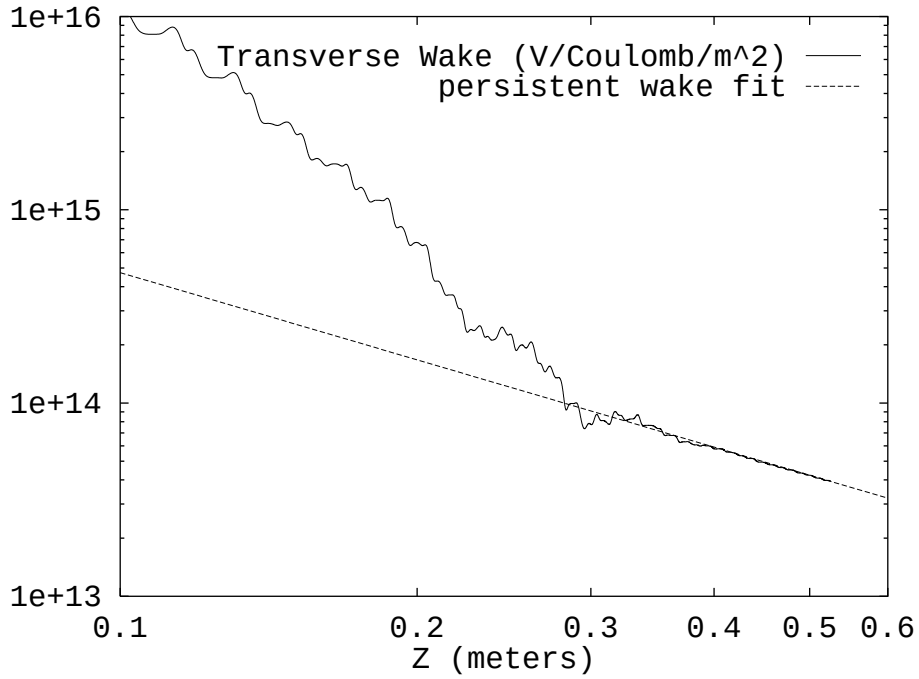

(b)

Figure 4.6: The wakefield of a waveguide damped cavity. The iris has a width $0.25a$ and thickness $0.25a$.

Since the persistent wake still dominates the wakefield after 0.3 meters, the overall wakefield at 42 cm is reduced by the factor of 2.2 as well.

The straight line fit in Fig. 4.6(a) determines a damping rate of $28.48m^{-1}$. By careful examination of the location of the zero crossings in the wakefield data, we are able to determine the resonant frequency of the dipole mode[4] at 17.445GHz. Based on the damping rate and resonant frequency, we determine the Q of the mode to be 6.42. This represents a 72% increase with respect to the result 3.74 found for the previous case. On the other hand, The amplitude of the damped mode, as indicated by the intersection of the dashed line with vertical axis in Fig. 4.4(a) and Fig. 4.6(a), changed only moderately from 2.33×10^{17} to 1.817×10^{17}, a 22% change. This result supports our argument on page 64 .

The results obtained from a third simulation with even larger iris width ($0.35a$) is displayed in Fig. 4.7. The damping rate shown in Fig. 4.7(a) is $16.88m^{-1}$, and the resonance frequency is 18.14GHz based on the same zero crossings location method used for the previous case. The dipole mode thus has a Q of 11.3. The persistent wake does not dominate the wakefield until 0.8 meters behind the source particle. As a consequence, the wakefield amplitude at 42 cm becomes larger than that in Fig. 4.6 even though the persistent wakefield amplitude has decreased. Therefore, we know that the optimum coupling has a Q in between 6.42 and 11.3.

4.2 Conclusion

We have shown a way to extract the persistent wakefield from MAFIA time domain simulations. Through the examples, we observed the dependence of wakefield amplitude on the coupling strength of the cavity-waveguide system. The results imply the existence of an optimum damping to achieve a minimum wakefield at a specified trailing distance *i.e. time interval*.

[4]We have assumed only one damped mode dominates at the early time. Even though our frequency domain calculation of the previous case shows that there is a higher order dipole mode at around 34 GHz, our assumption is reasonably well justified because of the weak excitation at higher frequency due to finite bunch length.

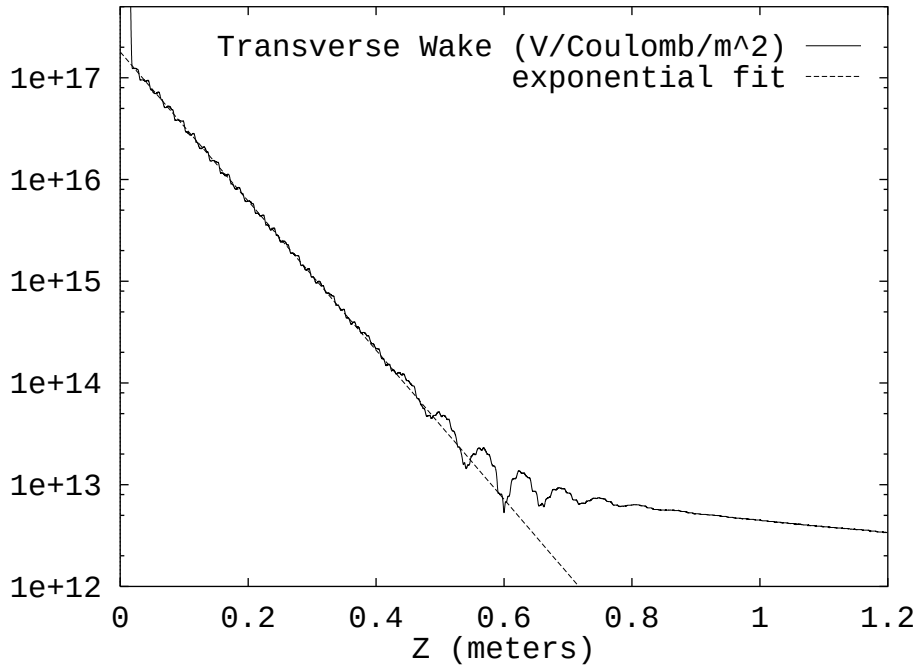

(a)

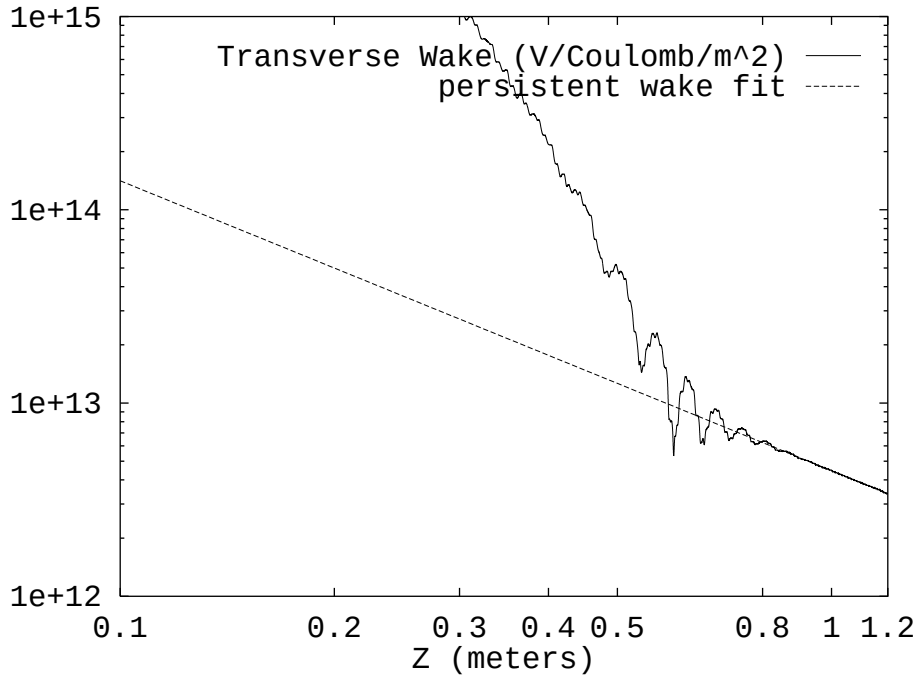

(b)

Figure 4.7: The wakefield of a waveguide damped cavity. The iris has a width $0.35a$ and thickness $0.25a$.

Notice from the above simulation that for a moderate value of Q, we have to calculate the wakefield to a very long distance in order to see the persistent tail. Our current method, which requires that we extend the waveguide length proportionally, becomes untenable, partly because of the finite difference meshing: the total mesh points goes as square of the length in 2D, not to mention cubic growth in 3D. All the mesh points in the space between the waveguides are totally wasted. We are thus motivated to explore other methods of determining the persistent wakefield. One promising method is mode matching, which will be described in the next chapter.

Chapter 5

Mode Matching Method

The previous chapter has demonstrated that the persistent wakefield decays as $t^{-3/2}$ in a waveguide damped cavity and oscillates at the waveguide cutoff frequency. But the amplitude of the wakefield is far from easy to determine. In this chapter, we present a new mode matching method, which involves concurrent mode matching on two or more orthogonal surfaces, to calculate the persistent wakefield. Furthermore, combining this technique with concatenation of generalized S-matrices, we illustrate that the electromagnetic field for many regular shapes can be determined.

The technique of mode matching on orthogonal surfaces has potentially useful applications on a variety of passive microwave circuits as well. We discuss a ninety degree bend problem as an example.

We also derive, as a consequence of the complex form of the Poynting vector Theorem, a weakened but non-trivial form of the unitary condition which applies to a general S-matrix involving non-propagating modes.

5.1 Mode Matching

Mode matching is a semi-analytical way to solve electromagnetic fields in a structure. It involves expanding the fields in two or more uniform regions in their respective eigenmodes and matching the fields on the common surface. We have

already used this method in Chapter 3, where the waveguide eigenmodes are the same on both sides of the common surface and not cross-coupled. As a result, the equations for the unknown amplitudes are easy to solve. Normally, the transverse electric field $\vec{E}_\perp$ and magnetic field $\vec{H}_\perp$ are matched at the interface, which is equivalent to our treatment on page 33 of matching $\frac{dH_x}{dx}$ and B_x, respectively in the dielectric cavity model.

A slightly non-trivial example of mode matching is to calculate the S-matrix of a waveguide step, where the waveguide changes its cross section at a certain location called the junction or interface. A typical step is illustrated in Fig. 5.1, where

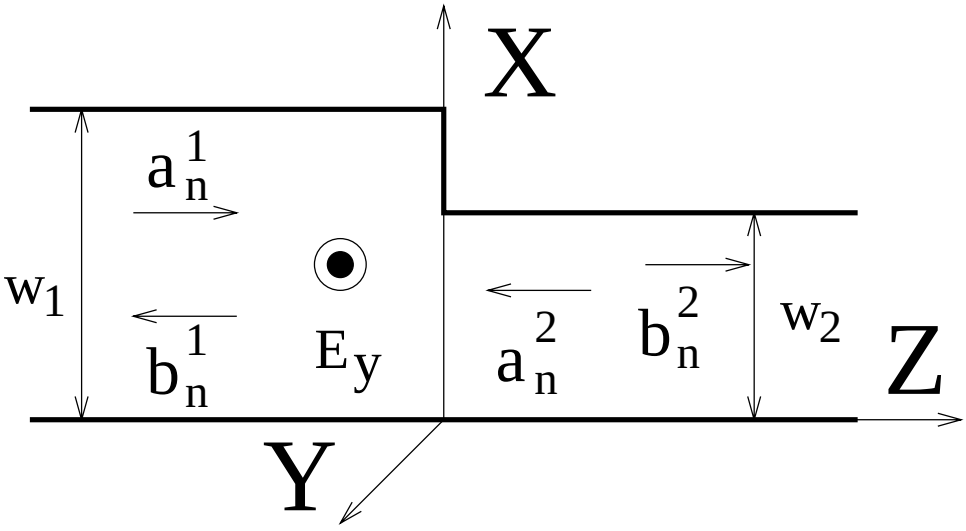

Figure 5.1: A one-step waveguide, where the superscripts 1 and 2 denote the ports, and the subscript n represents the channel.

the y direction is considered to be uniform. To simplify the discussion, the fields are also taken to be uniform in the y direction. Under these assumptions there are waveguide eigenmodes with $E_x = E_z = 0$, and an independent corresponding set with $H_x = H_z = 0$ (See Appendix A.1. Treat the configuration as a waveguide in Y direction.). Take the former case, which may be characterized by TE^{n0} ($n \neq 0$) waves incident with amplitude a_n^1 and a_n^2. We need to determine the reflected amplitudes b_n^1 and b_n^2. Expanding fields on both sides of the interface in their respective

eigenmodes(waveguide modes in Z direction), we obtain

$$\vec{E}^1_\perp = \sum_n (a^1_n e^{ik^1_{zn}z} + b^1_n e^{-ik^1_{zn}z}) e^{-i\omega t} \vec{f}^1_n, \tag{5.1}$$

$$\vec{H}^1_\perp = \sum_n (-\frac{k^1_{zn}}{\omega\mu})(a^1_n e^{ik^1_{zn}z} - b^1_n e^{-ik^1_{zn}z}) e^{-i\omega t} \vec{g}^1_n, \tag{5.2}$$

$$\vec{E}^2_\perp = \sum_m (a^2_m e^{-ik^2_{zm}z} + b^2_m e^{ik^2_{zm}z}) e^{-i\omega t} \vec{f}^2_m, \tag{5.3}$$

$$\vec{H}^2_\perp = \sum_m (\frac{k^2_{zm}}{\omega\mu})(a^2_m e^{ik^2_{zm}z} - b^2_m e^{ik^2_{zm}z}) e^{-i\omega t} \vec{g}^2_m, \tag{5.4}$$

where $k^1_{zn} = \sqrt{(\frac{\omega}{c})^2 - (\frac{n\pi}{w_1})^2}$ and $k^2_{zm} = \sqrt{(\frac{\omega}{c})^2 - (\frac{m\pi}{w_2})^2}$. In deriving the magnetic field, we have used Eq. A.17. The eigenmodes $\vec{f}$'s and $\vec{g}$'s are

$$\vec{f}^1_n = \frac{2}{\sqrt{w_1}} \sin(\frac{n\pi}{w_1}x)\hat{y}, \qquad \vec{g}^1_n = \frac{2}{\sqrt{w_1}} \sin(\frac{n\pi}{w_1}x)\hat{x}, \tag{5.5}$$

$$\vec{f}^2_n = \frac{2}{\sqrt{w_2}} \sin(\frac{n\pi}{w_2}x)\hat{y}, \qquad \vec{g}^2_n = \frac{2}{\sqrt{w_2}} \sin(\frac{n\pi}{w_2}x)\hat{x}, \tag{5.6}$$

where

$$\int_0^{w_p} \vec{f}^p_n \cdot \vec{f}^p_{n'} = \int_0^{w_p} \vec{g}^p_n \cdot \vec{g}^p_{n'} = \delta_{n,n'}, \quad p = 1,2. \;\; n, n' = 1, 2... \tag{5.7}$$

Continuity for the fields ($\vec{E}_\perp$ and $\vec{H}_\perp$) at $z = 0$ produces the following equations:

$$\sum_n (a^1_n + b^1_n)\vec{f}^1_n = \sum_m (a^2_m + b^2_m)\vec{f}^2_m, \tag{5.8}$$

$$\sum_n (a^1_n - b^1_n)k^1_{zn}\vec{g}^1_n = \sum_m -k^2_{zm}(a^2_m - b^2_m)\vec{g}^2_m. \tag{5.9}$$

In order to make use of Eq. 5.7, the mode orthogonality, Eq. 5.8 is multiplied by $\vec{f}^1_{n'}$ and integrated with respect to x from 0 to w_1 and Eq. 5.9 is multiplied by $\vec{g}^2_{m'}$ and integrated with respect to x from 0 to w_2. This yields

$$a^1_{n'} + b^1_{n'} = \sum_{m=1}^{M} (a^2_m + b^2_m)F(m,n') \quad n' = 1, 2, ...N, \tag{5.10}$$

$$\sum_{n=1}^{N} (a^1_n - b^1_n)k^1_{zn}F(m',n) = -k^2_{zm'}(a^2_{m'} - b^2_{m'}) \quad m' = 1, 2, ...M, \tag{5.11}$$

where

$$F(m,n) \equiv \frac{(-1)^{m+1}\frac{m\pi}{w_1}\sin(\frac{n\pi}{w_1}w_2)}{(k^2_{zm})^2 - (k^1_{zn})^2}. \tag{5.12}$$

We truncate the summation to N in the bigger waveguide, M in the smaller guide. There are a total of $M+N$ equations, with N b_n^1 and M b_m^2 as unknowns. Solving the linear equations expresses the b_n^1's and b_m^2's in terms of a_n^1 and a_m^2. This is the so-called scattering matrix. The ratio of $\frac{N}{M}$ is chosen to be $\frac{w_1}{w_2}$ to optimize convergence [24]. With the above choice of the mode number ratio, the spatial resolution of the fields on both side of the interface is the same.

5.1.1 Mode Matching Calculation on a Waveguide Cross

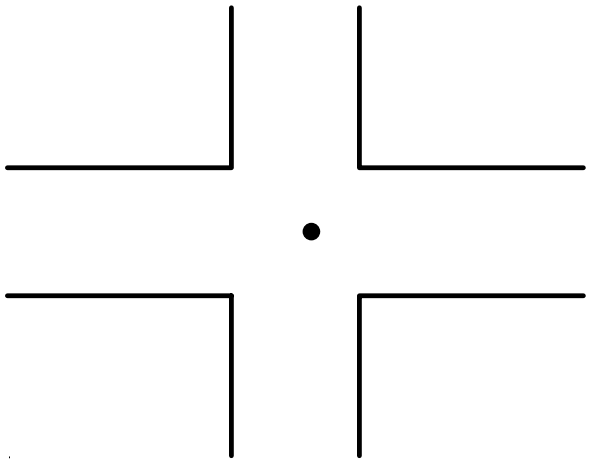

Figure 5.2: Crossed waveguides.

The structure under consideration is a crossed waveguide as in Fig. 5.2. Taking symmetry into account, the waveguide cross can be completely characterized by a 90 degree rectangular waveguide bend shown in Fig. 5.3. We note three appropriate boundary conditions on the $X = 0$ and the $Y = 0$ boundaries: (magnetic, magnetic) for the accelerating mode, (electric, magnetic) for dipole modes, and (electric, electric) for quadrapole modes. Because of the symmetry the (magnetic,electric) case, corresponding to the other dipole mode polarization need not be considered separately.

The method of single surface mode matching does not work here. The matching procedure has to be performed for the two dashed line interfaces at the

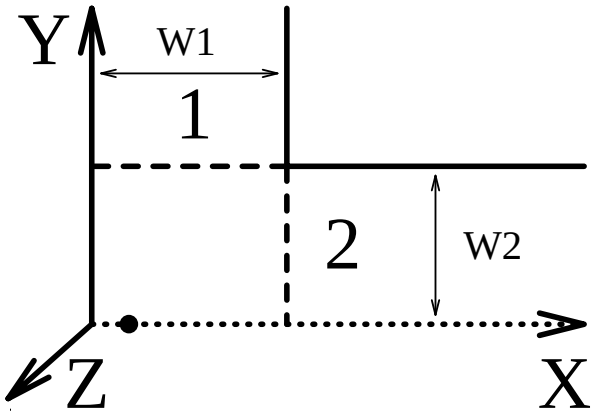

Figure 5.3: A quarter of the crossed waveguide. The short dashed line is the symmetric boundary; the long dashed lines are the waveguide junctions, and the large black dot marks the beam position.

same time. The situation here is distinct from that of two or more serial waveguide junctions in a pipe line, where the matching interfaces are parallel to one another. For the latter case the S-matrix for the assembly can be obtained by concatenating S-matrices separately computed for each junction.

Superposition

Before we introduce the new mode matching method, we digress to consider a simple, more intuitive situation in circuit theory. The box in the Fig. 5.4(a) has two output channels, and we propose to calculate the current flow through the resistors R^1 and R^2 as a function of their values and of the current flows which would occur if the two channels were shorted as shown in Fig. 5.4(b). All circuit elements are linear so that the currents are proportional to the source strength, and the superposition principle holds. In order to calibrate the effects of finite voltage on the R^1 and R^2, we can take a voltage source V^1 to replace the resistor R^1, also remove the source in the box, and calculate the currents I_1^1 and I_1^2 which the voltage V^1 produces (Fig. 5.4(c)). The result is the following:

$$I_1^1 = Y^{11}V^1 \qquad \text{and} \qquad I_1^2 = Y^{21}V^1, \tag{5.13}$$

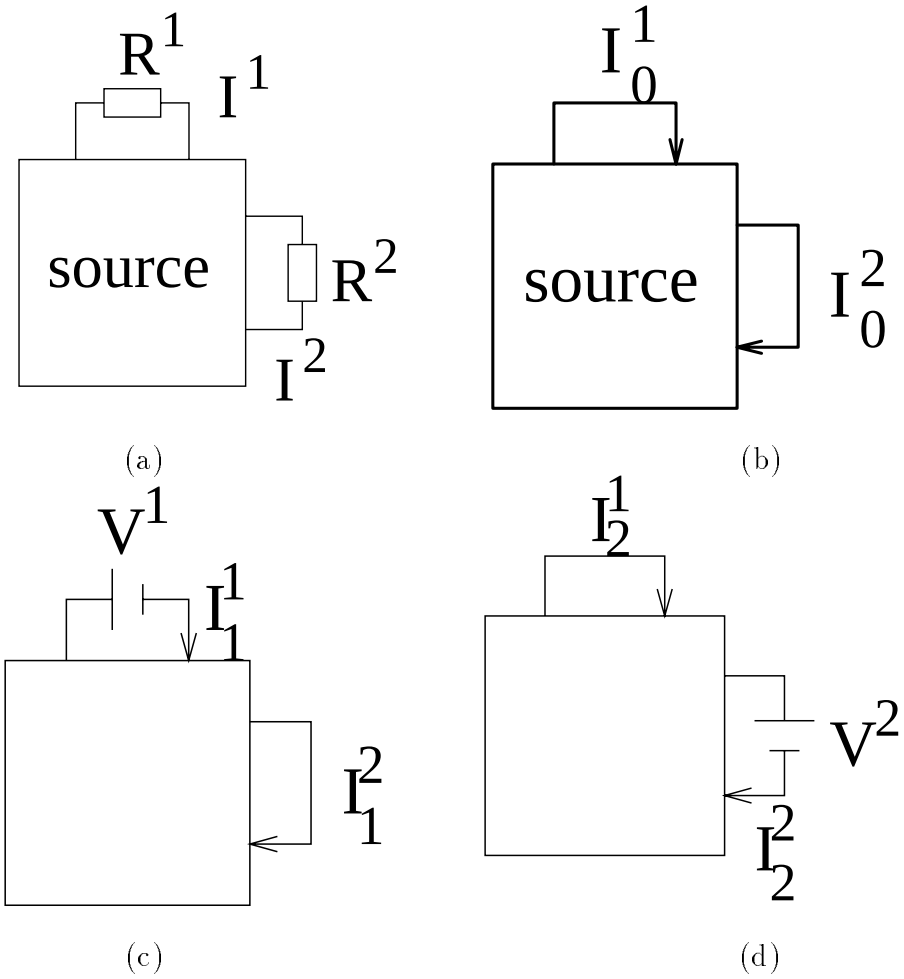

Figure 5.4: A circuit model with two output channels.

where we have used the linearity of the circuit. The proportionality constants Y^{ij} are called admittances. A similar expression can be derived from the configuration of Fig. 5.4(d), which yields

$$I_2^1 = Y^{12}V^2 \qquad \text{and} \qquad I_2^2 = Y^{22}V^2. \tag{5.14}$$

Finally, the solution of Fig. 5.4(a) can be constructed from Fig. 5.4(b), (c), and (d) by taking account of the superposition principle.

$$I^1 = Y^{11}V^1 + Y^{12}V^2 + I_0^1 = \frac{1}{R^1}V^1, \tag{5.15}$$

$$I^2 = Y^{21}V^1 + Y^{22}V^2 + I_0^2 = \frac{1}{R^2}V^2. \tag{5.16}$$

At the last equal sign, we used the *matching* condition at each of the resistors. The linear equations can be easily solved to give the voltage V's at each channel and consequently the currents I^j through the resistors.

Mode Matching on the Cross

To expand the fields at the terminal planes in terms of corresponding waveguide TE or TM eigenmodes, (See Eqs. A.15 and A.17.) an appropriate set of f_n's and g_n's in the cross configuration is

$$\vec{f}_m^1(x,z) = \sqrt{\frac{2}{dzw_1}}\sin(\frac{m\pi}{w_1}x)\hat{z} \quad , \quad \vec{g}_m^1(x,z) = -\sqrt{\frac{2}{dzw_1}}\sin(\frac{m\pi}{w_1}x)\hat{x}, \tag{5.17}$$

$$\vec{f}_n^2(y,z) = \sqrt{\frac{2}{dzw_2}}\cos(\frac{(n+\frac{1}{2})\pi}{w_2}y)\hat{z} \quad , \quad \vec{g}_n^2(y,z) = \sqrt{\frac{2}{dzw_2}}\cos(\frac{(n+\frac{1}{2})\pi}{w_2}y)\hat{y} \tag{5.18}$$

where the superscript denotes the junction. The coordinate directions are as shown in Fig. 5.5, and dz refers to the thickness in the z direction. Because the direction of the field is clear from inspection, we will often use the f's and g's without the vector symbol.

Eq. A.20 gives us a close analogy between the black box circuit in Fig. 5.4 and the microwave junction, where Y_n's are the inverse of the R's. The i_n's and e_n's are the unknowns we need to calculate just like the I's and V's.

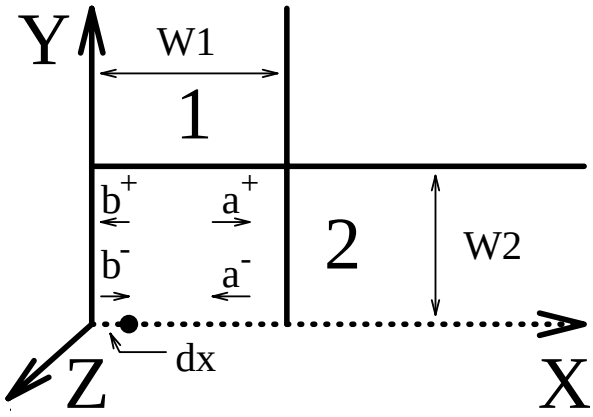

Figure 5.5: Shorted waveguide cross. The long dashed lines are replaced by the solid lines to symbolize the shorting plane and the large black dot is the beam position.

First, in the cross configuration, we are able to calculate the currents on the terminals when the waveguides are shorted at the interface.(See Fig. 5.5 and compare with Fig. 5.4(b).) The z dimension is not shown in the graph, but for the purpose of illustration, we assume $dz \ll w_1$. From Eq. 3.4, the transverse magnetic field H_x satisfies

$$\frac{1}{c^2}\frac{\partial^2}{\partial t^2}H_x - \nabla^2 H_x = \frac{4\pi}{c}\frac{\partial}{\partial y}J_z, \tag{5.19}$$

where $J_z = qc\delta(x-dx)\delta(y)\delta(z-ct)$. We have taken $\mu = \epsilon = 1$. Since the source currents on the interface 2 are the expansion coefficients of the magnetic field generated by J_z on interface 2 in terms of eigenfunctions of waveguide 2, we expand the Fourier components of the field in the $x = (0, w_1)$ region in terms of them.

$$\begin{aligned} H_x^r(\omega) &= \sum_{n=0}(a_n^+(\omega)e^{ik_{xn}x} + a_n^-(\omega)e^{-ik_{xn}x})h_n(y,z) \\ &= \sum_{n=0} a_n^+(\omega)(e^{ik_{xn}x} - e^{2ik_{xn}w_1}e^{-ik_{xn}x})h_n(y,z), \qquad (5.20) \\ H_x^l(\omega) &= \sum_{n=0}(b_n^+(\omega)e^{ik_{xn}x} + b_n^-(\omega)e^{-ik_{xn}x})h_n(y,z) \\ &= \sum_{n=0} b_n^+(\omega)(e^{ik_{xn}x} - e^{-ik_{xn}x})h_n(y,z), \qquad (5.21) \end{aligned}$$

where

$$h_n(y,z) = \sqrt{\frac{2}{w_2 dz}}\sin((n+\frac{1}{2})\pi\frac{y}{w_2}) \qquad \text{and} \qquad k_{xn} = \sqrt{(\frac{\omega}{c})^2 - (\frac{(n+\frac{1}{2})\pi}{w_2})^2}.$$

H_x^r stands for the H_x field to the right of the source particle and H_x^l is that to the left of the source particle. We also used the fact

$$H_x^r(\omega) \mid_{x=w_1} = H_x^l(\omega) \mid_{x=0} = 0$$

in arriving at Eqs. 5.20 and 5.21. We have omitted z dependent modes in the expansion. Because we have specified that dz be very small, z dependent expression produce a very high frequency wakefield which will be of no interest to us. The h_n's satisfy orthogonal conditions:

$$\int h_n(y,z) h_{n'}(y,z) dy dz = \delta_{nn'}. \tag{5.22}$$

The continuity of H_x at $x = dx$ requires

$$a_n^+(e^{ik_{xn}dx} - e^{2ik_{xn}w_1} e^{-ik_{xn}dx}) = b_n^+(e^{ik_{xn}dx} - e^{-ik_{xn}dx}). \tag{5.23}$$

Integrating Eq. 5.19 from dx^- to dx^+ and taking its time Fourier transform yields

$$\frac{\partial}{\partial x} H_x^r(\omega) \mid_{dx} - \frac{\partial}{\partial x} H_x^l(\omega) \mid_{dx} = \frac{q}{c} \delta'(y-\epsilon) e^{i\frac{\omega}{c}z} \tag{5.24}$$

In deriving the above we have replaced $\delta'(y)$ by $(1/2)\delta'(y-\epsilon)$ in order to avoid ambiguity associated with the y integration from zero to w_1 carried out below. The small positive quantity ϵ is set equal to zero after the integration. The factor $1/2$ arises because the assumed symmetry of the configuration implies an equal current source at $y = -\epsilon$. Multiplying by h_n, carrying out the y integration as described above taking account of the orthogonality property, and also integrating over z from $-dz/2$ to $dz/2$, we find

$$\begin{aligned} & ik_{xn}[a_n^+(e^{ik_{xn}dx} + e^{2ik_{xn}w_1} e^{-ik_{xn}dx}) - b_n^+(e^{ik_{xn}dx} + e^{-ik_{xn}dx})] \\ = \quad & -q \frac{2\sin(\omega \frac{dz}{2c})}{\omega} \sqrt{\frac{2}{dz w_2}} \frac{(n+\frac{1}{2})\pi}{w_2} \equiv \alpha. \end{aligned} \tag{5.25}$$

Solving the linear Eqs. 5.23 and 5.25 simultaneously yields the unknown amplitude

$$a_n^+ = -\frac{\alpha}{k_{xn}} \frac{\sin(k_{xn}dx)}{1 - e^{2ik_{xn}w_1}}. \tag{5.26}$$

According to waveguide theory (See Appendix A.1), if we treat the H_x field as the longitudinal field of the waveguide TE mode, then the transverse field H_y follows;

$$\begin{aligned} H_y^r(\omega) &= \sum_n \frac{ik_{xn}}{k_\perp^2} a_n^+ (e^{ik_{xn}x} + e^{2ik_{xn}w_1} e^{-ik_{xn}x}) \frac{\partial}{\partial y} h_n(y,z) \\ &= \sum_n \frac{ik_{xn}}{k_\perp} a_n^+ (e^{ik_{xn}x} + e^{2ik_{xn}w_1} e^{-ik_{xn}x}) g_n^2(y,z), \end{aligned} \tag{5.27}$$

where

$$k_\perp = \frac{(n+\frac{1}{2})\pi}{w_2}.$$

Substituting the expression for a_n^+ into H_y^r, we obtain

$$H_y^r(\omega) \mid_{x=w_1} = \sum_n \frac{\alpha}{k_\perp} \frac{\sin(k_{xn}dx)}{\sin(k_{xn}w_1)} g_n^2(y,z). \tag{5.28}$$

The current produced by the charged particle on the interface 2 is the coefficient of the $g_n^2(y,z)$,

$$(i_n^2)_0 = -q \frac{2\sin(\omega \frac{dz}{2c})}{\omega} \sqrt{\frac{2}{dz w_2}} \frac{\sin k_{xn}dx}{\sin k_{xn}w_1}. \tag{5.29}$$

Observe that the current $(i_n^2)_0$, which is the dipole current we are interested in, is proportional to the quantity dx when dx is very small. This is the result of the boundary condition we imposed at $x = 0$.

In terms of an analogy with the circuit model, the above quantity is to be compared with the I_0^2 in the Fig. 5.4(b). The difference is the extra index n here.

Similarly, we obtain

$$H_y^l \mid_{x=0}^{y=0} = \sum_n q \frac{2\sin(\omega \frac{dz}{2c})}{\omega} \frac{2}{dz w_2} (\cos(k_{xn}dx) - \cot(k_{xn}w_1)\sin(k_{xn}dx)). \tag{5.30}$$

To obtain the $(i_m^1)_0$, the source current at the interface 1, we follow the same procedure to expand the Fourier component of the field in Fig. 5.6 to obtain

$$\begin{aligned} H_y(\omega) &= \sum_{m=0} (a_m^+(\omega) e^{ik_{ym}y} + a_m^-(\omega) e^{-ik_{ym}y}) h_m(x,z) \\ &= \sum_{m=0} a_m^+(\omega)(e^{ik_{ym}y} - e^{2ik_{ym}w_2} e^{-ik_{ym}y}) h_m(x,z), \end{aligned} \tag{5.31}$$

$$\tag{5.32}$$

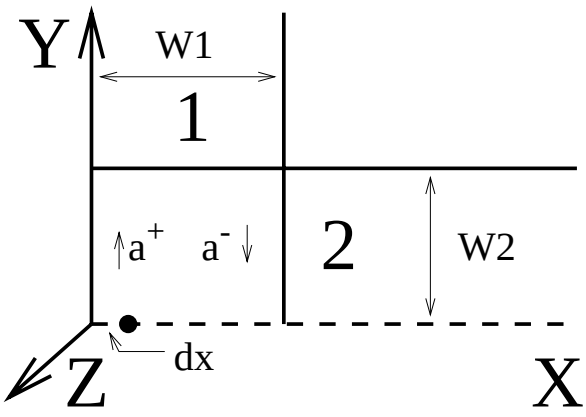

Figure 5.6: Shorted waveguide cross. The long dashed lines are replaced by the solid lines to symbolize the shorting plane and the large black dot is the beam position.

where

$$h_m(x,z) = \sqrt{\frac{2}{w_1 dz}}\cos(m\pi\frac{x}{w_1}) \qquad \text{and} \qquad k_{ym} = \sqrt{(\frac{\omega}{c})^2 - (\frac{m\pi}{w_2})^2}.$$

We used the fact that

$$H_y(\omega)\mid_{y=w2} = 0$$

in arriving at Eq. 5.31.

Similarly, the magnetic field H_y satisfies

$$\frac{1}{c^2}\frac{\partial^2}{\partial t^2}H_y - \nabla^2 H_y = \frac{4\pi}{c}(-)\frac{\partial}{\partial x}J_z, \tag{5.33}$$

where $J_z = qc\delta(x-dx)\delta(y)\delta(z-ct)$. Integrating Eq. 5.33 from $-\epsilon$ to $+\epsilon$ in y direction, and taking its Fourier transform, we obtain

$$\frac{\partial}{\partial y}H_y(\omega)\mid_{+\epsilon} - \frac{\partial}{\partial x}H_y(\omega)\mid_{-\epsilon} = \frac{2q}{c}\delta'(x-dx)e^{i\frac{\omega}{c}z}. \tag{5.34}$$

Because of the symmetry boundary on the x axis, left hand side of Eq. 5.34 is twice the first term. Taking account of the orthogonality of h_m and integrating over z from $-dz/2$ to $dz/2$, we find

$$a_m^+ = \frac{q}{ik_{ym}}\frac{sin(\frac{\omega dz}{c2})}{\omega}\sqrt{\frac{2}{w_1 dz}}\frac{m\pi}{w_1}\sin(m\pi\frac{dx}{w_1})\frac{e^{ik_{ym}w_2}}{\cos(k_{ym}w_2)}. \tag{5.35}$$

By regarding H_y as the longitudinal field of the TE modes, we obtain

$$\begin{aligned} H_x(\omega) &= \sum_{m=0} \frac{ik_{ym}}{k_\perp^2}(e^{ik_{ym}y} + e^{2ik_{ym}w_2}e^{-ik_{ym}y})\frac{\partial}{\partial x}h_m(x,z) \\ &= \sum_{m=0} \frac{ik_{ym}}{k_\perp}(e^{ik_{ym}y} + e^{2ik_{ym}w_2}e^{-ik_{ym}y})g_m^1(x,z). \end{aligned} \tag{5.36}$$

the current $(i_m^1)_0$, as the coefficient of g_m^1 is

$$(i_m^1)_0 = q\frac{2\sin(\omega\frac{dz}{2c})}{\omega}\sqrt{\frac{2}{dzw_2}}\frac{\sin\frac{m\pi dx}{w_1}}{\cos k_{ym}w_2}, \tag{5.37}$$

The magnetic field H_y at the center is also derived to give

$$H_y\ |_{x=0}^{y=0} = \sum_m -q\frac{2\sin(\omega\frac{dz}{2c})}{\omega}\sqrt{\frac{2}{w_1dz}}\frac{\frac{m\pi}{w_1}}{k_{ym}}\tan(k_{ym}w_2)\sin(\frac{m\pi}{w_1}dx). \tag{5.38}$$

We note that the magnetic fields in the cavity region is the same for these two expansion, merely being expressed in terms of different expansion functions.

From the discussion of the circuit model, it is clear that we need the admittance matrix which relates the port currents with port voltages. To calculate the admittance matrix elements, we first short the interface 1, and provide a voltage at the interface 2, just as we did in the black box circuit example in Fig. 5.4(d). The configuration is illustrated in Fig. 5.7. The Fourier component of the electric field E_z

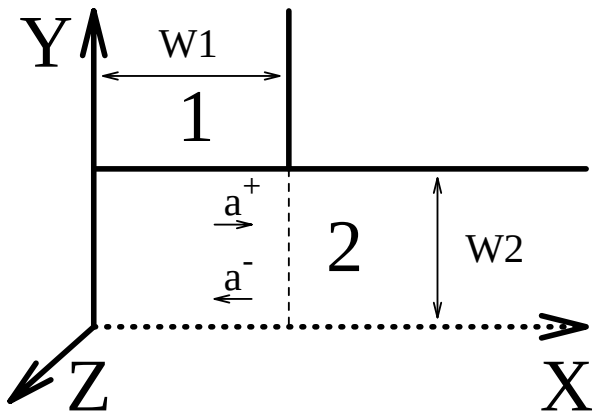

Figure 5.7: The configure to calculate the admittance matrix. The assumed voltage is applied on the thin dashed line.

on the thin dashed line[1], when expanded in the waveguide modes, becomes

$$E_z^2(\omega)\mid_{x=w_1} = \sum_n e_n^2 f_n^2(y,z), \tag{5.39}$$

where $f_n^2(y,z)$ is defined in Eq. 5.18.

The field in the region $x < w_1$ can be naturally expanded in terms of left propagating and right propagating components as

$$\begin{aligned} E_z^2(\omega) &= \sum_n (a_n^+ e^{ik_{xn}x} + a_n^- e^{-ik_{xn}x}) f_n^2(y,z) \\ &= \sum_n a_n^+ (e^{ik_{xn}x} - e^{-ik_{xn}x}) f_n^2(y,z), \end{aligned} \tag{5.40}$$

where the boundary condition at $x = 0$, $E_z^2(x=0) = 0$, has been taken into account. Comparing Eqs. 5.39 and 5.40, we find

$$a_n^+ = \frac{e_n^2}{e^{ik_{xn}w_1} - e^{-ik_{xn}w_1}}. \tag{5.41}$$

If we regard the E_z field as the transverse field of the waveguide TE mode, the associated $H_y(\omega)$ field obtained by Eq. A.17 is (notice that the propagation direction is x instead of z.)

$$\begin{aligned} H_y(\omega) &= \sum_n -\frac{ck_{xn}}{\omega} a_n^+ ik_{xn}(e^{ik_{xn}x} + e^{-ik_{xn}x}) f_n^2(y,z) \\ &= \sum_n -\frac{ck_{xn}}{\omega} \frac{e^{ik_{xn}x} + e^{-ik_{xn}x}}{e^{ik_{xn}w_1} - e^{-ik_{xn}w_1}} e_n^2 g_n^2(y,z). \end{aligned} \tag{5.42}$$

Thus, the current on the interface 1 ($x = w_1$) is

$$i_n^2 = \frac{ck_{xn}}{\omega} i \cot(k_{xn}w_1) e_n^2. \tag{5.43}$$

Similarly, the longitudinal $H_x(\omega)$ field can also be obtained from Eq. A.9 as

$$\begin{aligned} H_x(\omega) &= \sum_n \frac{c}{i\omega} a_n^+ (e^{ik_{xn}x} - e^{-ik_{xn}x})(-\frac{\partial}{\partial y}) f_n^2(y,z) \\ &= \sum_n \frac{ck_\perp}{i\omega} e_n^2 \frac{e^{ik_{xn}x} - e^{-ik_{xn}x}}{e^{ik_{xn}w_1} - e^{-ik_{xn}w_1}} \sqrt{\frac{2}{dzw_2}} \sin\frac{(n+\frac{1}{2})\pi y}{w_2}. \end{aligned} \tag{5.44}$$

[1] there are no E_y components because, as mentioned before, we are only including the z independent modes.

For $y = w_2$, we have

$$H_x(\omega) \mid_{y=w_2} = \frac{ck_\perp}{i\omega} \frac{\sin(k_{xn}x)}{\sin(k_{xn}w_1)} \sqrt{\frac{2}{dzw_2}} (-1)^n e_n^2. \tag{5.45}$$

The currents on the interface 2 are then

$$\begin{aligned} i_m^1 &= \sum_n \int_0^{w_1} dx \int_{-\frac{dz}{2}}^{\frac{dz}{2}} dz \frac{ck_\perp}{i\omega} \frac{\sin(k_{xn}x)}{\sin(k_{xn}w_1)} \sqrt{\frac{2}{dzw_2}} (-1)^n g_m^1(x,z) e_n^2 \\ &= \sum_n \frac{2c}{i\omega} \frac{(-)^{m+n+1}}{\sqrt{w_1 w_2}} \frac{\frac{m\pi}{w_1} \frac{(n+\frac{1}{2})\pi}{w_2}}{(\frac{\omega}{c})^2 - (\frac{m\pi}{w_1})^2 - (\frac{(n+\frac{1}{2})\pi}{w_2})^2} e_n^2. \end{aligned} \tag{5.46}$$

The admittance matrix elements are

$$Y_{mn}^{12} = \frac{2c}{i\omega} \frac{(-)^{m+n+1}}{\sqrt{w_1 w_2}} \frac{\frac{m\pi}{w_1} \frac{(n+\frac{1}{2})\pi}{w_2}}{(\frac{\omega}{c})^2 - (\frac{m\pi}{w_1})^2 - (\frac{(n+\frac{1}{2})\pi}{w_2})^2}, \quad \text{and} \tag{5.47}$$

$$Y_{n'n}^{22} = \frac{ck_{xn}}{\omega} i \cot(k_{xn}w_1) \delta_{n'n}. \tag{5.48}$$

Similarly, by assuming a voltage across interface 1, and shorting interface 2 as in Fig. 5.8, we are able to calculate the fields at the junctions; in particular, the

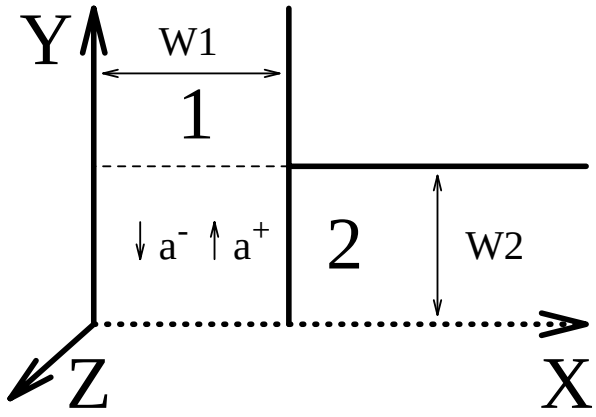

Figure 5.8: The configure to calculate the admittance matrix. The assumed voltage is applied on the thin dashed line.

fields $H_x(\omega)$ and $H_y(\omega)$ are

$$H_x(\omega) = \sum_m \frac{ck_{ym}}{\omega} \frac{i\sin(k_{ym}y)}{\cos(k_{ym}w_2)} e_m^1 f_m^1(x,z) \quad \text{and} \tag{5.49}$$

$$H_y(\omega) = \sum_m \frac{c}{\omega} \frac{i\cos(k_{ym}y)}{\cos(k_{ym}w_2)} e_m^1 \sqrt{\frac{2}{w_1 dz}} \frac{m\pi}{w_1} \cos(\frac{m\pi}{w_1}x). \tag{5.50}$$

Following the above expression, the resulting currents can be determined on both interface 1 and 2. Therefore, the admittance matrix elements are

$$Y^{21}_{nm} = \frac{2c}{i\omega}\frac{(-)^{m+n+1}}{\sqrt{w_1 w_2}}\frac{\frac{m\pi}{w_1}\frac{(n+\frac{1}{2})\pi}{w_2}}{(\frac{\omega}{c})^2-(\frac{m\pi}{w_1})^2-(\frac{(n+\frac{1}{2})\pi}{w_2})^2} \quad \text{and} \tag{5.51}$$

$$Y^{11}_{m'm} = \frac{ck_{ym}}{\omega} i\tan(k_{ym}w_2)\delta_{m'm}. \tag{5.52}$$

The waveguide junction is completely characterized by the admittance matrix, which relates the port currents with port voltages. The consistent solution of the cross waveguide is

$$\begin{pmatrix} i^1_m \\ i^2_n \end{pmatrix} = \begin{pmatrix} Y^{11} & Y^{12} \\ Y^{21} & Y^{22} \end{pmatrix}\begin{pmatrix} e^1_m \\ e^2_n \end{pmatrix} + \begin{pmatrix} (i^1_m)_0 \\ (i^2_n)_0 \end{pmatrix} = Y^c \begin{pmatrix} e^1_m \\ e^2_n \end{pmatrix}, \tag{5.53}$$

where Y^c is the diagonal matrix with the characteristic admittance of the outgoing waves. The last equal sign is the *matching* condition for outgoing waves.

The resulting voltage on the surface can be easily solved:

$$\begin{pmatrix} e^1_m \\ e^2_n \end{pmatrix} = (Y^c - Y)^{-1}\begin{pmatrix} (i^1_m)_0 \\ (i^2_n)_0 \end{pmatrix}, \tag{5.54}$$

where Y is understood as the admittance matrix. The indices n and m both run from 1 to ∞, but since the value of any fixed row or column element falls off as m^{-2} or n^{-2}, it is quite safe to truncate the series. A numerical solution of e_n's is obtained.

At last, from Eqs. 5.42, 5.50 and 5.38, the total H_y at $x = y = 0$, is obtained

$$\begin{aligned} H_y(\omega) &= \sum_n \frac{ck_{xn}}{\omega}\frac{i}{\sin(k_{xn}w_1)}\sqrt{\frac{2}{w_2 dz}}e^2_n \\ &+ \sum_m \frac{c}{i\omega}\frac{m\pi}{w_1}\frac{i}{\cos(k_{ym}w_2)}\sqrt{\frac{2}{w_1 dz}}e^1_m \\ &+ \sum_m -q\frac{2\sin(\omega\frac{dz}{2c})}{\omega}\frac{2}{w_1 dz}\frac{\frac{m\pi}{w_1}}{k_{ym}}\tan(k_{ym}w_1)\sin(\frac{m\pi}{w_1}dx). \end{aligned} \tag{5.55}$$

As a result, the dipole wakefield

$$W_\perp(t) = \int \tilde{W}_\perp(\omega)e^{-i\omega t} = \int \frac{H_y(\omega)}{qdx}e^{-i\omega t}d\omega \tag{5.56}$$

is readily available. Careful observation reveals that each term in Eq. 5.55 has poles at the modes of the cavity formed by shorting the waveguides, i.e. $k_{xn}w1 = m\pi$ or equivalently $k_{ym}w_2 = (n + \frac{1}{2})\pi$. There are, of course, no such resonances because the waveguides are not shorted. It is the sum of all 3 terms which cancels the spurious cavity mode resonances.

The persistent wakefield, as a special term of the wakefield, is obtained by using Eq. 3.58 in Section 3.3.3. Essentially the integrand of Eq. 5.56 is expanded at the cutoff of the waveguide modes in terms of the corresponding wave number k (either k_{xn} or k_{ym}). The last term of Eq. 5.55, caused by the currents $(i_m^1)_0$ or equivalently, $(i_n^2)_0$, is an even function of k. Therefore they have no branch point singularity. Thus, for the purpose of extracting the persistent wakefield, we omit them. In the numerical calculation, we determined the coefficient of the k term, $F(1)$ in Eq. 3.58, by means of a finite difference quotient.

The resulting persistent wakefield is written as a sum of the contribution from each waveguide mode.

$$W_p(t) = \sum_j \gamma_j t^{-\frac{3}{2}} \sin(\omega_j^c t + \phi_j), \tag{5.57}$$

where

$$\gamma_j = \sqrt{\frac{\pi}{2}} F_j(1). \tag{5.58}$$

Comparison

In the previous sections, our mode matching calculation is based on point charge excitation. In order to compare the result with actual simulations done with finite bunch length, a form factor has to be put in to reflect the bunch structure. The wakefield $W^b(t)$ of a bunch with bunch profile $\rho(t)$ is

$$W^b(t) = \int \rho(t')W(t - t')dt' = \int \tilde{\rho}(\omega)\tilde{W}(\omega)e^{-i\omega t}d\omega, \tag{5.59}$$

where $\tilde{\rho}$ is the Fourier transform of the $\rho(t)$. The Fourier transform of a Gaussian beam profile is also a Gaussian. The Gaussian expression prohibits straightforward

contour closure. At large t, however, we can use the saddle point method (see page 118) to derive

$$W^b(t) = \sum_j \gamma_j \tilde{\rho}(\omega_j^c) t^{-\frac{3}{2}} \sin(\omega_j^c t + \phi_j), \tag{5.60}$$

the same as Eq. 5.57 except for the form factor $\tilde{\rho}$.

We have shown the persistent wakefield of the cross in Fig. 4.2(a), where one persistent mode (TE^{10}) is clearly visible. The higher frequency modes are suppressed because the bunch length (2.7 mm) corresponds to a form factor with fairly narrow frequency width. A shorter bunch length (1.35mm) case was also run, and the wakefield is displayed in Fig. 5.9. The persistent nature ($t^{-\frac{3}{2}}$) is also dominant, and

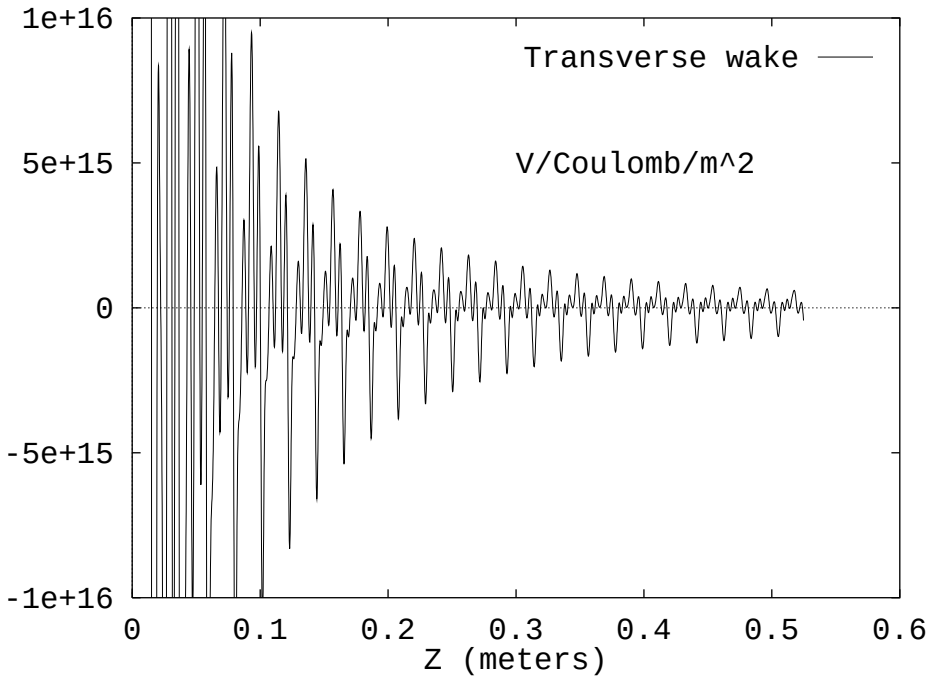

Figure 5.9: Wakefield with a 1.35 mm beam in the waveguide cross.

higher order harmonics are clearly present. In order to determine the higher order persistent mode amplitude the envelope method previously used in Chapter 4 does not apply. We therefore take a section of the wakefield from a MAFIA time domain calculation at a time when the persistent wake dominates, multiply by $t^{\frac{3}{2}}$, and then Fourier transform to obtain its amplitude and phase. Since all the waveguide modes

are harmonics of the TE^{10} mode, only a section of the wakefield with length equal to the cutoff wavelength of TE^{10} is needed.

Table 5.1 compares amplitudes and phases of the mode matching calculation with that from the MAFIA simulation.

Beam length	Mode number	MAFIA		Mode matching	
		amplitude	phase ϕ_j	amplitude	phase ϕ_j
2.7mm	TE_{10}	1.69468×10^7	-0.8528819	1.73054×10^7	-0.825266
	TE_{20}	0.324174×10^7	0.6851612	0.32468×10^7	0.637734
	TE_{30}	0.161986×10^7	0.9210403	0.157393×10^7	0.858344
1.35mm	TE_{10}	2.1428×10^7	-0.8481099	2.18093×10^7	-0.825266
	TE_{20}	0.822358×10^7	0.6949352	0.819026×10^7	0.637734
	TE_{30}	1.27451×10^7	0.9868003	1.26221×10^7	0.858344
0	TE_{10}			2.35575×10^7	-0.825266
	TE_{20}			1.11492×10^7	0.637734
	TE_{30}			2.52646×10^7	0.858344

Table 5.1: Comparison of the MAFIA and mode matching calculations of the persistent wake parameters of the waveguide cross. The mode matching calculation uses 20 modes in each waveguide. A finite difference quotient method is used to obtain the persistent amplitude.

The amplitudes are in quite good agreement, but a small phase discrepancy exists, which can be attributed to the numerical error of MAFIA. We notice that the phase discrepancy increases with higher mode number, which indicates poorer modeling of the rapid oscillations in the transverse direction. The discrepancy was originally larger than that shown in the table. The original values have been adjusted by applying the correction described below.

As a check on the reliability of the phase extracted from our MAFIA time domain simulations we calculated the persistent wake of a straight waveguide shorted at one end, a configuration for which an analytic result for the persistent wakefield phase is available. We found out that the MAFIA computed phase was in error by an amount related to the distance away from the source particle. The error at zero distance was obtained by linear extrapolation. After the linear correction, the

agreement of all the modes improves significantly. There is a small residual error which increases with mode number, indicating higher order errors. The entries in Table 5.1 were adjusted by a similar linear phase correction scheme, which also improves the agreement.

5.1.2 Mode Matching for More Complex Geometries

We have illustrated the mode matching method on a waveguide cross. With the help of S-matrices, more complex geometries can be solved. To illustrate the procedure, we will consider the geometry shown in Fig. 5.10. To make the drawing

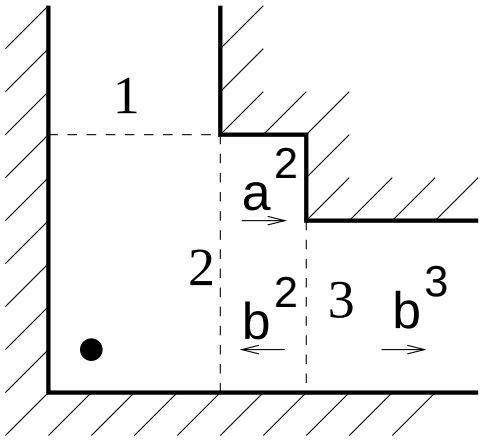

Figure 5.10: A larger cavity loaded by waveguides. The dot represents the source.

simpler, we arbitrarily place the source and assume the metal wall on the lower x and y boundaries. Following the previous section, we are able to find the current $(i_m^1)_0$ and $(i_n^2)_0$ due to the source if surfaces 1 and 2 are shorted. Also the impedance matrix $Y^{\mathbf{12}}$ is available from our previous calculation, which gives

$$\begin{pmatrix} i^1 \\ i^2 \end{pmatrix} = Y^{\mathbf{12}} \begin{pmatrix} e^1 \\ e^2 \end{pmatrix} + \begin{pmatrix} (i^1)_0 \\ (i^2)_0 \end{pmatrix}. \tag{5.61}$$

We have omitted the subscripts m and n.

From the outgoing boundary condition, we have

$$i^1 = Y^{1c} e^1 \tag{5.62}$$

on port 1. On port 2, we need to use the S-matrix $S^{\mathbf{23}}$ connecting ports 2 and 3. From the definition, we have

$$\begin{pmatrix} b^2 \\ b^3 \end{pmatrix} = S^{\mathbf{23}} \begin{pmatrix} a^2 \\ 0 \end{pmatrix}, \tag{5.63}$$

where we have used the fact that there is no incoming wave at port 3. From

$$e^2 = a^2 + b^2 = a^2 + S_{22}^{\mathbf{23}} a^2, \tag{5.64}$$

we obtain

$$a^2 = (1 + S_{22}^{\mathbf{23}})^{-1} e^2 \qquad \text{and} \qquad b^2 = (1 - (1 + S_{22}^{\mathbf{23}})^{-1}) e^2. \tag{5.65}$$

Thus the current and voltage are related by

$$i^2 = Y^{2c}(a^2 - b^2) = Y^{2c}(2(1 + S_{22}^{\mathbf{23}})^{-1} - 1) e^2. \tag{5.66}$$

Putting Eq. 5.61, 5.62, and 5.66 together yields

$$Y^{\mathbf{12}} \begin{pmatrix} e^1 \\ e^2 \end{pmatrix} + \begin{pmatrix} (i^1)_0 \\ (i^2)_0 \end{pmatrix} = \begin{pmatrix} Y^{1c} e^1 \\ Y^{2c}(2(1 + S_{22}^{\mathbf{23}})^{-1} - 1) e^2 \end{pmatrix}. \tag{5.67}$$

Eq. 5.67 can be solved to obtain the voltages e^1 and e^2, which gives the fields in the junction.

With concatenation of S-matrices, even more complex geometries can be solved, for example, the fields in the irised structure, shown in Fig. 5.11, are obtained by solving

$$Y^{\mathbf{12}} \begin{pmatrix} e^1 \\ e^2 \end{pmatrix} + \begin{pmatrix} (i^1)_0 \\ (i^2)_0 \end{pmatrix} = \begin{pmatrix} Y^{1c}(2(1 + S_{11}^{\mathbf{14}})^{-1} - 1) e^1 \\ Y^{2c}(2(1 + S_{22}^{\mathbf{23}})^{-1} - 1) e^2 \end{pmatrix}. \tag{5.68}$$

The S-matrices $S^{\mathbf{23}}$ and $S^{\mathbf{14}}$ can be calculated from the concatenation formula derived in Appendix A.3.

5.1.3 Mode Matching Calculation of S-matrix

The scattering matrix, defined in Appendix A.2, is an important quantity in describing microwave junctions. We have shown in the early sections how to calculate

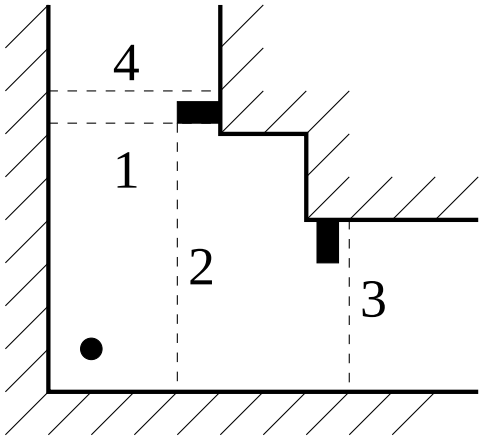

Figure 5.11: A complicated cavity with waveguide loading. The dot represents the source.

the S-matrix of a step. With mode matching on 2 orthogonal surfaces at the same time, we can solve the ninety degree bend problem in a similar way.

H-bend and E-bend

To illustrate the procedure, we calculate the S-matrix of a rectangular bend, as in Fig. 5.12. The admittance matrix of the "H-bend" is closely related to the one we calculated in the previous section. Only the lower y boundary condition is different. The transverse field expansion on the interface is then

$$\vec{E}_\perp = \sum_p e_p \vec{f}_p \qquad \text{and} \qquad \vec{H}_\perp = \sum_p i_p \vec{g}_p, \tag{5.69}$$

where

$$\vec{f}^1_m = \sqrt{\frac{2}{w_1}} \sin(\frac{m\pi}{w_1}x)\hat{z}, \qquad \vec{g}^1_m = -\sqrt{\frac{2}{w_1}} \sin(\frac{m\pi}{w_1}x)\hat{x}, \qquad m = 1, 2, ..., \tag{5.70}$$

$$\vec{f}^2_n = \sqrt{\frac{2}{w_2}} \sin(\frac{n\pi}{w_2}y)\hat{z}, \qquad \vec{g}^2_n = \sqrt{\frac{2}{w_2}} \sin(\frac{n\pi}{w_2}y)\hat{y}, \qquad n = 1, 2, ..., \tag{5.71}$$

where the z dimension is completely dropped. The admittance matrix Y relating e_p's and i_p's becomes

$$Y^{11}_{m'm} = -\frac{ck_{ym}}{\omega} \frac{e^{ik_{ym}w_2} + e^{-ik_{ym}w_2}}{e^{ik_{ym}w_2} - e^{-ik_{ym}w_2}} \delta_{m'm}, \tag{5.72}$$

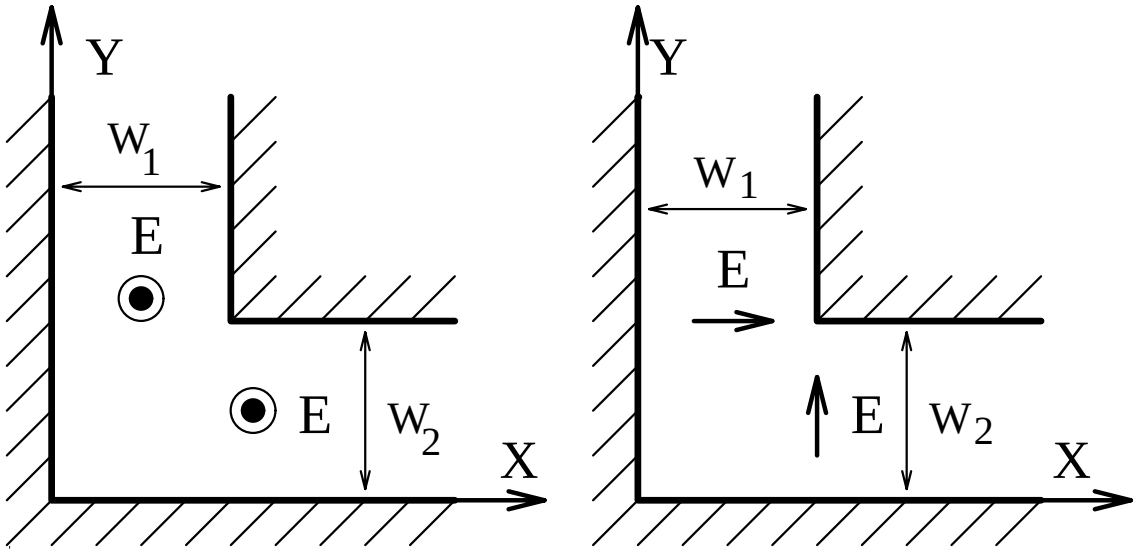

Figure 5.12: A 90° bend. (a): rectangular waveguide bend with TE^{01} mode, i.e. electric field pointing in/out of paper, called H-bend. (b) rectangular waveguide bend with TE^{10} mode, i.e. electric field going across waveguide, called E-bend.

$$Y^{21}_{nm} = \frac{c}{i\omega}\frac{2}{\sqrt{w_1 w_2}}\frac{(-)^{m+n+1}\frac{m\pi}{w_1}\frac{n\pi}{w_2}}{(\frac{\omega}{c})^2-(\frac{m\pi}{w_1})^2-(\frac{n\pi}{w_2})^2}, \tag{5.73}$$

$$Y^{12}_{mn} = \frac{c}{i\omega}\frac{2}{\sqrt{w_1 w_2}}\frac{(-)^{m+n+1}\frac{m\pi}{w_1}\frac{n\pi}{w_2}}{(\frac{\omega}{c})^2-(\frac{m\pi}{w_1})^2-(\frac{n\pi}{w_2})^2}, \tag{5.74}$$

$$Y^{22}_{n'n} = -\frac{ck_{xn}}{\omega}\frac{e^{ik_{xn}w_1}+e^{-ik_{xn}w_1}}{e^{ik_{xn}w_1}-e^{-ik_{xn}w_1}}\delta_{n'n}, \tag{5.75}$$

where

$$k_{xn}=\sqrt{(\frac{\omega}{c})^2-(\frac{n\pi}{w_2})^2} \qquad \text{and} \qquad k_{ym}=\sqrt{(\frac{\omega}{c})^2-(\frac{m\pi}{w_1})^2}. \tag{5.76}$$

The S-matrix is then computed from the formula

$$S=(1+Y)^{-1}(1-Y). \tag{5.77}$$

For further discussion see Appendix A.2.

We used the dimensions of a standard WR90 waveguide rectangular bend, ($w_1 = w_2 = 0.9$ inch) and calculated the TE^{01} mode reflection coefficient at 11.424 GHz. In carrying out the S-matrix calculation, Eq. A.27, we used 10 modes in each

waveguide. The resulting amplitude and phase agree very well with values from the "Waveguide handbook" [25] as shown in Table 5.2. The error from the "Waveguide handbook" is about 1%, so is the mode truncation error.

H-bend	Handbook	Mode matching
S_{11}	0.769 +0.052 I	0.770 +0.053 I

Table 5.2: Numerical comparison on the S-matrix of the H-bend.

In the case of the E-bend, it is the TM modes that are involved (again, we have assumed uniform z dependence). The only quantities involved are H_z, E_x, and E_y. Thus, the transverse field expansion is

$$\vec{E}_\perp = \sum_p e_p \vec{f}_p \qquad\qquad \vec{H}_\perp = \sum_p i_p \vec{g}_p, \tag{5.78}$$

where

$$\vec{f}^1_m = \sqrt{\frac{2}{w_1}}\cos(\frac{m\pi}{w_1}x)\hat{x}, \qquad \vec{g}^1_m = \sqrt{\frac{2}{w_1}}\cos(\frac{m\pi}{w_1}x)\hat{z}, \qquad m = 0, 1, 2, ..., \tag{5.79}$$

$$\vec{f}^2_n = \sqrt{\frac{2}{w_2}}\cos(\frac{n\pi}{w_2}y)\hat{y}, \qquad \vec{g}^2_n = -\sqrt{\frac{2}{w_2}}\cos(\frac{n\pi}{w_2}y)\hat{z}, \qquad n = 0, 1, 2, ... \tag{5.80}$$

Notice that the indices m and n start with 0. The admittance matrix elements (using $\vec{H}_\perp = \frac{\omega}{ck_{xn}}\hat{x} \times \vec{E}_\perp$ or $\vec{H}_\perp = \frac{\omega}{ck_{ym}}\hat{y} \times \vec{E}_\perp$),

$$Y^{11}_{m'm} = -\frac{\omega}{ck_{ym}}\frac{e^{ik_{ym}w_2} + e^{-ik_{ym}w_2}}{e^{ik_{ym}w_2} - e^{-ik_{ym}w_2}}\delta_{m'm}, \tag{5.81}$$

$$Y^{21}_{nm} = \frac{\omega}{ic}\frac{2}{\sqrt{w_1 w_2}}\frac{(-)^{m+n+1}}{(\frac{\omega}{c})^2 - (\frac{m\pi}{w_1})^2 - (\frac{n\pi}{w_2})^2}, \tag{5.82}$$

$$Y^{12}_{mn} = \frac{\omega}{ic}\frac{2}{\sqrt{w_1 w_2}}\frac{(-)^{m+n+1}}{(\frac{\omega}{c})^2 - (\frac{m\pi}{w_1})^2 - (\frac{n\pi}{w_2})^2} \quad \text{and} \tag{5.83}$$

$$Y^{22}_{n'n} = -\frac{\omega}{ck_{xn}}\frac{e^{ik_{xn}w_1} + e^{-ik_{xn}w_1}}{e^{ik_{xn}w_1} - e^{-ik_{xn}w_1}}\delta_{n'n}, \tag{5.84}$$

follow.

So far, we have dealt with z independent modes. The S-matrix of the z dependent modes, as an extension to the previous results, are derived by observing

first, modes with different z variation are independent from one another because of the symmetry; second, by taking the z independent solution $H_z(x,y)$ in the H-bend and $E_z(x,y)$ in the H-bend as the TE and TM eigenmodes of the waveguide (propagating in z direction), respectively, solutions of the z dependent modes can be obtained by superimposing 2 waves with opposite wave number in the z direction. The solutions obtained usually have mixed TE and TM modes if viewed in ports 1 and 2. Linear combination of the solutions are derived to give the S-matrix.

Fortunately, we only need to calculate the reflection coefficient of the TE^{10} mode (one variation in the z direction, no variation in x or y directions). There is no TM^{10} with which to be mixed. The z independent E-bend calculation at frequency $\frac{1}{2\pi}\sqrt{\omega^2-(\frac{c\pi}{dz})^2}$ yields the result.

A standard WR90 waveguide is also utilized to test the accuracy of the method. The values of w_1 and w_2 are chosen to be the narrow dimension, 0.4 inch, the z dimension is 0.9 inch. At 11.424 GHz, we calculated the z independent E-bend S-matrix at $\sqrt{11.424^2-(\frac{c\times 10^{-9}}{0.9\times 2\times 0.0254})^2}$ = 9.3548 GHz with 10 modes in each waveguide. The result agrees very well with that from "Waveguide Handbook" [26].

E-bend	Handbook	Mode matching
S_{11}	0.610 -0.307 I	0.608 -0.307 I

Table 5.3: Numerical comparison on the S-matrix of the E-bend.

5.2 General Conditions Satisfied by S-matrix Including Non Propagating Modes

In numerical calculations, non-propagating modes are frequently encountered. In the cascading formula above, evanescent modes in region 2 are actually very important because they do penetrate the short distance L. While the amplitude scattering matrix defined later in the section is unitary with propagating modes

only, thus widely used, it is easier to work with voltage scattering matrix to derive a generalized unitary condition when non-propagating modes are involved.

5.2.1 General Property of a Waveguide Junction

It is very difficult in general to calculate the electromagnetic field in a waveguide junction due to the complicated geometry involved. It has been pointed out [27] that a complete solution of an electromagnetic problem is not always desired. Often a description of conditions at the terminals of a junction is sufficient.

Consider a junction made of perfect conductor completely surrounded by an imaginary surface S. This surface cuts the waveguides perpendicularly at some planes called *terminals* as shown in Fig. 5.13.

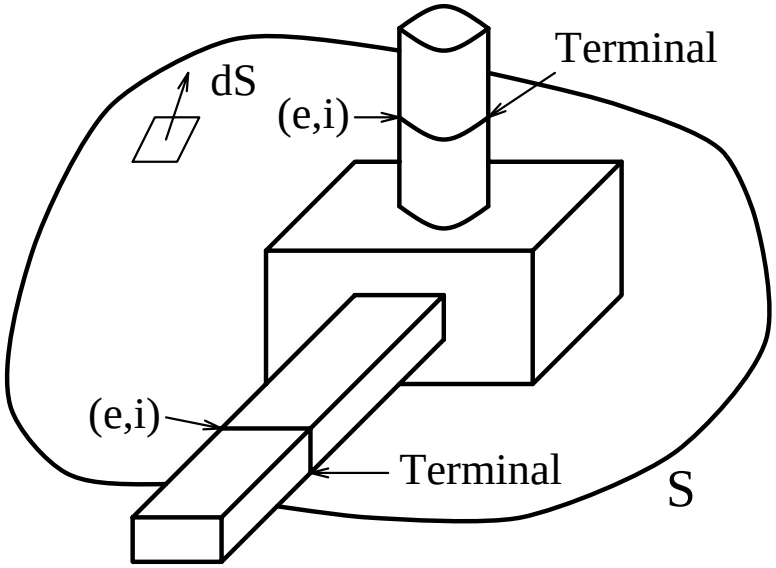

Figure 5.13: Example of a two-terminal junction.

Maxwell's equations for a periodic ($e^{-i\omega t}$) field are

$$\left.\begin{aligned} \nabla \times \vec{E} &= \tfrac{i\omega}{c}\mu\vec{H} \\ \nabla \cdot \epsilon\vec{E} &= 0 \\ \nabla \times \vec{H} &= \tfrac{4\pi}{c}\sigma\vec{E} + \tfrac{-i\omega}{c}\epsilon\vec{E} \\ \nabla \cdot \mu\vec{H} &= 0 \end{aligned}\right\} \tag{5.85}$$

The ϵ, μ, and σ are real here. Then if

$$\nabla \cdot (\vec{E} \times \vec{H}^*) \equiv \vec{H}^* \cdot \nabla \times \vec{E} - \vec{E} \cdot \nabla \times \vec{H}^* = i\omega\mu \vec{H}^* \cdot \vec{H} - (\frac{4\pi}{c}\sigma + \frac{i\omega\epsilon}{c})\vec{E} \cdot \vec{E}^* \quad (5.86)$$

be integrated over the volume enclosed by the surface S and the volume integral converted into a surface integral by Gauss's Theorem, we obtain the Poynting's Theorem:

$$\int_s (\vec{E} \times \vec{H}^*) \cdot d\vec{S} = -\frac{i\omega}{c} \int_v (\epsilon |\vec{E}|^2 - \mu |\vec{H}|^2) dV - \frac{4\pi\sigma}{c} \int_v \vec{E} \cdot \vec{E}^* dV \quad (5.87)$$

Since the field vanishes everywhere over the surface S except at the terminals[2], the surface integral reduced to an integral over the terminals. Since the $d\vec{S}$ is perpendicular to the axis of the waveguide, only the transverse components of $\vec{E}$ and $\vec{H}$ contribute to the integral. Expanding the transverse field as in Eqs. A.18 and A.19, Eq. 5.87 becomes

$$\begin{aligned} \sum_n e_n i_n^* &= \frac{4\pi\sigma}{c} \int_v \vec{E} \cdot \vec{E}^* dV - \frac{i\omega}{c} \int_v (\epsilon |\vec{E}|^2 - \mu |\vec{H}|^2) dV \\ &= 2P + 4i\omega(W_H - W_E), \end{aligned} \quad (5.88)$$

where $\int \vec{f}_n \times \vec{g}_m^* \cdot d\vec{S} = -\delta_{nm}$ follows directed from $\int \vec{f}_n \times \vec{g}_m \cdot d\vec{S} = -\delta_{nm}$ on page 132. W_H and W_E are the average magnetic and electric energy, respectively. A factor of 2 comes from time averaging. Eq. 5.88 provides a connection between the terminal quantities and the field quantities.

Symmetry Condition of Impedance and Admittance Matrices

Let there be two solutions of the Maxwell's equations that satisfy the boundary conditions, the

$$\left.\begin{aligned} \nabla \times \vec{E}^1 &= \tfrac{i\omega}{c}\mu \vec{H}^1 \\ \nabla \times \vec{H}^1 &= \tfrac{4\pi}{c}\sigma \vec{E}^1 + \tfrac{-i\omega}{c}\epsilon \vec{E}^1 \end{aligned}\right\} \quad (5.89)$$

$$\left.\begin{aligned} \nabla \times \vec{E}^2 &= \tfrac{i\omega}{c}\mu \vec{H}^2 \\ \nabla \times \vec{H}^2 &= \tfrac{4\pi}{c}\sigma \vec{E}^2 + \tfrac{-i\omega}{c}\epsilon \vec{E}^2 \end{aligned}\right\} \quad (5.90)$$

[2]It is not precisely true if the waveguide is made of lossy material since the fields penetrate the wall.

follows from Eqs. 5.85. The superscript 1 and 2 is used to distinguish the solutions. Likewise

$$\nabla\cdot(\vec{E}^1\times\vec{H}^2-\vec{E}^2\times\vec{H}^1)=\vec{H}^2\cdot\nabla\times\vec{E}^1-\vec{E}^1\cdot\nabla\times\vec{H}^2-\vec{H}^1\cdot\nabla\times\vec{E}^2+\vec{E}^2\cdot\nabla\times\vec{H}^1. \quad (5.91)$$

From Eqs. 5.89 and 5.90, we obtain

$$\nabla\cdot(\vec{E}^1\times\vec{H}^2-\vec{E}^2\times\vec{H}^1)=0. \quad (5.92)$$

If Eq. 5.92 is integrated over the volume enclosed by the surface,

$$0=\int_v\nabla\cdot(\vec{E}^1\times\vec{H}^2-\vec{E}^2\times\vec{H}^1)dv=\oint_s(\vec{E}^1\times\vec{H}^2-\vec{E}^2\times\vec{H}^1)\cdot d\vec{S} \quad (5.93)$$

holds too. The right hand side of Eq. 5.93 can be expressed in terms of terminal voltage e and current i, which gives

$$0=\sum_j(e_j^1i_j^2-e_j^2i_j^1). \quad (5.94)$$

By substituting the definition of admittance matrix into Eq. 5.94, we obtain

$$0=\sum_{jk}e_j^1Y_{jk}e_k^2-e_j^2Y_{jk}e_k^1=\sum_{jk}(Y_{jk}-Y_{kj})e_j^1e_k^2. \quad (5.95)$$

Since Eq. 5.95 holds for any sets of applied voltages at the terminals, it is obvious that

$$Y_{jk}=Y_{kj}, \qquad \forall\ j,k. \quad (5.96)$$

It can be shown in a similar way that

$$Z_{jk}=Z_{kj}, \qquad \forall\ j,k. \quad (5.97)$$

Therefore impedance and admittance matrices are always symmetric.

5.2.2 Voltage Scattering Matrix

The voltage scattering matrix (VSM) S_v has several general properties of importance. One of them is its symmetry, arising directly from the symmetry condition of Y and Y^c. We have shown the symmetry of Y in the previous section; Y_c is

diagonal, therefore certainly symmetric. Thus

$$\begin{aligned} & S^T Y^c = (Y^c - Y)(Y^c + Y)^{-1} Y^c \\ = \;& Y^c (Y^c + Y)^{-1} Y^c - Y(Y^c + Y)^{-1} Y^c \\ = \;& 2Y^c (Y^c + Y)^{-1} Y^c - (Y + Y^c)(Y^c + Y)^{-1} Y^c \\ = \;& 2Y^c (Y^c + Y)^{-1} Y^c - Y^c \\ = \;& Y^c [2(Y^c + Y)^{-1} Y^c - (Y^c + Y)^{-1}(Y^c + Y)] \\ = \;& Y^c (Y^c + Y)^{-1}(Y^c - Y) = Y^c S. \end{aligned} \tag{5.98}$$

The symmetry condition of Y and Y^c has been used in the first line.

An additional condition is imposed by Eq. 5.88. If Eqs. A.21 and A.24 are substituted in Eq. 5.88,

$$\begin{aligned} (\vec{a}^* + \vec{b}^*) Y^c (\vec{a} - \vec{b}) &= \vec{a}^* (Y^c + S^\dagger Y^c - Y^c S - S^\dagger Y^c S) \vec{a} \\ &= 2P + 4j\omega (W_H - W_E) \end{aligned} \tag{5.99}$$

follows. For a *lossless* junction, i.e. $P = 0$, the real part of Eq. 5.99 vanishes, which is

$$\begin{aligned} 0 &= \vec{a}^* (Y^c + S^\dagger Y^c - Y^c S - S^\dagger Y^c S) \vec{a} + \vec{a} (Y^{c*} + S^{\dagger *} Y^{c*} - Y^{c*} S^* - S^{\dagger *} Y^{c*} S^*) \vec{a}^* \\ &= \vec{a}^* (Y^c + Y^{c\dagger} + S^\dagger Y^c + Y^{c\dagger} S - Y^c S - S^\dagger Y^{c\dagger} - S^\dagger Y^c S - S^\dagger Y^{c\dagger} S) \vec{a}. \end{aligned} \tag{5.100}$$

Since Eq. 5.100 has to be true for any amplitude $\vec{a}$, the sum inside the parenthesis has to vanish, it yields

$$Y^c + Y^{c\dagger} = S^\dagger (Y^c + Y^{c\dagger}) S + S^\dagger (Y^{c\dagger} - Y^c) + (Y^c - Y^{c\dagger}) S. \tag{5.101}$$

Eq. 5.101 is the Generalized Unitary Condition(GUC) for the VSM S_v, the current scattering matrix S_i follows a similar derivation which we will not repeat. The result is given below:

$$S_i = (Z^c + Z)^{-1} (Z^c - Z), \tag{5.102}$$

$$S_i^T Z^c = Z^c S_i, \tag{5.103}$$

$$Z^c + Z^{c\dagger} = S_i^\dagger (Z^c + Z^{c\dagger}) S_i + S_i^\dagger (Z^{c\dagger} - Z^c) + (Z^c - Z^{c\dagger}) S_i. \tag{5.104}$$

5.2.3 Voltage and Amplitude Scattering Matrices

In microwave network analysis, the amplitude scattering matrix is widely used [27] [29]. It follows the same derivation as the voltage scattering matrix except in Eqs. A.18 and A.19, $\vec{f}_n$ and $\vec{g}_n$ are *normalized*:

$$\vec{f}_n \Rightarrow \frac{1}{\sqrt{Y_n^c}}\vec{f}_n \quad , \quad \vec{g}_n \Rightarrow \sqrt{Y_n^c}\vec{g}_n \tag{5.105}$$

So that $\int \vec{f}_n \times \vec{g}_m \cdot d\vec{S} = -\delta_{nm}$ still holds, but f's and g's are not normalized to unity. Eq. A.21 is changed into

$$e_q = a_q + b_q \quad , \quad i_q = (a_q - b_q). \tag{5.106}$$

We need the admittance matrix Y_a, which is given by

$$Y_a = \frac{1}{\sqrt{Y^c}} Y \frac{1}{\sqrt{Y^c}}, \tag{5.107}$$

to obtain the corresponding amplitude scattering matrix

$$S_a = (I + Y_a)^{-1}(I - Y_a). \tag{5.108}$$

It follows from the above two equations that both Y_a and S_a are symmetric and also that

$$S_a = \sqrt{Y^c} S_v \frac{1}{\sqrt{Y^c}} \tag{5.109}$$

holds.

Without DNP modes, we have

$$\begin{aligned} (\vec{a}^* + \vec{b}^*)(\vec{a} - \vec{b}) &= \vec{a}^*(I + S_a^\dagger - S_a - S_a^\dagger S_a)\vec{a} \\ &= 2P + 4j\omega(W_H - W_E). \end{aligned} \tag{5.110}$$

With $P = 0$, the familiar result

$$S_a^\dagger S_a = I \tag{5.111}$$

follows.

GUC, on the other hand, not only contains the same information about scattering matrix elements connecting propagating modes, but also provides extra information about scattering matrix elements related to DNP modes.

Suppose we have a lossless junction with N number of propagating modes and M number of non-propagating modes, the characteristic admittance Y^c and VSM S_v can be written as

$$Y^c = \begin{pmatrix} Y_1 & 0 \\ 0 & jB_2 \end{pmatrix}, \; S_v = \begin{pmatrix} S_{11} & S_{12} \\ S_{21} & S_{22} \end{pmatrix}, \tag{5.112}$$

where Y_1 is a $N \times N$ diagonal matrix with the N characteristic admittances of the propagating modes; jB_2 is a $M \times M$ diagonal matrix with purely imaginary matrix elements. S_v is also split into similar blocks. Inserting them into Eq. 5.101, we obtain

$$\begin{aligned} & \begin{pmatrix} Y_1 & 0 \\ 0 & 0 \end{pmatrix} \\ = & \begin{pmatrix} S_{11}^\dagger & S_{21}^\dagger \\ S_{12}^\dagger & S_{22}^\dagger \end{pmatrix} \begin{pmatrix} Y_1 & 0 \\ 0 & 0 \end{pmatrix} \begin{pmatrix} S_{11} & S_{12} \\ S_{21} & S_{22} \end{pmatrix} \\ & - \begin{pmatrix} S_{11}^\dagger & S_{21}^\dagger \\ S_{12}^\dagger & S_{22}^\dagger \end{pmatrix} \begin{pmatrix} 0 & 0 \\ 0 & jB_2 \end{pmatrix} \\ & + \begin{pmatrix} 0 & 0 \\ 0 & jB_2 \end{pmatrix} \begin{pmatrix} S_{11} & S_{12} \\ S_{21} & S_{22} \end{pmatrix}. \end{aligned} \tag{5.113}$$

It breaks down into 4 equations:

$$Y_1 = S_{11}^\dagger Y_1 S_{11}, \tag{5.114}$$

$$0 = S_{11}^\dagger Y_1 S_{12} - S_{21}^\dagger jB_2, \tag{5.115}$$

$$0 = S_{12}^\dagger Y_1 S_{11} + jB_2 S_{21}, \tag{5.116}$$

$$0 = S_{12}^\dagger Y_1 S_{12} + jB_2 S_{22} - S_{22}^\dagger jB_2. \tag{5.117}$$

Eq. 5.114 is the same as Eq. 5.111. Eqs. 5.115 and 5.116 are complex conjugate of each other. The last three equations can be further simplified if we take generalized symmetry condition into consideration. Substituting Eq. 5.112 into Eq. 5.98,

the symmetry condition becomes

$$\begin{pmatrix} S_{11}^T Y_1 & S_{21}^T jB_2 \\ S_{12}^T Y_1 & S_{22}^T jB_2 \end{pmatrix} = \begin{pmatrix} Y_1 S_{11} & Y_1 S_{12} \\ jB_2 S_{21} & jB_2 S_{22} \end{pmatrix}. \tag{5.118}$$

Eqs. 5.115 and 5.117 become

$$\left.\begin{aligned} S_{21} S_{11}^* &= S_{21}^* \\ \text{or} \quad S_{11}^* S_{12} &= -S_{12}^* \end{aligned}\right\}, \tag{5.119}$$

$$S_{21} S_{12}^* + S_{22} - S_{22}^* = 0. \tag{5.120}$$

They relate S_{21}, S_{12}, and S_{22} with their complex conjugates, respectively, i.e. a generalized reality condition. Current scattering matrix has similar results.

Because of the relationship of amplitude scattering matrix and voltage scattering matrix shown in Eq. 5.109, the generalized unitary condition of the amplitude scattering matrix S_a with DNP modes is readily available by substituting Eq. 5.109 into Eq. 5.101.

Besides the extra information, GUC is exact no matter where you do the mode number truncation, which allows one to check S-matrix in numerical calculations.

Application: Lossy Waveguide

In the presence of a lossy waveguide, the characteristic admittance of the waveguide mode is no longer real. See Fig. 5.14. To simplify the algebra, let us assume only TE^{01} waveguide mode is involved in matching the field at the interface. For a TE mode with electric field pointing out of the paper plane, the characteristic admittance

$$Y^c = \frac{ck_x}{\omega}, \tag{5.121}$$

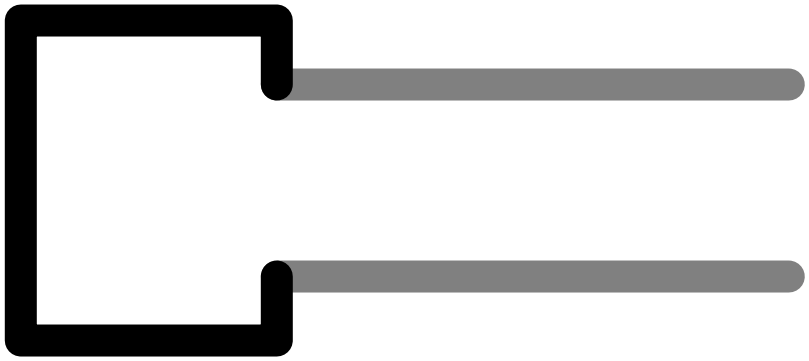

Figure 5.14: Example of a lossy waveguide loaded cavity. The gray lines represent a lossy waveguide and the cavity enclosed in the solid line is assumed to be made of perfect conductor.

where the propagation constant of the waveguide mode $k_x = \frac{1}{c}\sqrt{\omega^2 - \omega_c^2}$. For a lossy[3] waveguide, the field dependency on x becomes

$$e^{ik_x x} e^{-\alpha x} = e^{ik_x(1+\frac{i}{2Q_w})x}, \tag{5.122}$$

where α is the attenuation constant, and $Q_w = \frac{k_x}{2\alpha}$. Therefore the characteristic admittance

$$Y^c = \frac{ck_x}{\omega}(1 + \frac{i}{2Q_w}). \tag{5.123}$$

By substituting Eq. 5.123 into Eq. 5.101, we obtain

$$\frac{2c}{\omega}k_x = S_v^*(\frac{2c}{\omega}k_x)S_v + S_v^*(-\frac{i}{Q_w})\frac{c}{\omega}k_x + \frac{i}{Q_w}\frac{c}{\omega}k_x S_v, \tag{5.124}$$

which simplifies to

$$1 = S_v^* S_v + \frac{i}{2Q_w}(S_v - S_v^*). \tag{5.125}$$

In assuming $S_v = re^{i\theta}$, we obtain

$$1 = r^2 - \frac{\sin\theta}{Q_w}r. \tag{5.126}$$

[3]Strictly speaking, our discussion applies only to the perfect conducting wall, see footnote on page 94. It is still a good approximation if small resistance ρ is introduced to the waveguide wall. First, the waveguide eigenmode distortion is a 2nd order effect. Thus the field expansion is still valid. Second, the difference of the r.h.s. of Eqs. 5.87 and 5.88 is of second order too.
Another way of making the waveguide lossy is to fill the waveguide with material of non-zero σ which has no contradiction with the previous derivation.

The amplitude r is solved to obtain

$$r = \sqrt{1 + \frac{\sin^2\theta}{4Q_w^2}} + \frac{\sin\theta}{2Q_w} \approx 1 + \frac{\sin\theta}{2Q_w}. \tag{5.127}$$

Due to the lossy nature of the waveguide, the scattering matrix of a junction is no longer unitary even though the junction is lossless. The amplitude is phase dependent.

By a similarity transformation, the amplitude scattering matrix

$$S_a = \sqrt{Y^c} S_v \frac{1}{\sqrt{Y^c}} = S_v \tag{5.128}$$

is, in this simple case, the same as voltage scattering matrix. Thus S_a is not unitary either.

Taking the dominant TE^{01} mode as a practical example, the attenuation constant α is [28]

$$\alpha = \sqrt{\frac{\epsilon\omega}{2\sigma}} \frac{1}{b} \frac{1 + \frac{2b}{a}(\frac{\lambda}{2a})^2}{\sqrt{1 - (\frac{\lambda}{2a})^2}}, \tag{5.129}$$

where a and b are the width and height of the waveguide (it assumes that $a > b$), and λ is the free space wavelength, and σ is the conductivity of the metal. The Q_w, therefore follows

$$Q_w = \frac{b}{\delta_s} \frac{1 - (\frac{\lambda}{2a})^2}{\sqrt{\epsilon_r \mu_r}(1 + \frac{2b}{a}(\frac{\lambda}{2a})^2)} \tag{5.130}$$

where δ_s is the skin depth defined as $\sqrt{\frac{2}{\omega\mu\sigma}}$.

Taking WR90 waveguide ($a = 0.9$ inch, $b = 0.4$ inch) at 11.424 GHz for example, the Q_w of copper is 8.52×10^3 and Q_w of stainless steel type 304 is 1.32×10^3. It shows that stainless steel can cause 4×10^{-4} amplitude variation depending on the phase.

Also note that Q_w dropped as the frequency approaches the cutoff of the waveguide mode because of the numerator in the Eq. 5.130. Further more, $\frac{b}{\delta_s}$ is inversely proportional to the square root of frequency. Therefore, at higher frequency and closer to waveguide cutoff, the phase modulation of the scattering matrix amplitude will be appreciable.

5.2.4 Conclusion

We have derived voltage/current scattering matrix including DNP modes from admittance/impedance matrix and their corresponding generalized symmetry, unitary condition. Using a simple example, we have demonstrated the extra information contained in them compared with traditional amplitude scattering matrix applied only to propagating modes. We have also shown an example of lossy waveguide attached to a lossless junction, where the scattering matrix is not unitary.

Chapter 6

Minimum Wakefield Achievable by Waveguide Damping

If one were unaware of the persistent wakefield, one would conclude that the wakefield which remains after some fixed time interval is always reduced by decreasing Q_{ext}, and that limits on achievable wakefield suppression arise from limits on how low a Q_{ext} can be achieved. This is no longer obvious if one takes the persistent wake into account because our simulations have suggested that measures which increase cavity-waveguide coupling strength also tend to increase the strength of the persistent wake. In this chapter we present a circuit model which indicates that for a fixed separation of the lowest resonance from the cutoff and at fixed time delay that there is an optimum rather than a minimum Q_{ext} which minimizes the wakefield.

6.1 Circuit Model

We used two waveguide models in Chapter 3 to illustrate the origin of the persistent wakefield. Despite the simplicity of the geometry of the structures considered the required electromagnetic field computations were quite complex. In this chapter, we will utilize a much simpler equivalent circuit to model the waveguide damped cavity system. By lumping the distributed field into circuit parameters,

the model explicitly demonstrates the relationship between damped and persistent components of the wakefield in a simple mathematical form, thus making significant qualitative statements possible.

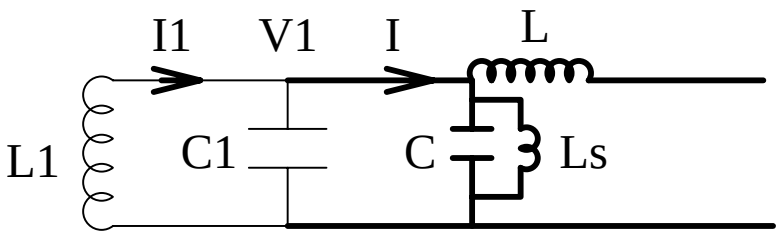

Figure 6.1: The circuit model of a waveguide loaded cavity. Thick line represents a transmission line. L, C, L_s are understood as distributed quantities.

The circuit model is shown in Fig. 6.1. The L_1 and C_1 form a lossless resonant circuit to mimic the cavity. As explained later the transmission line with shunt inductance L_s mimics the waveguide. We note that L and C are inductance and capacitance per unit length, respectively, while L_s is inductance times unit length.

6.1.1 Transmission Line

The differential equations of the transmission line with shunt inductance are explained below. See Fig. 6.2. At a given location x, taking a small increment Δx,

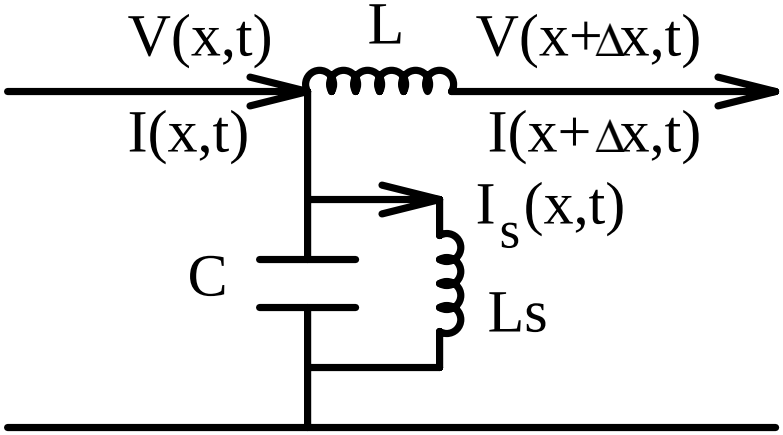

Figure 6.2: Transmission line with shunt inductance.

the voltages are related by

$$V(x+\Delta x,t)-V(x,t)=-L\Delta x\frac{dI}{dt}. \tag{6.1}$$

In the limit $\Delta x \to 0$, the above equation becomes

$$\frac{\partial V}{\partial x}=-L\frac{\partial I}{\partial t}. \tag{6.2}$$

Similarly

$$I(x+\Delta x,t)-I(x,t)=-\frac{dq}{dt}-I_s=-\frac{d}{dt}(C\Delta xV)-I_s, \tag{6.3}$$

where q is the charge on the capacitor C. Also we have

$$\frac{L_s}{\Delta x}\frac{dI_s}{dt}=V. \tag{6.4}$$

Remembering that L_s is the inductance times length, the inductance of a short section Δx is thus $\frac{L_s}{\Delta x}$. Differentiating Eq. 6.3 with respect to time, and utilizing Eq. 6.4, we obtain

$$\frac{\partial^2 I}{\partial x\partial t}=-C\frac{\partial^2 V}{\partial t^2}-\frac{V}{L_s}. \tag{6.5}$$

Combining Eqs. 6.2 with 6.5, we are able to obtain a single equation

$$LC\frac{\partial^2 V}{\partial t^2}-\frac{\partial^2 V}{\partial x^2}+\frac{L}{L_s}V=0 \tag{6.6}$$

involving V only.

For a periodic ($e^{-i\omega t}$) field,

$$\frac{\partial^2 V}{\partial x^2}-(LC\omega^2-\frac{L}{L_s})V=0. \tag{6.7}$$

The solutions are

$$V\sim e^{\pm ikx}, \tag{6.8}$$

with $k=\sqrt{LC}\sqrt{\omega^2-\frac{1}{CL_s}}$. Now we see the purpose of introducing the shunt inductance L_s in the transmission line: it gives rise to a cutoff frequency $\omega_c=\frac{1}{\sqrt{CL_s}}$. There is, in fact, a clear physical correspondence between our inductively shunted transmission line and a rectangular waveguide propagating the TE_{10} mode. The top and

bottom plates correspond to a parallel plate transmission line with series inductance and shunt capacitance, and the side walls provide the shunt inductance.

From Eq. 6.2, the voltage and current of the transmission line mode must be related by

$$\frac{V}{I} = \frac{\omega L}{\pm k} = \pm\sqrt{\frac{L}{C}}\frac{\omega}{\sqrt{\omega^2 - \omega_c^2}} \equiv Z, \tag{6.9}$$

where the $\pm$ sign depends on the direction of the propagating waves: plus for positive x direction, negative for the other.

6.1.2 Resonator with Transmission Line Loading

The differential equation of the voltage V_1 and current I_1 of the cavity follows the familiar equations of capacitance and inductance:

$$\frac{dV_1(t)}{dt} = \frac{1}{C_1}\frac{dQ}{dt} = \frac{1}{C_1}(I_1(t) - I(t)) \quad \text{and} \tag{6.10}$$

$$V_1 = -L_1\frac{dI_1(t)}{dt}, \tag{6.11}$$

where Q is the charge on the capacitor C_1.

The circuit is set up to have initial conditions $V_1(t = 0) = v_0$ and $I_1(t = 0) = 0$. V_1(or equivalently the electric field across the capacitor) is regarded as the longitudinal wakefield of the cavity. It is indeed the case if we have a small hole in the middle of each of the capacitor plates, and charged particles pass through them. In other words, the circuit is very close to a "pill-box" cavity with side wall modeled by the inductance. The initial condition is then equivalent to a charge passing through the "pill-box" cavity instantaneously and building up a voltage between the plates. Therefore V_1 as a function of t gives us a good description of the decaying wakefield.

Multiplying Eqs. 6.10 and 6.11 by $e^{i\omega t}$ and integrating from $t = 0$ to $t \to \infty$, and taking the initial conditions explicitly into account, we find

$$\left.\begin{aligned} \tilde{I}_1 &= \tilde{I} + C_1\textstyle\int_0^\infty \frac{dV}{dt}e^{i\omega t}dt = \tilde{I} - C_1 v_0 - i\omega C_1\tilde{V}_1 \\ &= \tfrac{\tilde{V}_1}{Z} - C_1 v_0 - i\omega C_1\tilde{V}_1 \\ \tilde{V}_1 &= L_1 i\omega\tilde{I}_1 \end{aligned}\right\}, \tag{6.12}$$

where $\tilde{()}$ symbolizes the Fourier transform (we have assumed the quantities to which we have applied the Fourier transform to be zero for negative time). We also used the result from the previous section in writing $\tilde{I}$ as $\frac{\tilde{V_1}}{Z}$ on the second line of Eq. 6.12, where Z is the characteristic impedance of the transmission line defined in Eq. 6.9. Solving Eq. 6.12 for $\tilde{V_1}$ then yields

$$\tilde{V_1} = \frac{i\frac{\omega}{\omega_0^2}v_0}{(\frac{\omega}{\omega_0})^2 + i\frac{R}{Z}\frac{\omega}{\omega_0} - 1}, \tag{6.13}$$

where $\omega_0 = \frac{1}{\sqrt{L_1 C_1}}$, is the natural resonant frequency of the cavity and $R = \sqrt{\frac{L_1}{C_1}}$, is the characteristic impedance of the cavity resonant mode. The inverse Fourier transform brings us the solution in the time domain:

$$\frac{V_1(t)}{v_0} = \frac{1}{2\pi}\int \frac{\tilde{V_1}}{v_0} e^{-i\omega t} d\omega. \tag{6.14}$$

What we have calculated is the *longitudinal* wakefield. The transverse wakefield is related to the longitudinal wakefield by the Panofsky-Wenzel theorem [30].

$$\nabla_\perp V_1 = \frac{\partial}{\partial s} V_\perp, \tag{6.15}$$

where $V_\perp$ is the transverse wakefield and $s = ct$. It states that the transverse gradient of the longitudinal wake potential is equal to the longitudinal gradient of the transverse wake potential. Thus

$$\tilde{V_\perp} = \frac{\omega_\perp}{-i\omega}\tilde{V_1} = \frac{-\frac{\omega_\perp}{\omega_0^2}v_0}{(\frac{\omega}{\omega_0})^2 + i\frac{R}{Z}\frac{\omega}{\omega_0} - 1}. \tag{6.16}$$

The symbol $\omega_\perp$ is a geometric factor related to the detailed shape of the structure. It is not given by our model. An equivalent result is obtained if one identifies $V_\perp$ with the current I_1 multiplied by an impedance (another parameter not given by the model). Physically this corresponds to the fact that the transverse force exerted by a dipole mode is due to its magnetic field.

The wakefield in the time domain

$$V_\perp(t) = \frac{1}{2\pi}\int \tilde{V}_\perp e^{-i\omega t} d\omega \tag{6.17}$$

is obtained from the inverse Fourier transform. The integrand has two branch points from the definition of Z. With a proper choice of branch cut, see Fig. 3.13, the integration is naturally divided into two terms: one from the pole contribution , the other from the branch cut integral.

When $\frac{R}{Z(\omega_0)} \ll 1$, i.e. the damping term is small, the pole of the expression $\tilde{V_\perp}$ is very close to ω_0. For the purpose of calculating the pole and evaluating the residue, $Z(\omega)$ can be taken as $Z(\omega_0)$. Then the poles satisfy

$$(\frac{\omega}{\omega_0}) \mid_{pole} = \pm\sqrt{1-\frac{1}{4Q^2}} - \frac{i}{2Q}, \tag{6.18}$$

where $Q = \frac{Z(\omega_0)}{R}$. The poles are symmetric with respect to the imaginary axis because of reality.

The branch cut integral (persistent wakefield) is evaluated with Eq. 3.58. When $t' \gg 1$, we only need to keep the first term. The total wakefield is

$$\begin{aligned} \frac{1}{v_0\frac{\omega_\perp}{\omega_0}} V_\perp(t) &\approx \frac{-1}{\sqrt{1-\frac{1}{4Q^2}}} \sin(\sqrt{1-\frac{1}{4Q^2}}t')e^{-\frac{t'}{2Q}} \\ &+ \sqrt{\frac{2}{\pi}} \frac{(\frac{\omega_c}{\omega_0})^{1/2}}{(1-(\frac{\omega_c}{\omega_0})^2)^{5/2}} \frac{1}{Q} \cos(\frac{\omega_c}{\omega_0}t' + \frac{1}{4}\pi) \frac{1}{t'^{3/2}} \end{aligned} \tag{6.19}$$

where $t' = \omega_0 t$.

It is clear from the above expression that the persistent wake amplitude is proportional to $\frac{1}{Q}$, which explains the phenomena we observed in Chapter 4, namely, the stronger the damping the larger the persistent wake. It also indicates that as the resonant frequency gets closer to the waveguide cutoff, the persistent wake is enhanced.

It has to be pointed out that in a cavity system without external damping, i.e. $Q \to \infty$, the transverse wakefield is a pure sine curve. It is possible to place bunches at the zero wakefield of the preceding bunches. But when more dipole modes (oscillating at different frequencies) are included, zero wakefield placement is not possible for all of the modes. Zero wakefield placement is not possible for the persistent wakefield either because of its phase.

Eq. 6.19 also tells us the best waveguide damping can do at a certain distance t' behind the source particle. A typical value for NLC is $t' = 40 * \pi$, i.e. 20 wave lengths away.

If we ignore the oscillating factor sin, cos, and the sign and take $\frac{1}{\sqrt{1-\frac{1}{4Q^2}}} \approx 1$ in Eq. 6.19, it is a good approximation to regard the sum as maxima of the oscillating amplitude of the $V_\perp(t)$. Thus the wakefield can be written as

$$\begin{aligned} W_\perp &= W_0(e^{-\frac{t'}{2Q}} + \frac{b}{Q}\frac{1}{t'^{3/2}}) \quad \text{with} \\ b &= \sqrt{\frac{2}{\pi}}\frac{(\frac{\omega_c}{\omega_0})^{1/2}}{(1-(\frac{\omega_c}{\omega_0})^2)^{5/2}}. \end{aligned} \tag{6.20}$$

The parameter b as a function of $\frac{\omega_c}{\omega_0}$ is plotted in Fig. 6.3

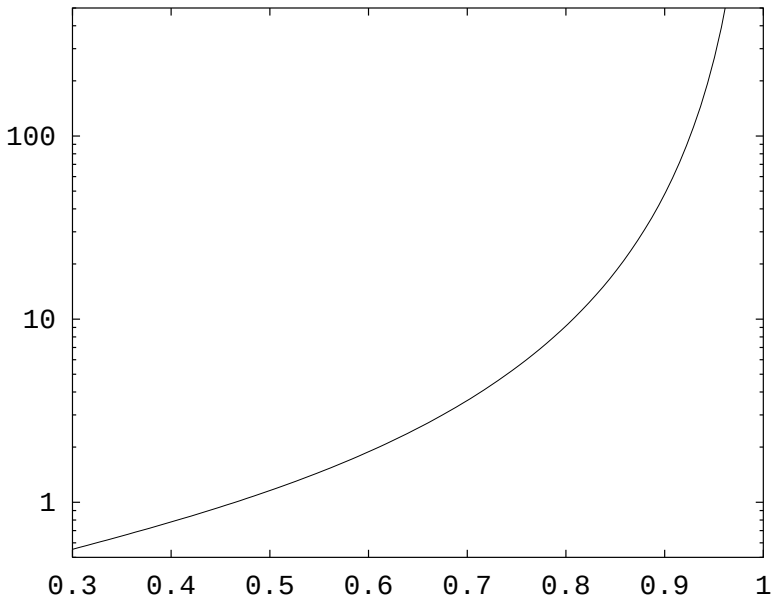

Figure 6.3: The value b as a function of $\frac{\omega_c}{\omega_0}$. The horizontal axis is $\frac{\omega_c}{\omega_0}$, and vertical axis represents b.

For a given t', the minimum value of the wakefield occurs when

$$\frac{1}{2Q} = \frac{\frac{5}{2}\log t' - \log b}{t'}, \tag{6.21}$$

Thus decreasing Q beyond this value increases the wakefield at t'. The optimum Q as a function of t' is plotted in Fig. 6.4.

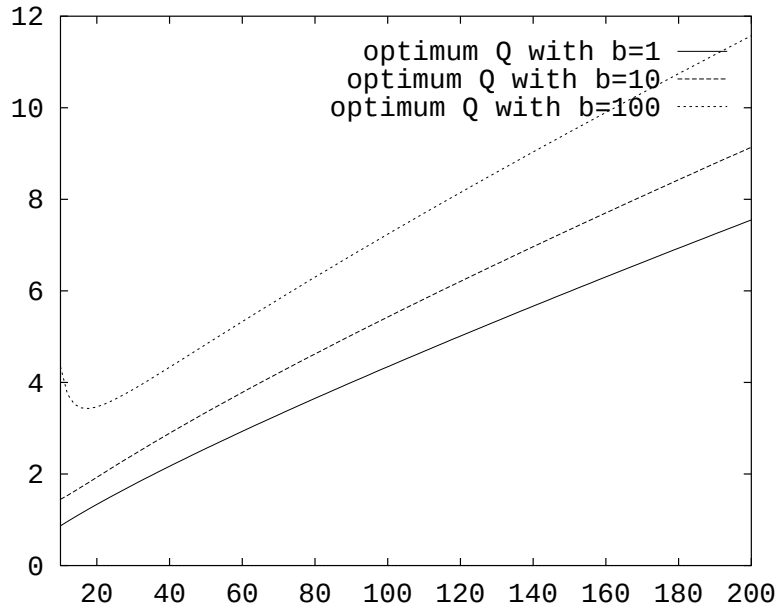

Figure 6.4: The optimum Q value as a function of distance. The three lines, from bottom to top, correspond to $b = 1, 10, 100$, respectively. The horizontal axis is $t' = \omega_c t$, and the vertical is the optimum Q value.

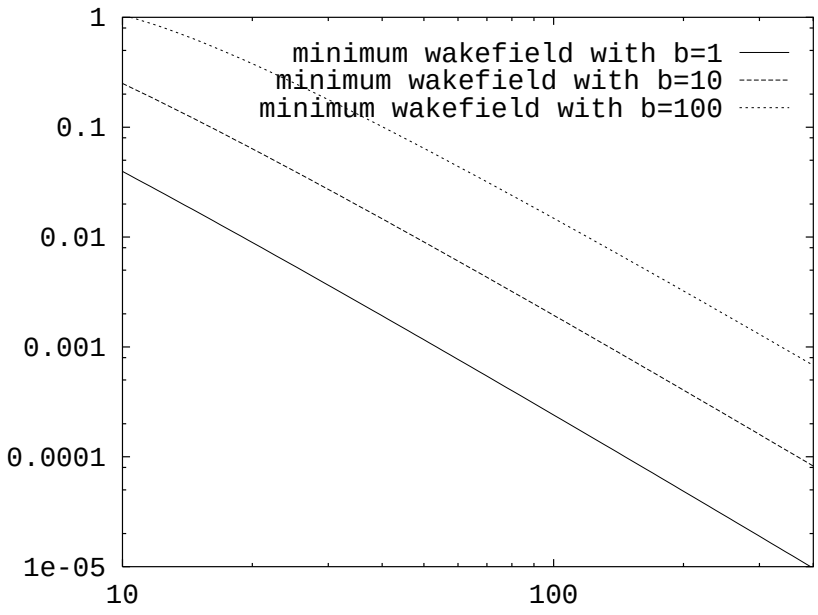

Figure 6.5: The minimum wakefield as a function of distance. The three lines, from bottom to top, correspond to $b = 1, 10, 100$, respectively. The horizontal axis is $t' = \omega_c t$. The vertical axis is the minimum wakefield achieved as a ratio to the wakefield at $t' = 0$.

Substituting Eq. 6.21 into Eq. 6.20, The value of the minimum wakefield at t'

$$W_{\perp}^{min} = W_0 t'^{-2.5}(5b\log t' + b - 2b\log b). \tag{6.22}$$

is obtained. Fig. 6.5 displays the minimum wakefield as a function of t' for a few values of b.

6.2 Numerical Comparison

We have made a few MAFIA simulations on different geometries in Chapter 4 where we have calculated the persistent wake amplitude and the damped wake amplitude. The ratios of the persistent wake amplitude to the damped wake amplitude for these cavity waveguide systems are compared with those predicted by Eq. 6.19 to explore the universality of the circuit model.

	MAFIA result	Theory
$Q = 3.94$, $\frac{\omega_c}{\omega_0} = 0.776$	2.17	2.19
$Q = 6.72$, $\frac{\omega_c}{\omega_0} = 0.776$	1.17	1.28
$Q = 7.34$, $\frac{\omega_c}{\omega_0} = 0.705$	0.587	0.659
$Q = 12.0$, $\frac{\omega_c}{\omega_0} = 0.731$	0.351	0.503

Table 6.1: Comparison of the circuit model and MAFIA simulation on persistent wake amplitude. The ratios of the persistent wake amplitude to the damped wake amplitude for several MAFIA simulated configurations are compared to those computed from the circuit model.

The MAFIA results and the circuit model agree very well considering how simple the circuit model is. The discrepancy at high Q value is attributed to the non resonant factors.

6.3 Cavity and Waveguide Detuning

For a single damped cavity, Eq. 6.22 presents the limit of the transverse wakefield. In the case of a multi-cell structure, there are more things one can do.

Notice that the persistent wakefield oscillates at the waveguide cutoff frequency. We could change the width of the waveguide from cavity to cavity. As a result, the persistent wakes of individual cavities do not oscillate coherently; the cancelation leaves the net effect of the total persistent wake very small. It is a natural extension of the cavity detuning scheme [20].

In an optimum-damped system, the dipole frequency (ω_0) has to be detuned in proportional to that of the waveguide cutoff, i.e. $\frac{\omega_c}{\omega_0}$ of each cavity is the same. In a N cell structure, detuning usually results in a wakefield which is $\frac{1}{N}$ of that of a single cell.

Taking the SLAC proposed X-band NLC for example, with dipole frequency at 15 GHz, the waveguide cutoff can be chosen at 13 GHz (it has to be greater than 11.424 GHz to keep the fundamental mode undamped.). At $t' = 40\pi$, the minimum wakefield of a single cell is 6.0×10^{-4} times that of an undamped cavity. With detuning in a 100-cell structure, the achievable transverse wakefield is down to a few parts in a million.

Chapter 7

Multi-bunch Transverse Instability

Since the discovery of the cumulative beam break-up instability at the SLAC linac by Neal and Panofsky [31] in 1966, it has been a subject of many research works. The first theoretical studies were carried out in the following few years by Wilson in 1967 [32], Panofsky and Bander in 1968 [33], and Helm and Loew [34] in 1970. Subsequent works have treated different aspects of the instability: Neil, Hall, and Cooper [35] have studied the dynamics of a single intense bunch passing N number of identical accelerator units, and with the help of the Laplace transform, exponential growth with N at the asymptotic limit is derived. Chao, Ritcher and Yao [36] used a perturbation method to find the emittance growth of a single long bunch both in the case of a coasting beam and an accelerated beam. Even though the *very long* bunch limit bears some resemblance to multi-bunch BBU, these works are primarily in the region of single bunch BBU. Gluckstern, Cooper and Channel [37] were the first to treat multi point-like charged bunches. They made use of the discrete Laplace transform and derived the asymptotic limit as the bunch number goes to infinity. The discussion is limited to the transverse wakefield of a single exponentially damped cavity mode. The subsequent work by Gluckstern, Neri, and Cooper [38] [39] dealt with the effect of randomly fluctuating parameters and smoothly varying parameters. Yokoya [40] solved the BBU equation under an arbitrary wakefield and evaluated the effect of cavity detuning, misaligned cavity, and misaligned focusing elements.

Decker and Wang [41] did a similar work. Thompson and Ruth [23] have treated the multi-bunch BBU in a very high energy linac in the time domain, where putting the bunches at the zero wakefield location is discussed.

In order to assess the effects on beam dynamics from the persistent wakefield, which decays as $t^{-\frac{3}{2}}$, we have analytically solved the multi-bunch BBU subject to an arbitrary form of wakefield in the continuous focusing approximation. The asymptotic limits of linac length going to infinity is then evaluated by a saddle point method. We start with the simple daisy chain model to illustrate the method.

7.1 Analytical Solution of the Daisy Chain Model

In section 1.3, we have solved the daisy chain model with an approximation to illustrate its rapid growing transverse offset with distance and to exhibit the dependence upon bunch number. We return to it here to obtain the solution without approximation. With proper scaling, the daisy chain model can be written as a recursive differential equation:

$$\frac{d^2}{du^2}x_n + x_n = \lambda x_{n-1}. \tag{7.1}$$

Comparing with Eq. 1.4, we see immediately that

$$u = ks, \qquad \lambda = \frac{Ne^2 W_\perp(l)}{k^2 E}. \tag{7.2}$$

Here u has the meaning of betatron phase advance along the linac, while λ is usually a small coefficient coupling the motion of the bunches. It is understood that $x_{-1} = 0$, so the equation for x_0 is included. If we multiply Eq. 7.1 by e^{-pu} and integrate from 0 to ∞,

$$-p + (p^2 + 1)\tilde{x}_n(p) = \lambda \tilde{x}_{n-1}(p) \tag{7.3}$$

follows. In Eq. 7.3, we have used the initial conditions $x_n(0) = 1$ and $x_n'(0) = 0$, which corresponds to an injection offset error in accelerator language. A $\tilde{}$ on top of a symbol denotes Laplace transform. Recursive equations can be solved by a

generating function method in a systematic way [42], which we will use later. However Eq. 7.3 is simple enough to be solved by inspection. Starting from $\tilde{x}_0 = \frac{p}{1+p^2}$, $\tilde{x}_1 = \frac{p}{1+p^2}(1+\frac{\lambda}{1+p^2})$, and $\tilde{x}_2 = \frac{p}{1+p^2}(1+\frac{\lambda}{1+p^2}+(\frac{\lambda}{1+p^2})^2)$ etc, it is straight forward to see that Eq. 7.3 is solved by the the general form

$$\tilde{x}_n = \frac{p}{1+p^2}\sum_{j=0}^{n}(\frac{\lambda}{1+p^2})^j. \tag{7.4}$$

With the inverse Laplace transform, we obtain

$$\begin{aligned} x_n(u) &= \frac{1}{2\pi i}\int \tilde{x}_n e^{pu}dp \\ &= \frac{1}{2\pi i}\int \frac{p}{1+p^2}\sum_{j=0}^{n}(\frac{\lambda}{1+p^2})^j e^{pu}dp \\ &= \frac{d}{du}\frac{1}{2\pi i}\int \frac{1}{1+p^2}\sum_{j=0}^{n}(\frac{\lambda}{1+p^2})^j e^{pu}dp \\ &= \frac{d}{du}\sum_{j=0}^{n}\frac{1}{2\pi i}\int \lambda^j \frac{e^{pu}}{(1+p^2)^{j+1}}dp. \end{aligned} \tag{7.5}$$

The path of integration is understood to be taken along a line parallel to the imaginary axis with positive real part. Because of the factor e^{pu}, the integration path can be closed from the left. The contour integral has contributions only from the two $j+1$th order poles at i and $-i$. Therefore Eq. 7.5 becomes

$$x_n(u) = \frac{d}{du}\sum_{k=0}^{n}\frac{\lambda^k}{k!}\{(\frac{e^{pu}}{(p+i)^{k+1}})^{(k)}\mid_{p=i} + (\frac{e^{pu}}{(p-i)^{k+1}})^{(k)}\mid_{p=-i}\}, \tag{7.6}$$

where $^{(k)}$ is the kth derivative. Carrying out the derivatives according to the binomial formula $(fg)^{(k)} = \sum_{j=0}^{k}\frac{k!}{j!(k-j)!}f^{(j)}g^{(k-j)}$, we have

$$x_n(u) = \sum_{k=0}^{n}\frac{\lambda^k}{k!}\sum_{j=0}^{k}\frac{(2k-j)!}{(k-j)!\ j!\ 2^{2k-j}}[ju^{j-1}\sin(u-j\frac{\pi}{2}) + u^j\cos(u-j\frac{\pi}{2})]. \tag{7.7}$$

In order to simplify the expression, it is necessary to switch the order of the summation which leaves

$$\begin{aligned} x_n(u) &= \sum_{j=0}^{n}\sum_{k=j}^{n}\frac{\lambda^k}{k!}\frac{(2k-j)!}{(k-j)!\ j!\ 2^{2k-j}}[ju^{j-1}\sin(u-j\frac{\pi}{2}) + u^j\cos(u-j\frac{\pi}{2})] \\ &= \sum_{j=0}^{n}\frac{(\frac{\lambda}{2})^j}{j!}[ju^{j-1}\sin(u-j\frac{\pi}{2}) + u^j\cos(u-j\frac{\pi}{2})]\sum_{k=0}^{n-j}(\frac{\lambda}{4})^k\frac{(2k+j)!}{(j+k)!k!}. \end{aligned} \tag{7.8}$$

If we shift the index j in the sin term by one unit, the sin term is then combined with the cos term to give the following result:

$$x_n(u) = \sum_{j=0}^{n} \frac{(\frac{\lambda}{2}u)^j}{j!} \cos(u - j\frac{\pi}{2}) \sum_{k=0}^{n-j} (\frac{\lambda}{4})^k \frac{(2k+j)!}{(j+k)!k!} \frac{j}{2k+j}. \tag{7.9}$$

Note, that when $j = 0$ and $k = 0$, the factor $\frac{j}{2k+j} = 1$.

As a check on the algebra we have used Mathematica [44] to show the $x_n(u)$ in Eq. 7.9 satisfies Eq. 7.1 for n up to ten.

A set of typical values for the NLC parameters are [20]

Quantity	N	k	s	$W_\perp(l)$	E
Value	10^{10}	0.25 m^{-1}	6000 m	10^{15}V/C/m^2	18 GeV

In this example,

$$\lambda = 1.4 \times 10^{-3}. \tag{7.10}$$

Hence the $k = 0$ term of the Eq. 7.9 dominates, the contribution of other terms drops rapidly. To a good approximation, we are able to keep only the $k = 0$ term. Not surprisingly, Eq. 7.9 then reduces to Eq. 1.9.

$$x_n(u) = \sum_{j=0}^{n} \frac{(\lambda\frac{u}{2})^j}{j!} \cos\,(u - j\frac{pi}{2}) = \Re \sum_{j=0}^{n} \frac{(-i\lambda\frac{u}{2})^j}{j!} e^{iu}. \tag{7.11}$$

We have discussed the case of non accelerating beams; due to gradual acceleration, the "effective" length of the linac is given by [23]

$$u_{eff} \approx 2\sqrt{\frac{E_i}{E_f}}u, \tag{7.12}$$

where $E_i = 18$ GeV is the initial linac energy, $E_f = 250$ GeV is the final energy. It is assumed that k scaled as $-\frac{1}{2}$ power, and hence that λ is energy independent. With

$$u_{eff} = 0.8 \times 10^3, \tag{7.13}$$

Eq. 7.11 gives a moderate growth of $\mid 1 + 0.56i \mid -1 = 15\%$ for x_1.

7.2 More General Model

In the case of a slowly decaying wakefield, where the effect of all the preceding bunches other than the closest cannot be ignored, a more general approach has to replace the daisy chain model[1]. As will be seen, it again amounts to the solving of recursive equations.

7.2.1 General Solution of x_n

With proper scaling, this problem can be formulated by a series of recursive equations as follows [43]:

$$\frac{d^2}{du^2}x_n + x_n = \lambda \sum_{m=1}^{n} x_{n-m}h(m), \tag{7.14}$$

where u and λ are defined in Eq. 7.2, therefore $h(1) = 1$. The equation assumes smooth focusing and no acceleration as before. Bear in mind that λ is usually small as shown in Eq. 7.10 and $x_n(u)$ is usually evaluated at large u as shown in Eq. 7.13. Taking the Laplace transform in u, we have

$$-p\delta_{0,n} + (p^2+1)\tilde{x}_n(p) = \lambda \sum_{m=1}^{n} \tilde{x}_{n-m}(p)h(m). \tag{7.15}$$

We assume $x'(0) = 0$ and $x_n(0) = \delta_{0,n}$, and will show later that this assumption does not affect the result by much. Multiplying Eq. 7.15 by y^n and summing from 0 to ∞, we obtain

$$-p + (p^2+1)G(y,p) = \lambda f(y)G(y,p) \tag{7.16}$$

$$\text{with} \qquad f(y) \equiv \sum_{m=1}^{\infty} y^m h(m) \tag{7.17}$$

$$G(y,p) \equiv \sum_{m=0}^{\infty} y^m \tilde{x}_m(p). \tag{7.18}$$

The generating function G is solved from Eq. 7.16 to give

$$G(y,p) = \frac{p}{p^2 + 1 - \lambda f(y)}. \tag{7.19}$$

[1] this section actually shows that daisy chain model is surprisingly good for approximating many different wakefields.

The inverse Laplace transform gives

$$G(y,u) = \cos(u\sqrt{1-\lambda f(y)}). \tag{7.20}$$

To find $x_n(u)$, we need to extract the coefficient of the y^n term in $G(y,u)$ (see Eq. 7.18), which can be obtained by integrating $\frac{G(y,u)}{y^{n+1}}$ along a contour in the y plane around the origin and dividing the result by $2\pi i$ (from Cauchy's theorem). We thus have

$$x_n(u) = \frac{1}{2\pi i}\oint_c \frac{\cos(u\sqrt{1-\lambda f(y)})}{y^{n+1}}dy. \tag{7.21}$$

From the two power expansions

$$\cos(u\sqrt{1-\lambda f(y)}) = \sum_{n=0}^{\infty} x_n(u)y^n \quad and \quad e^{iu\sqrt{1-\lambda f(y)}} = \sum_{n=0}^{\infty} z_n(u)y^n,$$

we see that equation

$$x_n(u) = \Re(z_n(u)) \tag{7.22}$$

has to hold by equating powers of y.

From now on, we will use the expression for $x_n(u)$ in the following form.

$$x_n(u) = \frac{1}{2\pi i}\oint_c \frac{e^{iu\sqrt{1-\lambda f(y)}}}{y^{n+1}}dy. \tag{7.23}$$

It is understood that we only take the real part of the right hand side of Eq. 7.23. Alternatively, we could take its magnitude as the envelope of $x_n(u)$.

Saddle Point Method

Our primary interest is in the behavior of $x_n(u)$ at large u, so that we know whether the beam is unstable and how fast the instability grows. A powerful method in dealing with just this type of integral is the saddle-point method, also called the method of steepest descent, which we will briefly explain in the following. Consider a typical integral of the form

$$\int_C e^{i\phi(y)}dy, \tag{7.24}$$

where $\phi(y)$ varies rapidly with y due to a large factor (in our case, u.). The rapid oscillating integrand yields a substantial contribution only at the saddle point y_s defined by

$$\frac{d\phi(y)}{dy} \mid_{y_s} = 0. \tag{7.25}$$

By analytically changing the path C through y_s, the integral in Eq. 7.24 can be written as[2]

$$\int_{C'} e^{i\phi(y_s)+\frac{i}{2}(y-y_s)^2\phi''(y_s)+O((y-y_s)^3)}dy. \tag{7.26}$$

The orientation of path C' is chosen such that the integrand has the steepest descent (hence the name.) away from the saddle point. Then we may write the integral as

$$e^{i\phi(y_s)} \int e^{-\frac{|\phi''(y_s)|}{2}x^2}dx = \sqrt{\frac{2\pi}{\mid \phi''(y_s) \mid}}e^{i\phi(y_s)}, \tag{7.27}$$

where we have used the fact that $\mid \phi''(y_s) \mid$ is large.

Asymptotic Limit of x_n

For asymptotic evaluation of Eq. 7.23, we deform the contour to pass through the saddle point, which satisfies

$$\frac{d}{dy}i\phi(y) = \frac{d}{dy}(iu\sqrt{1-\lambda f(y)} - (n+1)\log y) = -\frac{iu\lambda f'(y)}{2\sqrt{1-\lambda f(y)}} - \frac{n+1}{y} = 0. \tag{7.28}$$

The solution of Eq. 7.28 for each n is substituted in $\phi(y)$, and $\Re(i\phi(y))$ is the exponential growth rate of x_n. In order to set an upper bound of BBU, we take the maximum of those rates as the upper limit of BBU growth, which satisfies

$$\frac{d}{dn}\Re(iu\sqrt{1-\lambda f(y)} - (n+1)\log y) = 0. \tag{7.29}$$

It is understood that y is a function of n implicitly defined by Eq. 7.28. Utilizing this fact, we can further write Eq. 7.29 in the form of

$$\frac{dy}{dn}\frac{d}{dy}\Re(iu\sqrt{1-\lambda f(y)} - (n+1)\log y) - \Re\log y = 0. \tag{7.30}$$

[2] We have assumed that no poles are encountered when moving the integration path, otherwise a pole contribution will be added.

The first term vanishes because of the saddle-point condition. The equation then reduces to

$$y = e^{i\theta}. \tag{7.31}$$

We are able to calculate θ by invoking the saddle-point condition Eq. 7.28. Eq. 7.28 becomes

$$\Re(yf') = \sum_{m=1}^{\infty} mh(m)\cos(m\theta) = 0 \tag{7.32}$$

if we assume $\sqrt{1-\lambda f(y)} \approx 1$. Solution of Eq. 7.32 determines the value of θ. Substituting $y = e^{i\theta}$ into the expression of $i\phi(y)$, we obtain the maximum growth exponent

$$\gamma = \Re(i\phi(y)) = \Im(-u\sqrt{1-\lambda f(y)}) \approx \frac{\lambda u}{2}\Im f(e^{i\theta}) = \frac{\lambda u}{2}\sum_{m=1}^{\infty}\sin(m\theta)h(m). \tag{7.33}$$

The maximum growth occurs at bunch number N_{max}, where N_{max} satisfies Eq. 7.28, which we rewrite as

$$\begin{aligned} N_{max} &= -\frac{iu\lambda y f'(y)}{2\sqrt{1-\lambda f(y)}} - 1 \\ &\approx \frac{\lambda u}{2}\Im(yf'(y)) \\ &= \frac{\lambda u}{2}\sum_{m=1}^{\infty} mh(m)\sin(m\theta). \end{aligned} \tag{7.34}$$

It is not surprising then to see Eqs. 7.32 and 7.33. In fact, Eq. 7.32 is the maximum condition of Eq. 7.33 with respect to the variable θ.

A few simple wakefield models have been worked out explicitly. The results are displayed in Fig. 7.1. Details are given in Appendix C.

$h(m)$	θ	$\gamma/\frac{\lambda u}{2}$	$N_{max}/\frac{\lambda u}{2}$
$\delta_{m,1}$	$\frac{\pi}{2}$	1	1
$e^{-\beta(m-1)}$	$\arcsin(\tanh\beta)$	$\frac{1}{1-e^{-2\beta}}$	$\frac{\coth\beta}{1-e^{-2\beta}}$
$m^{-\frac{3}{2}}$	0.74377	1.07736	1.29804
$\lim_{\epsilon\to 0+} m^{-1-\epsilon}$	$\pi\epsilon$	$\frac{\pi}{2}[1+\epsilon\log\epsilon+(\log\pi+\gamma_e-1)\epsilon]$	$\frac{1}{\pi}\frac{1}{\epsilon}$

Table 7.1: Solutions of the maximum beam growth vs wakefield decay laws. The γ_e is Euler's constant, which is approximately 0.5772156649.

7.2.2 Uniform Initial Offsets

In the case where all bunches start with a uniform offset, i.e. $x_n(0) = 1$ and $x'_n(0) = 0$, Eq. 7.15 and 7.16 become

$$-p + (p^2+1)\tilde{x}_n(p) = \lambda \sum_{m=1}^{n-1} \tilde{x}_{n-m}(p)h(m) \tag{7.35}$$

$$-\frac{p}{1-y} + (p^2+1)G(y,p) = \lambda f(y)G(y,p) \tag{7.36}$$

where $f(y)$ and $G(y,p)$ are defined in Eq. 7.17 and 7.18, respectively. Solve for $G(y,p)$ to get

$$G(y,p) = \frac{1}{1-y}\frac{p}{p^2+1-\lambda f(y)}. \tag{7.37}$$

Therefore

$$G(y,u) = \frac{\cos(u\sqrt{1-\lambda f(y)})}{1-y} \tag{7.38}$$

is obtained by inverse Laplace transform.

Carrying through the same contour integral to extract the coefficient of the y^n term, we have

$$\begin{aligned} x_n(u) &= \frac{1}{2\pi i}\oint_c \frac{\cos(u\sqrt{1-\lambda f(y)})}{(1-y)y^{n+1}}dy \\ &\sim \frac{1}{2\pi i}\oint_c \frac{e^{iu\sqrt{1-\lambda f(y)}}}{(1-y)y^{n+1}}dy. \end{aligned} \tag{7.39}$$

The $\sim$ is understood as taking the real part of the right hand side. Note the extra factor $\frac{1}{1-y}$ in the integrand compared with Eq. 7.23. The corresponding saddle-point condition is modified to

$$\begin{aligned} \frac{d}{dy}i\phi(y) &= \frac{d}{dy}(iu\sqrt{1-\lambda f(y)} - (n+1)\log y - \log(1-y)) \\ &= -\frac{iu\lambda f'(y)}{2\sqrt{1-\lambda f(y)}} - \frac{n+1}{y} + \frac{1}{1-y} = 0. \end{aligned} \tag{7.40}$$

The y value for maximum growth rate then satisfies

$$\frac{d}{dn}\Re(it\sqrt{1-\lambda f(y)} - (n+1)\log y - \log(1-y)) = 0. \tag{7.41}$$

Again, y is regarded as a function of n defined by the saddle-point condition Eq. 7.40. Rewriting Eq. 7.41 in the form

$$0 = \frac{dy}{dn}\frac{d}{dy}\Re(iu\sqrt{1-\lambda f(y)} - (n+1)\log y - \log(1-y)) - \Re\log y = -\Re\log y, \quad (7.42)$$

we find that the same maximum growth condition holds:

$$y = e^{i\theta}. \quad (7.43)$$

We can calculate θ the same way as before by invoking saddle-point Eq. 7.40. With the approximation, $\sqrt{1-\lambda f(y)} \approx 1$, Eq. 7.40 becomes

$$\Re(yf' - \frac{2}{i\lambda u}\frac{y}{1-y}) = \sum_{m=1}^{\infty} mh(m)\cos(m\theta) + \frac{1}{\lambda u}\frac{\sin\theta}{1-\cos\theta} = 0. \quad (7.44)$$

The second term in Eq. 7.44 is negligible when $u \to \infty$, and Eq. 7.44 becomes Eq. 7.32.

The maximum growth rate then becomes

$$\gamma = \frac{\lambda u}{2}\Im f(e^{i\theta}) + \Re\log(1-e^{i\theta}) = \frac{\lambda u}{2}\sum_{m=1}^{\infty}\sin(m\theta)h(m) + \Re\log(1-e^{i\theta}). \quad (7.45)$$

By the same token, Eq. 7.45 approaches Eq. 7.33 at large u limit.

From Eq. 7.40 the maximum growth occurred at bunch number

$$N_{max} = \frac{\lambda u}{2}\Im(e^{i\theta}f'(e^{i\theta})) + \Re(\frac{e^{i\theta}}{1-e^{i\theta}}) - 1 = \frac{\lambda u}{2}\sum_{m=1}^{\infty} mh(m)sin(m\theta) - \frac{3}{2}. \quad (7.46)$$

which goes to Eq. 7.34 at large u limit.

It is interesting to note that all of the wakefields above produce a growth rate with a maximum in N. It is a direct consequence of the fact that $\sum_{m=1}^{\infty} h(m)$ is finite. This observation has an interesting implication in accelerator design: If the wakefield decays faster than $\frac{1}{t}$, the luminosity can be indefinitely increased by adding more and more bunches to the train (we ignore the technical problems of beam loading etc.). In other words, if the bunch charge is limited so that the growth rate at $n = N_{max}$ is acceptable, then the luminosity can be increased indefinitely by increasing n beyond N_{max}. Numerical simulations of bunch displacements caused by wakefields decaying with different power laws are shown in Fig. 7.1 to illustrate this assertion.

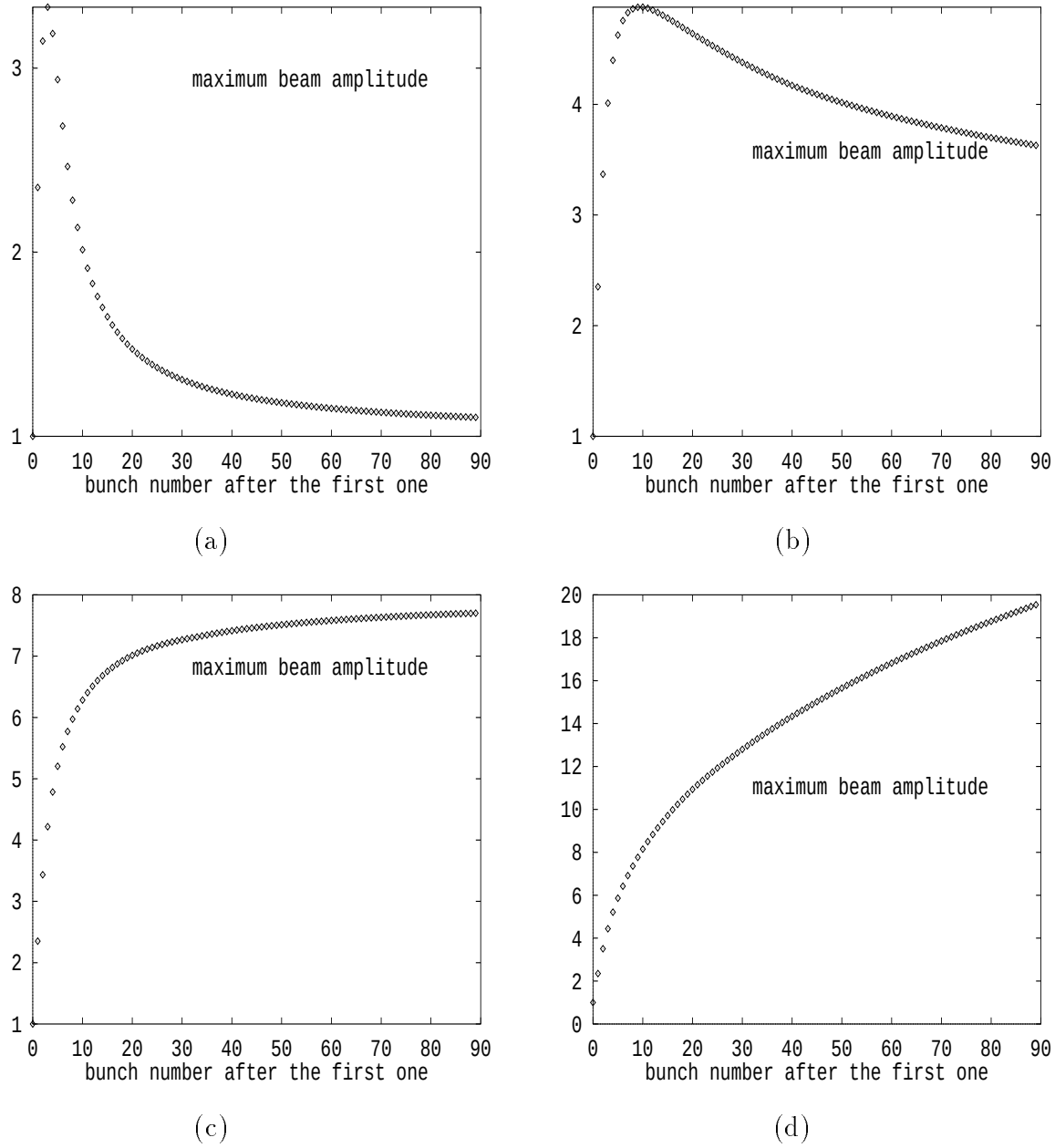

Figure 7.1: Simulations of BBU for wakefields with different decay laws, all with $\frac{\lambda u}{2} = 2.145306$ and with initial offset $x_n(0) = 1$. The maximum beam offset is plotted against the bunch number. (a): $h(m) = m^{-1.5}$, (b): $h(m) = m^{-1.1}$ (c): $h(m) = m^{-1}$ (d) $h(m) = m^{-0.9}$.

7.2.3 Oscillating Wakefield $\propto \cos(m\theta_0)$

The same analysis allows one to deal with an oscillating wakefield, i.e. $h(m) \propto \cos(m\theta_0)$. In fact, we have dealt with the special case of $\theta_0 = 0$ in the earlier sections. If we assume a single damped mode to represent the transverse wakefield, then

$$h(m) = e^{-\beta(m-1)} \cos(m\theta_0), \tag{7.47}$$

where θ_0 is the bunch to bunch wakefield phase advance (modulo 2π). According to Eq. 7.33, the maximum growth rate

$$\begin{aligned} \gamma &= \frac{\lambda u}{2} \sum_{m=1}^{\infty} \sin(m\theta) e^{-\beta(m-1)} \cos(m\theta_0) \\ &= \frac{\lambda u}{2} \frac{1}{2} [\frac{\sin(\theta+\theta_0)}{1+e^{-2\beta}-2e^{-\beta}\cos(\theta+\theta_0)} + \frac{\sin(\theta-\theta_0)}{1+e^{-2\beta}-2e^{-\beta}\cos(\theta-\theta_0)}] \end{aligned} \tag{7.48}$$

and θ satisfies (from Eq. 7.32)

$$\begin{aligned} & \cosh\beta \cos\theta \cos\theta_0 (\cosh^2\beta + 1 + \cos^2\theta + \cos^2\theta_0) \\ + \; & (1 - 2\cosh^2\beta)(\cos^2\theta + \cos^2\theta_0) - 2\cos^2\theta\cos^2\theta_0 + \cosh^2\beta - 1 = 0. \end{aligned} \tag{7.49}$$

Numerical solutions of the above equation are plotted for a few β values in Fig. 7.2. As can be seen from the plots, θ correlates with θ_0 strongly, especially for a slowly decaying wakefield (low β). The oscillation introduced by $\cos(m\theta_0)$ in $h(m)$ is neutralized by $\sin(m\theta)$ in the Eq. 7.48. Therefore, the maximum growth rate does not change drastically due to the introduction of wakefield oscillation. Physically, what happens is that the trailing bunches find their way in the betatron phase, so that their betatron phases lag by an appropriate amount to neutralize the wakefield phase from the proceeding bunch. The wake force still adds up from all the proceeding bunches. That is why the BBU growing trend does not differ much between oscillating and non-oscillating cases.

The following figure plot the maximum growth rate γ as a function of θ_0,

The maximum growth happens at bunch number

$$N_{max} = \frac{\lambda u}{2} \sum_{m=1}^{\infty} m h(m) \sin(m\theta) = -\frac{\lambda u}{2} \Re(\frac{d}{d\theta} f(e^{i\theta}))$$

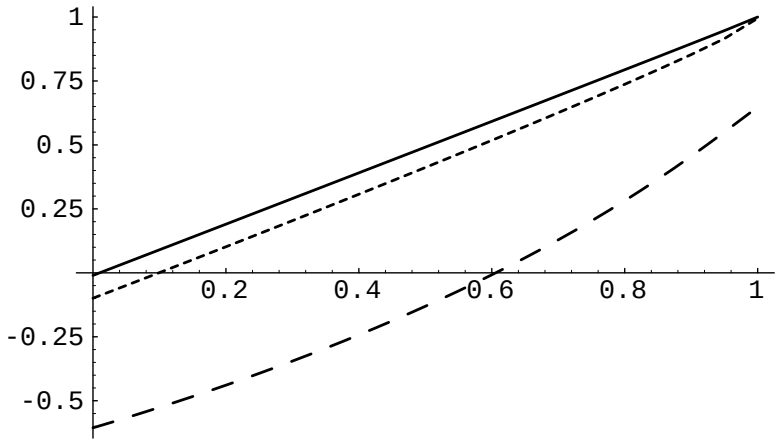

Figure 7.2: Solutions of θ as a function of θ_0. The three lines(solid, short dashed, and long dashed), from top to bottom, correspond to $\beta = 0.01$, 0.1, 1, respectively. The vertical axis is $\cos\theta$, the horizontal axis represents $\cos\theta_0$.

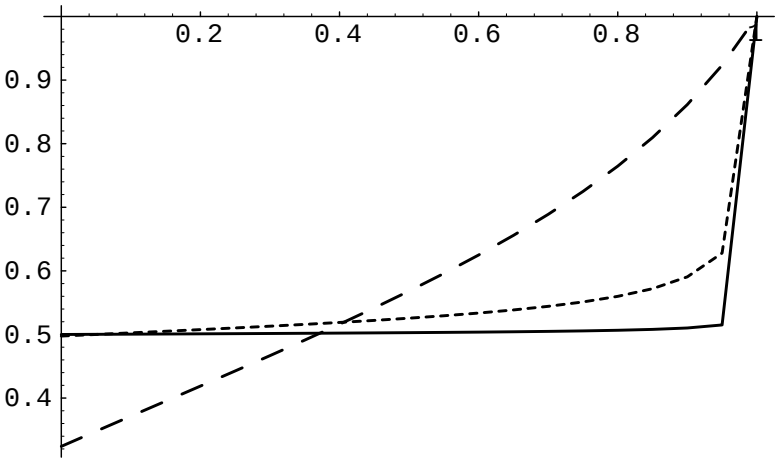

Figure 7.3: The maximum growth rate γ as a function of θ_0. The solid line, short dashed line, and long dashed line correspond to $\beta = 0.01$, 0.1, 1, respectively. The vertical axis is $\frac{\gamma(\theta_0)}{\gamma(0)}$, the horizontal axis represents $\cos\theta_0$.

$$= \frac{\lambda u}{4}\left[\frac{\sin(\theta+\theta_0)(1-e^{-2\beta})}{(1+e^{-2\beta}-2e^{-\beta}\cos(\theta+\theta_0))^2}+\frac{\sin(\theta-\theta_0)(1-e^{-2\beta})}{(1+e^{-2\beta}-2e^{-\beta}\cos(\theta-\theta_0))^2}\right] \quad (7.50)$$

Equation 7.50 is plotted as a function of θ_0 for a few value of β in Fig. 7.4

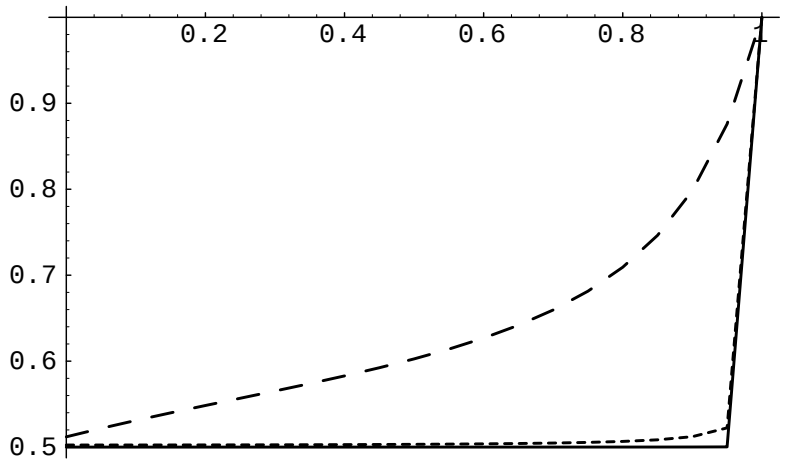

Figure 7.4: The bunch number N_{max} as a function of θ_0. The solid line, short dashed line, and long dashed line correspond to $\beta = 0.01$, 0.1, 1, respectively. The vertical axis is $\frac{N_{max}(\theta_0)}{N_{max}(0)}$, the horizontal axis represents $\cos\theta_0$.

7.2.4 Oscillating Wakefield $\propto \sin(m\theta_0)$

The previous section described the beam dynamics of the wakefield which oscillates proportional to $\cos(m\theta)$ for the sake of comparison between the oscillating and non-oscillating cases. In the real accelerating structure, the transverse wakefield is proportional to $\sin(m\theta)$ while the longitudinal wakefield is proportional to $\cos(m\theta)$. We have, of course, assumed point-like charge bunches. Hence, it is important to discuss the wakefield

$$h(m) = e^{-\beta(m-1)}\sin(m\theta_0), \quad (7.51)$$

where θ_0 is again the bunch to bunch phase advance. Similar to Eq. 7.48, the maximum growth rate satisfies

$$\begin{aligned}\gamma &= \frac{\lambda u}{2}\sum_{m=1}^{\infty}\sin(m\theta)e^{-\beta(m-1)}\sin(m\theta_0) \\ &= \frac{\lambda u}{2}\frac{1}{2}\left[\frac{e^{-\beta}-\cos(\theta+\theta_0)}{1+e^{-2\beta}-2e^{-\beta}\cos(\theta+\theta_0)}-\frac{e^{-\beta}-\cos(\theta-\theta_0)}{1+e^{-2\beta}-2e^{-\beta}\cos(\theta-\theta_0)}\right] \quad (7.52)\end{aligned}$$

where θ satisfies (from Eq. 7.32)

$$-(1+5e^{2\beta}+e^{4\beta})\cos\theta + e^{2\beta}\cos 3\theta - e^{2\beta}\cos(\theta-2\theta_0)$$
$$+ \quad 4e^{\beta}(1+e^{\beta})\cos\theta_0 - e^{2\beta}\cos(\theta+2\theta_0) = 0. \tag{7.53}$$

Numerical solutions of Eq. 7.53 are plotted in Fig. 7.5.

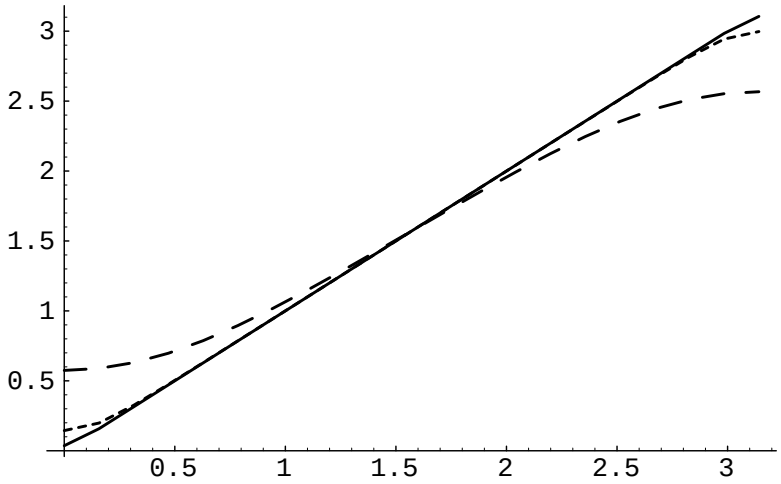

Figure 7.5: Solutions of θ as a function of θ_0. The three lines(solid, short dashed, and long dashed), correspond to $\beta = 0.0625$, 0.25, and 1, respectively. The vertical axis is θ, the horizontal axis represents θ_0.

The maximum growth rate is also plotted as a function of θ_0 for several β values in Fig. 7.6.

The bunch number of the maximum beam growth N_{max} satisfies

$$N_{max} = \frac{\lambda u}{2}\sum_{m=1}^{\infty} mh(m)\sin(m\theta) = -\frac{\lambda u}{2}\Re(\frac{d}{d\theta}f(e^{i\theta}))$$
$$= \quad -\frac{\lambda u}{4}[\frac{\cos(\theta+\theta_0)(1+e^{-2\beta})-2e^{-\beta}}{(1+e^{-2\beta}-2e^{-\beta}\cos(\theta+\theta_0))^2} - \frac{\cos(\theta-\theta_0)(1+e^{-2\beta})-2e^{-\beta}}{(1+e^{-2\beta}-2e^{-\beta}\cos(\theta-\theta_0))^2}] \tag{7.54}$$

It is shown in Fig. 7.7

It is seen from Figs. 7.6 and 7.7 that $\gamma(0) = N_{max}(0) = \gamma(\pi) = N_{max}(\pi) = 0$ because there is no wakefield at the location of the bunches if $\theta_0 = 0, \pi$. These locations are referred as wake zero crossings. Thompson and Ruth [23] have discussed the application of putting the bunches near wake zero crossing. It is however, not practical if there is more than one mode present. We observe that in between 0 and

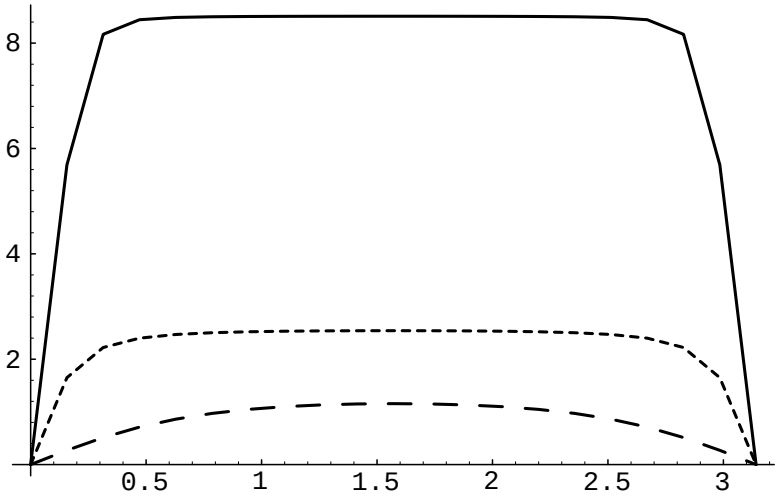

Figure 7.6: The maximum growth rate γ as a function of θ_0. The solid line, short dashed line, and long dashed line correspond to $\beta = 0.0625$, 0.25, and 1, respectively. The vertical axis is $\gamma(\theta_0)$, the horizontal axis represents θ_0.

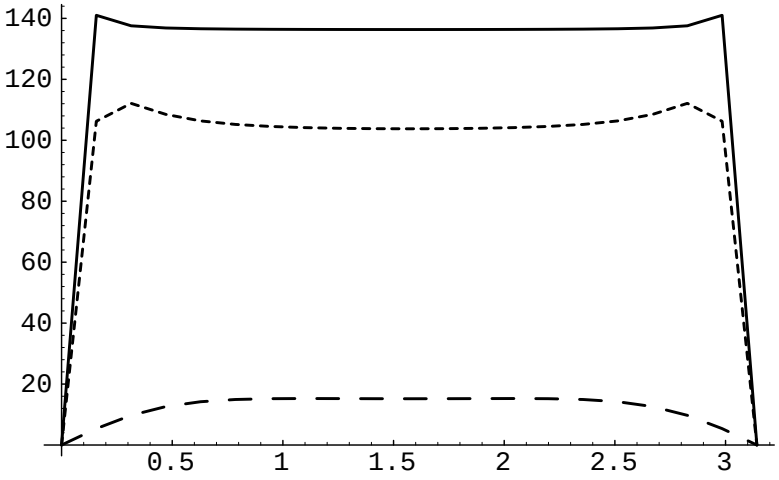

Figure 7.7: The bunch number N_{max} as a function of θ_0. The solid line, short dashed line, and long dashed line correspond to $\beta = 0.0625$, 0.25, 1, respectively. The vertical axis is $N_{max}(\theta_0)$. The short and long dashed line has been multiplied by a factor of 10 in the vertical direction in order to shown all the curve on the same scale. the horizontal axis represents θ_0.

π, the point $\theta_0 = \frac{\pi}{2}$ gives a reasonable estimation of γ and N_{max} for the whole range. The result

$$\theta(\frac{\pi}{2}) = \frac{\pi}{2} \tag{7.55}$$

is easily verified from Eq. 7.53, and

$$\gamma(\frac{\pi}{2}) = \frac{\lambda u}{2}\frac{1}{1-e^{-2\beta}} \tag{7.56}$$

is derived from Eq. 7.52. In addition,

$$N_{max}(\frac{\pi}{2}) = \frac{\lambda u}{2}\frac{1+e^{-2\beta}}{(1-e^{-2\beta})^2} = \frac{\lambda u}{2}\frac{\coth\beta}{1-e^{-2\beta}} \tag{7.57}$$

follows from Eq. 7.54.

It is interesting to note that Eqs. 7.56 and 7.57 are the same as the result for the wakefield $h(m) = e^{-\beta(m-1)}$ outlined in Table 7.1.

7.3 Conclusion

With a smooth focusing approximation and no acceleration, we have solved the cumulative BBU analytically to quantify the effects of various wakefield decay forms on the BBU growth trend in the limit of $u \to \infty$: With a field decaying faster than $\frac{1}{t}$, the BBU is qualitatively similar to the daisy chain model, which has a maximum BBU growth rate. The significance of this result is that adding more bunches to the train does not worsen the beam quality provided the train is already longer than N_{max}, the location of maximum beam growth.

In practical designs, $\frac{\lambda u}{2}$ is seldom bigger than unity in order to preserve the beam quality, then the adiabatic damping due to acceleration, discrete focusing, and the detailed form of the wakefield play moderate and complicated roles. Also the effect of structure misalignment becomes significant. Therefore this work is not a substitute for detailed particle tracking, rather it gives a qualitative insight into the effects of wakefields.

Appendix A

Microwave Theory

A.1 Waveguide Theory

The source free Maxwell's Equations are

$$\left.\begin{array}{rcl} \nabla \times \vec{E} & = & -\frac{1}{c}\frac{\partial \vec{B}}{\partial t} \\ \nabla \cdot \vec{D} & = & 0 \\ \nabla \times \vec{H} & = & \frac{1}{c}\frac{\partial \vec{D}}{\partial t} \\ \nabla \cdot \vec{B} & = & 0 \end{array}\right\}. \tag{A.1}$$

It follows that both $\vec{E}$ and $\vec{H}$ satisfy

$$(\nabla^2 + \mu\epsilon\frac{\partial^2}{\partial t^2}) \left\{ \begin{array}{c} \vec{E} \\ \vec{H} \end{array} \right\} = 0. \tag{A.2}$$

Without loss of generality, we assume that the waveguide is oriented in the z direction. Because of the cylindrical geometry of the waveguide, it is useful to single out the spatial variation of the field in the z direction and also assume sinusoidal time dependence $e^{-i\omega t}$.

$$\left.\begin{array}{c} \vec{E}(x,y,z,t) \\ \vec{H}(x,y,z,t) \end{array}\right\} = \left\{ \begin{array}{l} \vec{E}(x,y)e^{ikz-i\omega t} \\ \vec{H}(x,y)e^{ikz-i\omega t} \end{array} \right. \tag{A.3}$$

The transverse coordinate dependence satisfies:

$$(\nabla_\perp^2 + k_\perp^2) \left\{ \begin{array}{c} \vec{E} \\ \vec{H} \end{array} \right\} = 0, \tag{A.4}$$

where $\nabla_\perp^2$ is the transverse part of the Laplacian operator. With proper boundary conditions, a set of eigenvalues $k_\perp$ are determined with an associated set of field functions called eigenmodes. The propagation constant k satisfies

$$k = \pm\sqrt{(\frac{\omega}{c})^2 - k_\perp^2}, \tag{A.5}$$

where plus sign gives a wave propagating in positive z axis, minus sign gives the wave propagating in the opposite direction.

It is useful to separate the field into components parallel to and perpendicular to the z axis, so that

$$\vec{E} = \hat{z}E_z + \vec{E}_\perp \qquad \text{and} \qquad \vec{H} = \hat{z}H_z + \vec{H}_\perp, \tag{A.6}$$

where $\hat{z}$ is the unit vector in z direction. Maxwell's equations can be written out in terms of the longitudinal and transverse components as

$$\begin{aligned} (\vec{\nabla}_\perp + \hat{z}\frac{\partial}{\partial z}) \times (\hat{z}E_z + \vec{E}_\perp) &= \frac{i\mu\omega}{c}(\vec{H}_\perp + \hat{z}H_z), \\ -\hat{z} \times \vec{\nabla}_\perp E_z + ik\hat{z} \times \vec{E}_\perp + \vec{\nabla}_\perp \times \vec{E}_\perp &= \frac{i\mu\omega}{c}(\vec{H}_\perp + \hat{z}H_z). \end{aligned} \tag{A.7}$$

Eq. A.7 can be further split into two equations, one for the longitudinal direction, the other for the transverse direction:

$$-\hat{z} \times \vec{\nabla}_\perp E_z + ik\hat{z} \times \vec{E}_\perp = \frac{i\mu\omega}{c}\vec{H}_\perp, \tag{A.8}$$

$$\vec{\nabla}_\perp \times \vec{E}_\perp = \frac{i\mu\omega}{c}\hat{z}H_z. \tag{A.9}$$

Similarly, there is a corresponding set of equations for the curl equation of H. Notice the symmetry between the two curl equations; they are invariant under operation $E \mapsto H$, $H \mapsto -E$ and $\epsilon \leftrightarrow \mu$. From the above observation, the second set of equations is easily written as

$$-\hat{z} \times \vec{\nabla}_\perp H_z + ik\hat{z} \times \vec{H}_\perp = -\frac{i\epsilon\omega}{c}\vec{E}_\perp, \tag{A.10}$$

$$\vec{\nabla}_\perp \times \vec{H}_\perp = -\frac{i\epsilon\omega}{c}\hat{z}E_z. \tag{A.11}$$

Substituting the expression for $\vec{E}_\perp$ in Eq. A.10 into Eq. A.8, we then have

$$\vec{H}_\perp = i\frac{\omega}{ck_\perp^2}\epsilon\hat{z}\times\vec{\nabla}_\perp E_z + i\frac{k}{k_\perp^2}\vec{\nabla}_\perp H_z. \tag{A.12}$$

The same symmetry argument produces the expression for $\vec{E}_\perp$;

$$\vec{E}_\perp = -i\frac{\omega}{ck_\perp^2}\mu\hat{z}\times\vec{\nabla}_\perp H_z + i\frac{k}{k_\perp^2}\vec{\nabla}_\perp E_z. \tag{A.13}$$

It is evident from the Eqs. A.12 and A.13 that the fields are determined by the longitudinal components E_z and H_z only. The fields thus naturally divide themselves into two distinct categories:

- Transverse Magnetic (TM) waves: $H_z = 0$,

  $$\vec{E}_\perp = i\frac{k}{k_\perp^2}\vec{\nabla}_\perp E_z, \qquad \vec{H}_\perp = i\frac{\omega}{ck_\perp^2}\epsilon\hat{z}\times\vec{\nabla}_\perp E_z. \tag{A.14}$$

  Therefore the transverse magnetic and electric fields are related by

  $$\vec{H}_\perp = \frac{\omega}{ck}\epsilon\hat{z}\times\vec{E}_\perp \equiv Y\hat{z}\times\vec{E}_\perp. \tag{A.15}$$

  Now the equation looks more or less like the relation between the electric current and voltage. Accordingly, Y was called the mode admittance.

- Transverse Electric (TE) waves: $E_z = 0$,

  $$\vec{E}_\perp = -i\frac{\omega}{ck_\perp^2}\mu\hat{z}\times\vec{\nabla}_\perp H_z, \qquad \vec{H}_\perp = i\frac{k}{k_\perp^2}\vec{\nabla}_\perp H_z \qquad \text{and} \tag{A.16}$$

  $$\vec{H}_\perp = \frac{ck}{\omega\mu}\hat{z}\times\vec{E}_\perp \equiv Y\hat{z}\times\vec{E}_\perp. \tag{A.17}$$

It is useful to expand the transverse field in a waveguide in terms of the corresponding waveguide TE and TM modes:

$$\vec{E}_\perp = \sum_n e_n\vec{f}_n, \tag{A.18}$$

$$\vec{H}_\perp = \sum_n i_n\vec{g}_n, \tag{A.19}$$

where $\int\vec{f}_n\cdot\vec{f}_m dS = \int\vec{g}_n\cdot\vec{g}_m dS = \delta_{nm}$, $\int\vec{f}_n\times\vec{g}_m\cdot d\vec{S} = \delta_{nm}$ with $d\vec{S}$ points to the direction of the wave.

The e_n and i_n are conveniently called *voltage* and *current*, and the index n designates the eigenmodes (both TE and TM).

With the field expansion in Eqs. A.18 and A.19, Eqs. A.15 and A.17 can be rewritten as

$$i_n = Y_n^c e_n. \tag{A.20}$$

where Y_n^c is called characteristic admittance of the waveguide mode. Notice that the same waveguide mode propagating in opposite direction has a characteristic admittance differing by a minus sign.

A.2 S-matrix of a Microwave Junction

Voltage and current are not the only useful description of the terminal fields; another useful representation can be obtained in terms of incoming and outgoing waves. These waves may be characterized as *voltage amplitudes*, *current amplitudes* or, especially in the case of propagating modes, as *wave amplitudes* normalized to unit power. They are defined below:

$$e_q = a_q + b_q \quad , \quad i_q = Y_q^c(a_q - b_q) \quad \text{or} \tag{A.21}$$

$$i_q = a_q + b_q \quad , \quad e_q = Z_q^c(a_q - b_q) \quad \text{or} \tag{A.22}$$

$$e_q = \sqrt{Z_q^c}(a_q + b_q) \quad , \quad i_q = \sqrt{Y_q^c}(a_q - b_q). \tag{A.23}$$

In Eq. A.21, a_q is interpreted as incoming wave *voltage amplitude*, b_q as that of outgoing wave. Y_q^c is the characteristic admittance of qth mode. In Eq. A.22, a_q and b_q are that of the *current amplitudes*, and Z_q^c is the characteristic impedance of the qth mode. Similarly, a_q and b_q in Eq. A.23 are that of the *wave amplitudes*.

The scattering matrix as defined by

$$b_q = S_{qp} a_p \tag{A.24}$$

is readily derived from Eqs. A.21 and admittance matrix Y, which yields

$$Y^c(\vec{a} - \vec{b}) = \vec{i} \equiv Y\vec{e} = Y(\vec{a} + \vec{b}), \tag{A.25}$$

where matrix notation is used instead of the indices. Solving $\vec{b}$ in terms of $\vec{a}$, we have

$$\vec{b} = (Y^c + Y)^{-1}(Y^c - Y)\vec{a}. \tag{A.26}$$

Thus the scattering matrix,

$$S_v = (Y^c + Y)^{-1}(Y^c - Y). \tag{A.27}$$

This matrix is called the *voltage scattering matrix* because it relates outgoing voltage amplitudes to those of the incoming.

Similarly, the *current scattering matrix* S_i and *amplitude scattering matrix* S_a satisfy

$$S_i = (Z^c + Z)^{-1}(Z^c - Z), \quad \text{and} \tag{A.28}$$

$$S_a = (I + Y_a)^{-1}(I - Y_a) \tag{A.29}$$

where I is the unit matrix. Note here the admittance matrix Y_a is related to Y by

$$Y_a = \frac{1}{\sqrt{Y^c}} Y \frac{1}{\sqrt{Y^c}}. \tag{A.30}$$

The voltage scattering matrix, current scattering matrix and amplitude scattering matrix are related by

$$S_v = -Y^{c-1} S_i Y^c \quad \text{or} \quad S_i = -Z^{c-1} S_v Z^c. \tag{A.31}$$

$$S_a = \sqrt{Y^c} S_v \frac{1}{\sqrt{Y^c}} \tag{A.32}$$

For the sake of brevity, the subscript v and i are dropped in most cases unless we want to emphasize the difference. It is also easy to distinguish the voltage or current scattering matrix used in context by the appearance of Y's or Z's.

A.3 Concatenation of S-matrices

When microwave elements are linked together, the S-matrix of the final structure can be obtained by the concatenation formula. For example, the scattering

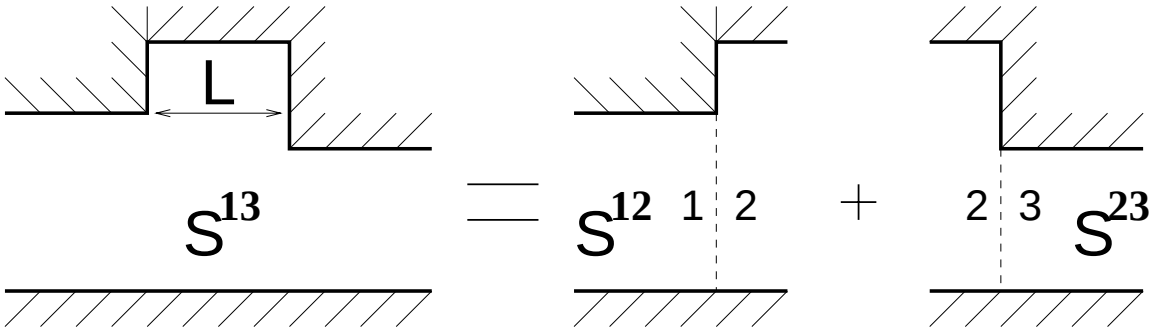

Figure A.1: Example of a two-step junction.

matrices $S^{\mathbf{12}}$ and $S^{\mathbf{23}}$ in a two-step junction, shown in Fig. A.1 are readily available from mode matching method. The combined S-matrix $S^{\mathbf{13}}$, by definition, should relate the amplitudes of ports 1 and 3. We proceed by writing down S-matrix relations connecting incoming and outgoing waves of adjacent ports

$$a^1_{out} = S^{\mathbf{12}}_{11} a^1_{in} + S^{\mathbf{12}}_{12} a^2_{in}, \tag{A.33}$$

$$a^2_{out} = S^{\mathbf{12}}_{21} a^1_{in} + S^{\mathbf{12}}_{22} a^2_{in}, \tag{A.34}$$

$$a'^2_{out} = S^{\mathbf{23}}_{22} a'^2_{in} + S^{\mathbf{23}}_{23} a^3_{in}, \tag{A.35}$$

$$a^3_{out} = S^{\mathbf{23}}_{32} a'^2_{in} + S^{\mathbf{23}}_{33} a^3_{in}, \tag{A.36}$$

and then eliminating the waves in region 2. Note that the $S's$ in these equations are matrices whose elements are S matrix elements. The boldface superscripts identify the individual S matrices as indicated in the figure, and the subscripts refer to the port on which they operate. Correspondingly, the a's are column vectors whose components are mode coefficients in the waveguide indicated by the superscript. The terms "in" and "out" refer to incoming and outgoing waves, respectively. All the amplitude a's are measured at the dashed line interfaces. As a result, the amplitude a^2's are related by

$$a'^2_{in} = e^{ik_2 L} a^2_{out} \quad \text{and} \tag{A.37}$$

$$a'^2_{out} = e^{-ik_2 L} a^2_{in}. \tag{A.38}$$

The region 2 amplitudes can be expressed in terms of those of regions 1 and 3 by combining the Eqs. A.34, A.35, A.37 and A.38. The result is then substituted in

Eqs. A.33 and A.36 to obtain

$$a^1_{out} = S^{\mathbf{12}}_{11} a^1_{in} - S^{\mathbf{12}}_{12}(S^{\mathbf{23}}_{22} e^{ik_2 L} S^{\mathbf{12}}_{22} - e^{-ik_2 L})^{-1}(S^{\mathbf{23}}_{22} e^{ik_2 L} S^{\mathbf{12}}_{21} a^1_{in} + S^{\mathbf{23}}_{23} a^3_{in}), \quad \text{(A.39)}$$

$$a^3_{out} = S^{\mathbf{23}}_{33} a^3_{in} - S^{\mathbf{23}}_{32}(S^{\mathbf{12}}_{22} e^{ik_2 L} S^{\mathbf{23}}_{22} - e^{-ik_2 L})^{-1}(S^{\mathbf{12}}_{21} a^1_{in} + S^{\mathbf{12}}_{22} e^{ik_2 L} S^{\mathbf{23}}_{23} a^3_{in}), \quad \text{(A.40)}$$

which gives the elements of the final S-matrix as follows:

$$S^{\mathbf{13}}_{11} = S^{\mathbf{12}}_{11} - S^{\mathbf{12}}_{12}(S^{\mathbf{23}}_{22} e^{ik_2 L} S^{\mathbf{12}}_{22} - e^{-ik_2 L})^{-1} S^{\mathbf{23}}_{22} e^{ik_2 L} S^{\mathbf{12}}_{21} \quad \text{(A.41)}$$

$$S^{\mathbf{13}}_{13} = -S^{\mathbf{12}}_{12}(S^{\mathbf{23}}_{22} e^{ik_2 L} S^{\mathbf{12}}_{22} - e^{-ik_2 L})^{-1} S^{\mathbf{23}}_{23} \quad \text{(A.42)}$$

$$S^{\mathbf{13}}_{31} = -S^{\mathbf{23}}_{32}(S^{\mathbf{12}}_{22} e^{ik_2 L} S^{\mathbf{23}}_{22} - e^{-ik_2 L})^{-1} S^{\mathbf{12}}_{21} \quad \text{(A.43)}$$

$$S^{\mathbf{13}}_{33} = S^{\mathbf{23}}_{33} - S^{\mathbf{23}}_{32}(S^{\mathbf{12}}_{22} e^{ik_2 L} S^{\mathbf{23}}_{22} - e^{-ik_2 L})^{-1} S^{\mathbf{12}}_{22} e^{ik_2 L} S^{\mathbf{23}}_{23} \quad \text{(A.44)}$$

Appendix B

Kroll-Yu Method

The Kroll-Yu method is based on the studies of the reflection coefficient $R(\omega)$ near the cavity resonance frequency to calculate the external Q of a waveguide loaded cavity.

Field in the waveguide region is easy to write down

$$E_z \propto e^{jkx} + Re^{-jkx}$$

where x is the longitudinal coordinate along the waveguide, with $x = 0$ taken at the cavity waveguide interface, and R is the reflection coefficient with respect to this surface. The propagation constant $k = \frac{1}{c}\sqrt{\omega^2 - \omega_c^2}$, and ω_c is the cutoff of the waveguide mode[1].

The Kroll-Yu method utilizes the observation that the eigenfrequency (complex) of the cavity-waveguide system without the shorting plane corresponds to a situation in which there is an outgoing wave but no incoming wave, plus the fact that reflection coefficient R has to have absolute value unity with real frequency ω. We can write

$$R(\omega) = -\frac{\omega - u + jv}{\omega - u - jv} e^{-2j\chi(\omega)} \tag{B.1}$$

where $\chi(\omega)$ is a real analytic function in the vicinity of the pole being studied. The minus sign is introduced for later convenience. The symbols u and v are the real and

[1] We have assumed that only one mode propagates in the waveguide at the frequency range under discussion

imaginary part of the resonant frequency, respectively. Since the field E_z must vanish at the shorting plane, thus $e^{jkD} + Re^{-jkD} = 0$

$$R(\omega) = -e^{2j\phi} = -e^{2jkD}. \tag{B.2}$$

Combine Eq. B.2 with Eq. B.1 to obtain

$$\phi(\omega) = \tan^{-1}\left(\frac{v}{\omega - u}\right) - \chi(\omega) + n\pi \tag{B.3}$$

where $\chi(\omega)$ is assumed to be adequately represented by its first two terms of a Taylor series expansion around u,

$$\chi(\omega) \approx \chi(u) + \chi'(u)(\omega - u). \tag{B.4}$$

Differentiating Eq. B.3 and applying Eq. B.4 we find

$$-\frac{1}{2}\frac{d\phi}{d\omega} = \frac{1}{2}\frac{u}{(\omega - u)^2 + v^2} + \frac{1}{2}\chi'(u). \tag{B.5}$$

It is apparent that Eq. B.5 exhibits a typical Breit-Wigner resonant form with peak at $\omega = u$, and when multiplied by v, with peak value $Q + \frac{1}{2}\chi'(u)v$, where $Q = \frac{v}{2u}$.

We note that the form of Eq. B.3 is unchanged when the origin of reference plane is shifted by a distance d, only $\chi(\omega) \rightarrow \chi(\omega) + kd$. Because the relationship between k and ω is not linear, shifting reference plane will result in different answers when we make the assumption in Eq. B.4. We can, of course, assume a different Taylor expansion

$$\chi(\omega) \approx \chi(k(u)) + \chi'(k(u))(k(\omega) - k(u)) \tag{B.6}$$

to make the choice of reference plane completely irrelevant.

We also note that the boundary condition of the shorting plane can be changed into magnetic, which amounts to changing $n\pi$ in Eq. B.3 to $(n + 1/2)\pi$, or equivalently changing $\chi(u)$ into $\chi(u) + 1/2\pi$. The same argument applies to any boundary conditions.

The choice of representation of $R(\omega)$ by Eq. B.1 is not unique. Sometimes, it is useful to exhibit two or more resonances. Taking into account of the fact that

each resonance corresponds to a pole in the expression of $R(\omega)$, we may write

$$R(\omega) = -e^{2j\phi} = -\frac{\omega - u_1 + jv_1}{\omega - u_1 - jv_1}\,\frac{\omega - u_2 + jv_2}{\omega - u_2 - jv_2}e^{-2j\chi(\omega)}, \tag{B.7}$$

which gives

$$\phi(\omega) = \tan^{-1}\left(\frac{v_1}{\omega - u_1}\right) + \tan^{-1}\left(\frac{v_2}{\omega - u_2}\right) - \chi(\omega) + n\pi. \tag{B.8}$$

The same reference plane independent approximation of $\chi(\omega)$ can be made.

B.1 Implementation Formula

Equation B.3 with the approximation Eq. B.4 or Eq. B.6 provides a four parameters representation of the function $\phi(\omega)$, which can be numerically solved [16] with four ϕ-ω pairs as the input. A set of MAFIA calculations with different value of D are performed[2]. With the inspection of field plot, if one branch near the resonance (avoided crossing) can be identified, four MAFIA runs with different length will provide enough information. With two branches near AC identified, two MAFIA runs are needed.

The procedure can be thought as a four parameters fit to the four data points. Thus explicit formula expressing u, v, $\chi(u)$, and $\chi'(u)$ in terms of the four data points ϕ_i and ω_i ($i \in \{1, 2, 3, 4\}$) is of interest.

We did not quite achieve that due to the complicated nature of the expressions, but we will show that for arbitrary choice of $\chi'(u)$, it is possible to obtain explicit expression for u, v, and $\chi(u)$ by requiring them to satisfy the $\phi(\omega)$ curve for any three data points. The fourth data point provides a straight forward root search to find $\chi'(u)$, therefore, determining all the parameters.

Let us designate the three points by (ϕ_i, ω_i) where $i \in \{1, 2, 3\}$. Then from Eq. B.3 with the approximation Eq. B.4[3].

$$\phi_i + \chi(u) + \chi'(u)(\omega_i - u) = \tan^{-1}(\frac{v}{\omega_i - u}) \tag{B.9}$$

[2] Waveguide boundary conditions can be arbitrary as long as they are consistent

[3] Eq. B.3 and Eq. B.6 produce similar results

Taking the difference of the above for $i = 1$ and $i = 2$ yields

$$\phi_1 - \phi_2 + \chi'(u)(\omega_1 - \omega_2) = \tan^{-1}(\frac{v}{\omega_1 - u}) - \tan^{-1}(\frac{v}{\omega_2 - u}) \tag{B.10}$$

Next we take tangent of both sides, use a standard trigonometric identity, and rearrange slightly to get

$$\tan(\phi_1 - \phi_2 + \chi'(u)(\omega_1 - \omega_2)) = \frac{v(\omega_2 - \omega_1)}{(\omega_1 - u)(\omega_2 - u) + v^2} \tag{B.11}$$

Now we take the reciprocal and multiply by $(\omega_1 - \omega_2)$ to obtain

$$(\omega_1 - \omega_2)\cot(\phi_1 - \phi_2 + \chi'(u)(\omega_1 - \omega_2)) = -v - \frac{(\omega_1 - u)(\omega_2 - u)}{v} \equiv B_{12} \tag{B.12}$$

Here we identify B_{12} with the left-hand side of Eq. B.12 and note that it is completely determined by a pair of the originally designated points and the assumed value of $\chi'(u)$. Defining B_{23} similarly, we define

$$A \equiv \frac{B_{12} - B_{23}}{\omega_3 - \omega_1}, \tag{B.13}$$

a quantity determined by the three designed points and $\chi'(u)$. Then we find, following simple algebra, that

$$\frac{\omega - u}{v} = A. \tag{B.14}$$

Eq. B.14 can be combined with Eq. B.12 to eliminate v and obtain

$$u = \frac{\omega_2 + AB_{12} + \omega_1 A^2}{1 + A^2}. \tag{B.15}$$

Now that u has been determined, v and $\chi(u)$ can be determined accordingly from Eq. B.12 and B.14.

$$v = (u - \omega_1)A - B_{12} \tag{B.16}$$

$$\chi(u) = \tan^{-1}(\tfrac{v}{\omega_i - u}) - \phi_i - \chi'(u)(\omega_i - u) \tag{B.17}$$

The second expression can be evaluated at any of the 3 points. Indeed, despite the asymmetric appearance of the 3 data points in Eqs. B.15, B.16 and B.17, the results are independent of the order. In fact, by using 3 data points and assuming $\chi'(u) = 0$,

we have an explicit three-parameter formula, which is very accurate at sufficiently high Q_{ext} provided that the input data is accurate. More reliable result, however, can be obtained by determining $\chi'(u)$ from a fourth data point. Rearranging Eq. B.9 for $i = 4$

$$\omega_4 - u - v\cot(\phi_4 + \chi(u) + \chi'(u)(\omega_4 - u)) = 0 \tag{B.18}$$

Since all 3 parameters have been expressed in terms of $\chi'(u)$, the left hand side of Eq. B.18 can be regarded as a function of $\chi'(u)$. $\chi'(u)$ is determined as a root of it. It is possible that Eq. B.18 has more than one root due to the periodic nature of the cot. A FORTRAN program is used to manually select the right one.

Appendix C

A Few Examples of BBU Growth Rate

C.1 $h(m) = \delta_{m,1}$ (Daisy Chain Model)

From Eq. 7.32 we immediately have

$$\cos\theta = 0, \tag{C.1}$$

which gives

$$\theta = \frac{\pi}{2}. \tag{C.2}$$

And from Eqs. 7.33 and 7.34, we obtain

$$\gamma = \frac{\lambda u}{2} \quad and \quad N_{max} = \frac{\lambda u}{2} \tag{C.3}$$

C.2 $h(m) = e^{-\beta(m-1)}$

We first calculate an auxiliary function $f(e^{i\theta})$,

$$f(e^{i\theta}) = \sum_{m=1}^{\infty} h(m) e^{im\theta} = e^{\beta} \sum_{m=1}^{\infty} e^{-m\beta} e^{im\theta}. \tag{C.4}$$

Summing the series we obtain the closed form

$$f(e^{i\theta}) = e^{\beta} \frac{e^{-\beta} e^{i\theta}}{1 - e^{-\beta} e^{i\theta}} = \frac{e^{i\theta} - e^{-\beta}}{1 + e^{-2\beta} - 2e^{-\beta}\cos\theta}. \tag{C.5}$$

If we write Eq. 7.32 in the following form

$$0 = \frac{d}{d\theta}\Im(f(e^{i\theta})) = \frac{d}{d\theta}\frac{\sin\theta}{1+e^{-2\beta}-2e^{-\beta}\cos\theta} = \frac{(1+e^{-2\beta})\cos\theta - 2e^{-\beta}}{(1+e^{-2\beta}-2e^{-\beta}\cos\theta)^2}, \tag{C.6}$$

the solution is easily obtained:

$$\cos\theta = \frac{1}{\cosh\beta}. \tag{C.7}$$

Substituting Eq. C.7 in Eqs. 7.33 and 7.34, we obtain

$$\gamma = \frac{\lambda u}{2}\Im(f(e^{i\theta})) = \frac{1}{1-e^{-2\beta}}\frac{\lambda u}{2} \quad and \tag{C.8}$$

$$N_{max} = \frac{\lambda u}{2}[-\Re(\frac{d}{d\theta}f(e^{i\theta}))] = \frac{\coth\beta}{1-e^{-2\beta}}\frac{\lambda u}{2}. \tag{C.9}$$

C.3 $h(m) = m^{-1-\epsilon}$

With a power law decaying wakefield, stationary point equation 7.32 becomes

$$0 = \Re(\sum_{m=1}^{\infty}\frac{(e^{i\theta})^m}{m^{\epsilon}}) = \Re(e^{i\theta}\Phi(e^{i\theta},\epsilon,1)), \tag{C.10}$$

where $\Phi(z,s,v)$ is Lerch Φ function defined by

$$\Phi(z,s,v) = \sum_{m=0}^{\infty}\frac{z^m}{(v+m)^s}. \tag{C.11}$$

Taking $\epsilon = \frac{1}{2}$ for example, we use Mathematica [44] to solve Eq. C.10 numerically to obtain

$$\theta \approx 0.74377. \tag{C.12}$$

Substituting in Eqs. 7.33 and 7.34,

$$\gamma = \Im(e^{i\theta}\Phi(e^{i\theta},1+\epsilon,1))\frac{\lambda u}{2} \approx 1.07736\frac{\lambda u}{2} \tag{C.13}$$

$$N_{max} = \Im(e^{i\theta}\Phi(e^{i\theta},\epsilon,1))\frac{\lambda u}{2} \approx 1.29804\frac{\lambda u}{2} \tag{C.14}$$

follows.

We observe numerically that at the limit of $\epsilon \to 0^+$, the stationary point $e^{i\theta}$ from Eq. 7.32 approaches 1. Near $z = 1$, Lerch Φ function has an asymptotic expression [45]

$$\lim_{z\to 1} \Phi(z, s, v) = , (1-s)(1-z)^{s-1}, \tag{C.15}$$

where , is Gamma function. In the limit of $e^{i\theta} \to 1$, we obtain

$$e^{i\theta}\Phi(e^{i\theta}, \epsilon, 1) = e^{i\theta}(1-e^{i\theta})^{s-1}, (1-\epsilon) = e^{i\theta} \mid 1-e^{i\theta} \mid^{\epsilon-1} e^{i\phi(\epsilon-1)}, \tag{C.16}$$

where $\tan\phi = \frac{-\sin\theta}{1-\cos\theta} = -\cot\frac{\theta}{2}$, i.e. $\phi = -(\frac{\pi}{2} - \frac{\theta}{2})$. To simplify the expression, , $(1-\epsilon)$ is taken to be 1. Therefore Eq. C.16 can be written as

$$\begin{aligned} e^{i\theta}\Phi(e^{i\theta}, \epsilon, 1) &= e^{i\theta}(2\sin\frac{\theta}{2})^{\epsilon-1} e^{i(\frac{\pi}{2}-\frac{\theta}{2})(1-\epsilon)} \\ &= ie^{i(\frac{\theta}{2}(1+\epsilon)-\frac{\pi}{2}\epsilon)}(2\sin\frac{\theta}{2})^{\epsilon-1}. \end{aligned} \tag{C.17}$$

The result

$$\theta = \pi\frac{\epsilon}{1+\epsilon} \to \pi\epsilon. \tag{C.18}$$

is easily obtained by noting Eqs. C.10 and C.17.

The value of N_{max} then follows from Eq. 7.34, C.17, and C.18

$$N_{max} = \frac{\lambda u}{2}\sum_{m=1}^{\infty} m h(m)\sin(m\theta) = \Im(e^{i\theta}\Phi(e^{i\theta}, \epsilon, 1))\frac{\lambda u}{2} \to \frac{1}{\theta}\frac{\lambda u}{2} = \frac{1}{\pi}\frac{1}{\epsilon}\frac{\lambda u}{2}. \tag{C.19}$$

From a generic expansion of Lerch Φ function [46], we have

$$\Phi(z, s, v) = \frac{, (1-s)}{z^v}(\log\frac{1}{z})^{s-1} + z^{-v}\sum_{r=0}^{\infty}\zeta(s-r, v)\frac{(\log z)^r}{r!}, \tag{C.20}$$

where $\zeta(s, v)$ is the generalized zeta function defined by

$$\zeta(s, v) = \sum_{n=0}^{\infty}(v+n)^{-s} \qquad\qquad v \neq 0, -1, -2, \ldots \ \Re(s) > 1. \tag{C.21}$$

If s is taken to be $1+\epsilon$, we have

$$e^{i\theta}\Phi(e^{i\theta}, 1+\epsilon, 1) = , (-\epsilon)(-i\theta)^{\epsilon} + \sum_{r=0}^{\infty}\zeta(1+\epsilon-r, 1)\frac{(i\theta)^r}{r!}. \tag{C.22}$$

With $\epsilon \to 0^+$, we have [47]

$$, (-\epsilon) = \frac{-1}{\epsilon} + \psi(1) - \frac{\epsilon}{2}(\frac{\pi^2}{3} + \psi^2(1) - \psi'(1)) + O(\epsilon^2), \tag{C.23}$$

where $\psi(1) = -\gamma_e$ and $\psi'(1) = \zeta(2,1) = \frac{\pi^2}{6}$. We also have [48]

$$\zeta(1+\epsilon,1) = \zeta(1+\epsilon) = \frac{1}{\epsilon} + \sum_{n=0}^{\infty} \frac{(-1)^n}{n!}\gamma_n \epsilon^n = \frac{1}{\epsilon} + \gamma_0 - \gamma_1\epsilon + O(\epsilon^2), \tag{C.24}$$

where γ_n are constants defined by

$$\gamma_n = \lim_{m\to\infty}\{\sum_{k=1}^{m} \frac{(\log k)^n}{k} - \frac{(\log m)^{n+1}}{n+1}\}. \tag{C.25}$$

As a special case, we see that $\gamma_0 = \gamma_e$. We also have [49][1]

$$\zeta(\epsilon,1) = \zeta(\epsilon) = -\frac{1}{2} + O(\epsilon). \tag{C.26}$$

Putting Eqs. C.23, C.24, and C.26 together, Eq. C.22 becomes

$$\begin{aligned} & e^{i\theta}\Phi(e^{i\theta},1+\epsilon,1) \\ = \; & [-\frac{1}{\epsilon} - \gamma_e - \frac{\epsilon}{2}(\frac{\pi^2}{3} + \gamma_e^2 - \frac{\pi^2}{6})][1 + \epsilon\log(-i\theta) + \frac{\epsilon^2}{2}\log^2(-i\theta)] \\ + \; & (\frac{1}{\epsilon} + \gamma_e - \gamma_1\epsilon) - \frac{1}{2}i\theta + O(\epsilon^2\log\epsilon). \end{aligned} \tag{C.27}$$

In keeping the lowest order of ϵ, we have used the fact that θ is of the same order as ϵ. Eq. C.27 is further simplified into

$$\begin{aligned} & e^{i\theta}\Phi(e^{i\theta},1+\epsilon,1) \\ = \; & (i\frac{\pi}{2} - \log\theta)(1+\epsilon\gamma_e) - \frac{\epsilon}{2}(\log\theta - i\frac{\pi}{2})^2 - \frac{i\theta}{2} - \frac{\epsilon}{2}(\frac{\pi^2}{6} + \gamma_e^2) - \gamma_1\epsilon. \end{aligned} \tag{C.28}$$

From Eq. 7.34, C.28 and C.18, the value of maximum growth rate γ is obtained.

$$\begin{aligned} \gamma &= \Im(e^{i\theta}\Phi(e^{i\theta},1+\epsilon,1))\frac{\lambda u}{2} \\ &= [\frac{\pi}{2}(1+\epsilon\gamma_e) + \frac{\pi}{2}\epsilon\log\theta - \frac{1}{2}\theta]\frac{\lambda u}{2} \qquad \text{(C.29)} \\ &= \frac{\pi}{2}[1 + \epsilon\log\epsilon + (\log\pi + \gamma_e - 1)\epsilon]\frac{\lambda u}{2}. \qquad \text{(C.30)} \end{aligned}$$

[1]The definition of $\zeta(s,v)$ in Eq. C.21 does not apply here, but its analytical continuation defined by other series applies, for example, Eq. C.24.

Bibliography

[1] D. W. Kerst et al., Phys. Rev. **102**, 590 (1956).

[2] R. Palmer, *High Energy Physics in the 1990's*, S. Jenson, Ed. (World Scientific, Singapore, 1989), pp.638-641.

[3] L. Fonda, G. C. Ghirardi, and A. Rimini, *Rep. Prog. phys.,* **41**, 587 (1978).

[4] Alexander W. Chao *Physics of Collective Beam Instabilities in High Energy Accelerators*, Wiley-Interscience Publication. 1993.

[5] Norbert Holtkamp, talk at SLAC, Jan 10, 1995.

[6] Tsumoru Shintake, private communication.

[7] J. D. Jackson, *Classical Electrodynamics*, 2nd ed., Wilsey, New York, 1975.

[8] *PEP-II An Asymmetric B Factory*, CDR, SLAC-418 June. 1993, 34.

[9] T. Weiland et al. *DESY Report*, M-86-07, June 1986.

[10] K. Halbach and R. F. Holsinger, *Particle Accelerators* **7**, 213 (1976).

[11] J. N. Corlett, *Proc. of the IEEE Part. Acce. Conf. 1989*, 211.

[12] A. F. Jacob, G. R. Lambertson, and W. Barry *Proc. of the 2nd European Part. Acce. Conf. 1990*, 928.

[13] J. C. Slater, *Microwave Electronics* (Van Nostrand, New York, 1950).

[14] R. L. Gluckstern and R. Li, *Proceedings of the 1988 LINAC Conference*, CEBAF report 89-001,(1989) pp.356-358. Also T. Kageyama, KEK-report 89-4(1989).

[15] Y. Goren and David U. L. Yu, SLAC/AP-73(1989).

[16] N. M. Kroll and D. U. L. Yu, *Particle Accelerators* **34**, 231 (1990).

[17] N. Kroll, J. Kim, and D. Yu *Proc. 1992 Linac Conf.* Ottawa, Ontario, August 24-28 (1992) AECL-10728, 217 (1992).

[18] Norman M. Kroll and Xintian E. Lin, *Proc. of 1990 LINAC Conference*, Albuquerque, NM, Sept. 10-14 (1990), 238.

[19] P. Arcioni and G. Conciauro, *Particle Accelerators* **36**,177 (1991).

[20] K. A. Thompson, et al. *Particle Accelerators*, Nov 1993, (SLAC-PUB-6032).

[21] N. M. Kroll, K. A. Thompson, et al. *Proc. of the 6th Workshop on Advanced Accelerator concepts*, Lake Geneva, WI, June 12-18, 1994

[22] N. M. Kroll, K. A. Thompson, et al. *Proc. of the IEEE Part. Acce. Conf.* 1995.

[23] K. A. Thompson and R. D. Ruth, *Phys. Rev. D* **41**, 964, (1990).

[24] R. Mittra, S. W. Lee *Analytical Techniques in the Theory of Guided wave.*

[25] N. Marcuvitz, *Waveguide Handbook.* McGraw-Hill, 1951. 318.

[26] see [25]. 312.

[27] C. G. Montgomery, R. H. Dicke, E. M. Purcell, *Principles of Microwave Circuits.* McGraw-Hill, 1948.

[28] see [27]. page 47, Eq.(76).

[29] R. E. Collin, *Field Theory of Guided Waves.* IEEE Press, 1991, pp 190-192.

[30] W. K. H. Panofsky and W. A. Wenzel, Rev. Sci. Instr. **27**, 967, (1956).

[31] R. B. Neal and W. H. Panofsky, Science **152**, 1353 (1966).

[32] P. B. Wilson, Report No. HEPL-TN-67-8(unpublished).

[33] W. K. H. Panofsky and M. Bander, Rev. Sci. Instr. **39**, 206, (1968).

[34] R. H. Helm and G. A. Loew, *Linear Accelerators* (North-Holland, Amsterdam, 1970).

[35] V. K. Neil, L. S. Hall and R. K. Cooper, *Particle Accelerators* **9**, 213 (1979).

[36] A. W. Chao, B. Richter, and C. Y. Yao, Nucl. Instrum. Methods **178**, 1 (1980).

[37] R. L. Gluckstern, R. K. Cooper, and P. J. Channel *Particle Accelerators* **16**, 125 (1985).

[38] R. L. Gluckstern, F. Neri, and R. K. Cooper, *Particle Accelerators* **23**, 37 (1988).

[39] R. L. Gluckstern, F. Neri, and R. K. Cooper, *Particle Accelerators* **23**, 53 (1988).

[40] K. Yokoya, Report No. DESY 86-084 (unpublished).

[41] G. Decker and J. M. Wang, Phys. Rev. D **38**, 980 (1980).

[42] L. Graham, Donald E. Knuth, and Oren Patashnik, *Concrete Mathematics.* Addison-Wesley. 1994. Sect. 7.3.

[43] Marshall Rosenbluth, private communication.

[44] Stephen Wolfram, *Mathematica, a system for doing mathematics by computer.* Addison-Wesley, 1991.

[45] *Higher Transcendental Functions.* McGraw-Hill, 1955. 30, equation (12).

[46] see [45] 29, equation (8).

[47] see [45] 46, equation (11).

[48] M. Abramowitz and I. Stegun, *Handbook of Mathematical Functions*, Dover, 1972. 807, equation 23.2.5.

[49] see [48], 807, equation 23.2.11 and 23.2.13.